Synthesis of monolithic graphene oxide-based adsorbents for CO_2 capture

A thesis submitted for the award of degree of

Doctor of Philosophy

Submitted by

RANJEET KUMAR JHA

(Registration No.: 901909021)

Under the guidance of

Dr. Soumen Basu
Professor
Department of Chemistry and Biochemistry

Dr. Haripada Bhunia
Professor
Department of Chemical Engineering

THAPAR INSTITUTE
OF ENGINEERING & TECHNOLOGY
(Deemed to be University)

Department of Chemistry and Biochemistry
Thapar Institute of Engineering and Technology (Deemed to be University)
Patiala-147004, Punjab (India)
www.thapar.edu

March 2024

Dedicated

To

My Parents

Father: Krishna Nand Jha & Father's in law: Prem Nath Jha
Mother: Asha Jha & Mother's in law: Sudha jha

My siblings, including my brothers and sister

Anil Kumar Jha, Sudhir Kumar Jha, Ajit Kumar Jha, Prassana Kumar Jha and Shyama Jha

And

My wife and son

Alka Kumari and Arjit Kumar Jha

CERTIFICATE

This certificate attests to the authenticity of the thesis titled ***"Synthesis of monolithic graphene oxide-based adsorbents for CO_2 capture"*** *being submitted by Mr. Ranjeet Kumar Jha to Department of Chemistry and Biochemistry, Thapar Institute of Engineering & Technology (Deemed to be University), Patiala for the award of degree of* ***Doctor of Philosophy****. This document presents a comprehensive record of the genuine research conducted by the individual under our guidance and supervision. It successfully fulfills the prescribed conditions for submitting this thesis, and to the best of our knowledge, it has met the requisite standards.*

The findings presented in this thesis, whether in their entirety or partially, have not been shared with any other university or institute for the purpose of conferring a degree or diploma.

S Basu

(Supervisor)
Dr. Soumen Basu
Professor
Department of Chemistry and Biochemistry,
Thapar Institute of Engineering &
Technology, Patiala, Punjab (India)

(Supervisor)
Dr. Haripada Bhunia
Professor
Department of Chemical Engineering,
Thapar Institute of Engineering &
Technology, Patiala, Punjab (India)

(Head)
Dr. Manmohan Chhibber
Professor & Head
Department of Chemistry and Biochemistry,
Thapar Institute of Engineering & Technology,
Patiala, Punjab (India)

CANDIDATE'S DECLARATION

I, hereby declare that the work presented in the thesis entitled ***"Synthesis of monolithic graphene oxide-based adsorbents for*** CO_2 ***capture",*** *in fulfilment of the requirement for the* ***award of the Degree of Doctor of Philosophy*** *in the Department of Chemistry and Biochemistry, Thapar Institute of Engineering and Technology, Patiala, is an authentic record of my own work carried out under the supervision of Dr. Soumen Basu (Professor, Department of Chemistry and Biochemistry, TIET) and Dr. Haripada Bhunia (Professor, Department of Chemical Engineering, TIET). The matter presented in this thesis has not been submitted in part or full for the award of any degree in India or Abroad.*

Ranjeet Kr. Jha

Ranjeet Kumar Jha

ACKNOWLEDGEMENTS

I express heartfelt gratitude to the divine for providing me with the strength to successfully complete this project.

The execution of this work took place in the Advanced Nanomaterials Laboratory and Chemical Engineering Lab at Thapar Institute of Engineering and Technology from 2019 to 2024. I extend my deepest gratitude, particularly to my supervisors, for their invaluable guidance and support ***Prof. Soumen Basu,*** *Department of Chemistry and Biochemistry, Thapar Institute of Engineering & Technology (Deemed to be University) and* ***Prof. Haripada Bhunia****, Department of Chemical Engineering, Thapar Institute of Engineering & Technology (Deemed to be University). I am immensely grateful to my supervisors for granting me this exceptional study opportunity and for their ceaseless advice, wisdom, and inspiration throughout the course of my research. Their guidance has been instrumental in enriching my knowledge during my Ph.D. studies. I endeavored to emulate their consistent habit of staying abreast of contemporary scientific research, a practice from which I derived significant insights. I am profoundly grateful for their unwavering support and encouragement to conduct top-notch research. It has been a tremendous honor to work under their guidance.*

I express profound gratitude to ***Prof. Padmakumar Nair****, Director, Thapar Institute of Engineering & Technology (Deemed to be University),* ***Prof. N. Tejo Prakash****, Dean of Research & Development Cell, Thapar Institute of Engineering & Technology (Deemed to be University) and* ***Prof. Manmohan Chhibber****, Head, Department of Chemistry and Biochemistry, Thapar Institute of Engineering & Technology (Deemed to be University) for providing the opportunity to pursue this doctoral research.*

I extend profound gratitude to the members of my doctoral committee ***Dr. Neetu Singh*** *of Department of Chemical Engineering,* ***Prof. Amjad Ali*** *and* ***Dr. Banibrata Maity****, Department of Chemistry & Biochemistry, Thapar Institute of Engineering & Technology (Deemed to be University) for their massive assistance in guiding me in the right direction.*

My heartfelt thanks to the staff members of the Department of Chemistry & Biochemistry and Department of Chemical Engineering, Thapar Institute of Engineering & Technology

(Deemed to be University) due to their invaluable assistance, moral support, and spiritual guidance.

I extend my heartfelt gratitude to my friends and lab mates, Mrs. Ayushi, Mrs. Anuska Garg, Smt. Niru Sohal, Mr. Pritam Hait, Mr. Himanshu Rahav, and Dr. Saudagar Dongare, for the wonderful times and unwavering moral support. The warmth they exuded, embodied by their ever-smiling faces, will be a cherished inspiration for me.

I gratefully acknowledge the financial support provided by ***Thapar Institute of Engineering & Technology (Deemed to be University)*** *throughout the course of this work.*

Furthermore, I wish to express my gratitude to all those who knowingly or unknowingly assisted me in successfully completing this task.

ABSTRACT

Carbon dioxide (CO_2) is a major greenhouse gas, poses one of the greatest challenges of the twenty-first century. The imperative to reduce CO_2 concentration globally stems from the far-reaching impacts of global warming and climate change concerns. Among carbon capture and storage (CCS) technologies, oxy-fuel combustion, post-combustion, and pre-combustion are prominent. Notably, post-combustion is acknowledged as an environmentally sustainable and cost-effective solution. Since graphene has an expansive surface area, minimal energy requirement for regeneration, and impressive attributes such as high adsorption capacity, selectivity, and rapid kinetics, graphene stands out as a highly sought-after adsorbent for CO_2 capture. Despite the superior performance of CO_2 adsorption under static conditions, this method is impractical for flue gas applications. Our research endeavors to bridge this gap by employing a self-assembled methodology, subsequently activated under suitable conditions using carbon sources containing oxygen. This approach aims to improve the resulting adsorbents' texture, surface characteristics, and CO_2/N_2 selectivity. Three types of monolithic graphene oxide-based adsorbents were established by the self-assembly reduction process of graphene oxide and activated physically/chemically, as shown in Scheme 1.

A high surface area of physically activated oxygen-enriched monolithic graphene oxide was developed by a self-assembly reduction process of graphene oxide at 90 °C. The as-synthesized monoliths were physically activated (UV treatment) within different periods (2.5, 5, 10, and 15 h) and observed the CO_2 adsorption effect in various conditions (temperature and concentration of CO_2 flow). The synthesized monolithic properties explored the CO_2 adsorption effect under dynamic conditions and revealed the CO_2 capture performance. The variation in morphology, specific surface area, crystal defects, functionality detection, and CO_2 capture performance were analyzed by SEM, BET, XRD/Raman, FTIR, and TGA, respectively. The optimized adsorbent reveals an excellent dynamic CO_2 capture

capacity of 1.65 mmol g^{-1} at 25 °C, owing to its elevated BET surface area of 577.3 m^2 g^{-1}. Considering the desorption step with a constant volume flow rate, it becomes evident that the pressure drop results in excessive consumption of desorbing gas (N_2), approximately 50 % of the regeneration process. Several studies were investigated; the regenerability of 98.8 %, an excellent CO_2/N_2 selectivity, fast kinetics, the pseudo-second-order kinetic model and Freundlich isotherm model were best fitted. Thermodynamic studies reveal the heterogeneity of the adsorption site and the adsorption process endothermic nature, as indicated by $\Delta H°$ value of +13.1154139 KJ mol^{-1}, underscoring the distinctive characteristic property of chemisorption.

High surface area chemically activated carbon-enriched monolithic reduced Graphene Oxide was synthesized by self-assembly reduction process of graphene oxide at 90 °C with different weight ratios of oxalic acid (1:1, 1:0.500, and 1:0.250). The as-synthesized monoliths were carbonized (at 600 °C) and chemically activated with varying proportions of NaOH (1:1, 1:2, and 1:3). These materials offer the CO_2 adsorption effect under dynamic conditions, fast mass transfer, easy handling, and outstanding stability throughout the adsorption-desorption cycle. FE-SEM and HR-TEM analyses confirmed the porous nature and shape of the adsorbents. At the same time, XPS examination revealed the presence of distinct functional groups on the surface of the monolith. By increasing the mass ratios (MGO:NaOH) from 1:1 to 1:2, the surface areas increased by approximately 2.6 times, ranging from 520.8 to 753.9 m^2 g^{-1} (surface area of the untreated MGO was 289.2 m^2 g^{-1}). Consequently, this resulted in a notable enhancement of 2.10 mmol g^{-1} in dynamic CO_2 capture capacity. The assessment encompassed the evaluation of production yield, selectivity, regenerability, kinetics, equilibrium isotherm, and isosteric temperatures of adsorption (Q_{st}). The decrease in CO_2 capture effectiveness with rising adsorption temperature indicated an exothermic and physisorption process. The regenerability of 99.1 % at 100 °C and excellent cyclic stability with efficient CO_2 adsorption make this monolithic adsorbent appropriate for post-combustion CO_2 capture. The significant Q_{st} supports the heterogeneity of the adsorbent's surface, and the pseudo-second-order kinetic model,andh the Freundlich isotherm model emerged as the most fitting. Therefore, the current investigation shows that the carbon-enriched adsorbents enhance the CO_2 adsorption capacity. It may be used as a low-cost pretreatment method on an industrial scale before carbon capture.

Innovating Monolithic Graphene Oxide Frameworks were prepared through the utilization of innovative porous crystalline structures established via KOH-treated monolithic graphene oxide frameworks. These materials exhibit remarkable and versatile characteristics for both functional exploration and applications within the realm of CO_2 capture. In this comprehensive study, we have synthesized monolithic reduced graphene oxide-based adsorbents through a meticulous self-assembly process involving different mass ratios of GO/malic acid (MaA) (1:0.250, 1:0.500, and 1:1 by weight). Building upon this foundation, we further modified MGO 0.250 through KOH treatment by chloroacetic acid method, leading to the creation of MGO 0.250_KOH, which was subjected to CO_2 capture assessments. The comprehensive investigation encompassed an array of parameters, including morphology, specific surface area, crystal defects, functional group identification, and CO_2 capture efficiency. Employing a combination of FT-IR, XRD, Raman, BET, SEM, HR-TEM, and XPS techniques, the study revealed profound insights. Particularly notable was the observation that the MGO 0.250_KOH adsorbent exhibited an exceptional CO_2 capture performance, leading to a significant enhancement of the CO_2 capture capacity from 1.69 mmol g^{-1} to 2.35 mmol g^{-1} at standard conditions of 25 °C and 1 bar pressure. This performance enhancement was concomitant with an augmentation in surface area, elevating from 287.93 to 419.75 m^2 g^{-1} (a nearly 1.5-fold increase compared to MGO 1.000 with a surface area of 287.93 m^2 g^{-1}). The monolithic adsorbent demonstrated a commendable production yield of 82.92%, along with an impressive regenerability of 98.80% at 100 °C. Additionally, adsorbent's proficiency in CO_2 adsorption renders it a promising candidate for post-combustion CO_2 capture applications. These findings collectively underscore the capacity of adsorbents to significantly amplify CO_2 capture capabilities. The viability of employing this strategy as an uncomplicated pre-treatment technique in various industrial sectors is a plausible prospect, given the study's outcomes.

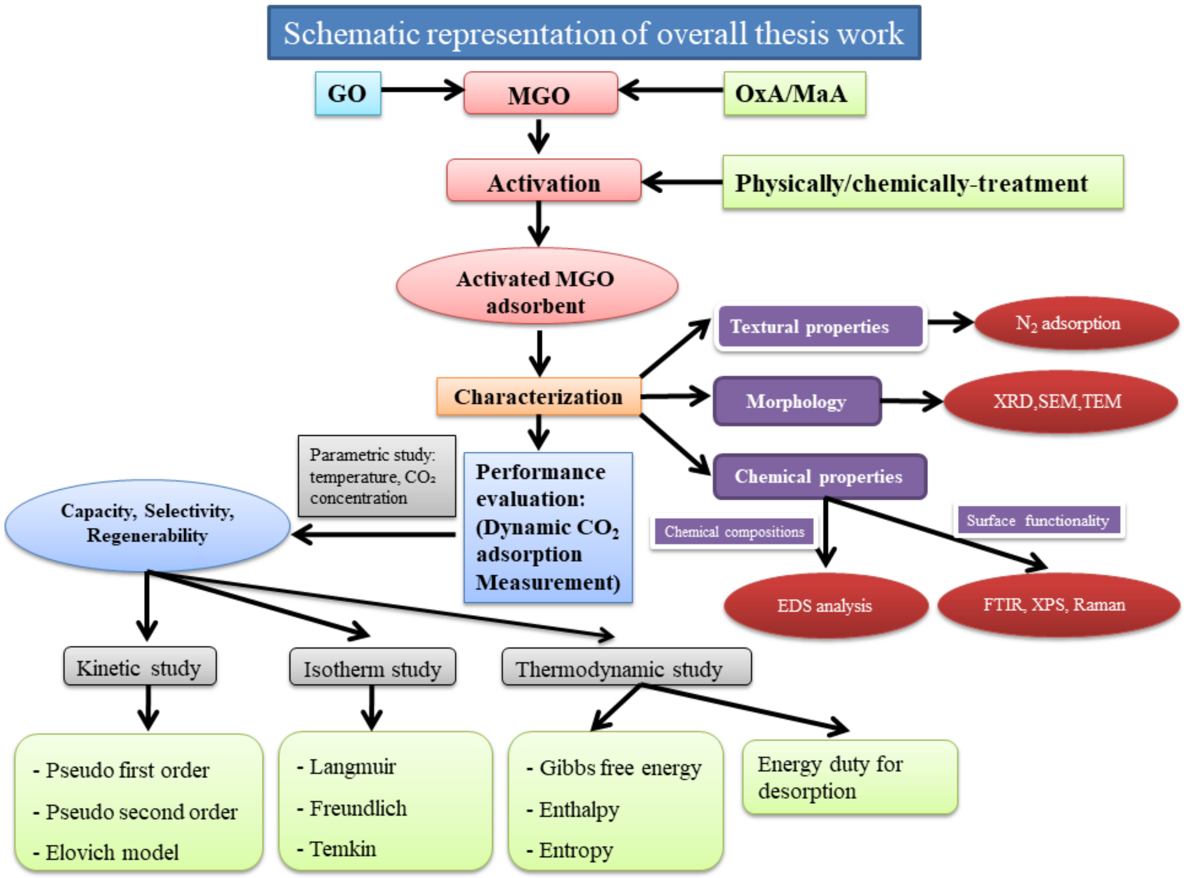

Scheme 1 Schematic representation of the overall thesis work.

TABLE OF CONTENTS

LIST OF FIGURES

LIST OF TABLES

LIST OF SYMBOLS

Atm	Standard atmosphere
B	Heat of adsorption, J mol^{-1}
B	Temkin constant related to the heat of adsorption, J mol^{-1}
C	Effluent CO_2 concentration, volume %
C_o	CO_2 inlet concentrations, volume %
C_p	Specific heat capacity of the adsorbent, J g^{-1} K^{-1}
k_1	Pseudo-first order rate constant, min^{-1}
k_2	Pseudo-second order rate constant, g mmol^{-1} min^{-1}
k_α	Elovich order rate constant.
K_L	Langmuir adsorption isotherm constant, atm^{-1}
K_F	Freundlich adsorption isotherm constant, mmol g^{-1} atm$^{-1/n}$
K_T	Temkin adsorption isotherm constant, atm^{-1}
M	Mass of the adsorbent, g
N	Fractional order model constant related to driving force
N	Total number of experimental points
P	CO_2 partial pressure in atm
$q_{t\ (exp)}$	Experimental CO_2 adsorption capacity, mmol g^{-1}
$q_{t\ (pred)}$	Predicted CO_2 adsorption capacity, mmol g^{-1}
q_e	Dynamic adsorption capacity at equilibrium, mmol g^{-1}
q_m	Maximum monolayer adsorption capacity, mmol g^{-1}
q_t	CO_2 adsorption capacity at time t, mmol g^{-1}
Q_{st}	Isosteric heat of adsorption, kJ mol^{-1}
R	Universal gas constant, kJ mol^{-1} K^{-1}
R^2	Regression coefficient

S_{BET}	BET surface area, $m^2\ g^{-1}$
T	Time, min
T	Temperature, K
V_{meso}	Mesopore volume, $cm^3\ g^{-1}$
V_{micro}	Micropore volume, $cm^3\ g^{-1}$
V_P	Total pore volume obtained at a relative pressure of 0.99, $cm^3\ g^{-1}$

Greek Letters

Å	Angstrom
Θ	Theta
Λ	Wavelength

LIST OF ABBREVIATIONS

A%	Relative area percentage
B. E.	Binding energy
BET	Brunauer–Emmett–Teller
BJH	Barrett–Joyner–Halenda
SSA	Surface area and pore size distribution
MGO	Monolithic graphene oxide
GHGs	Greenhouse gases
PFCs	Perfluorocarbons
HFCs	Hydrofluorocarbons
EPA	Environmental Protection Agency
PEI	Polyethyleneimine
EDA	Ethylenediamine
NETL	National energy technology laboratory (U.S.)
DOE	Department of energy
MWCNTs	Multi-walled carbon nanotubes
Ppm	Parts per million
FT-IR	Fourier transformed infra-red
PSDs	Pore size distributions
SEM	Scanning electron microscopy
EDS	Energy dispersive spectroscopy
TEM	Transmission electron microscopy
TEPA	Tetraethylene penta amine
TGA	Thermogravimetriic analyser
CCS	Carbon Capture and Storage

XPS	X-ray photoelectron spectroscopy
XRD	X-ray diffraction
FWHM	Full width at half maximum
TSA	Temperature swing adsorption
PSA	Pressure swing adsorption
DEA	diethanolamine
GNPs	Graphene nanoplatelets
GBMs	Graphene-based materials

Chapter 1 – Introduction and Literature Review

1.1 Background of graphene-based monolith

Graphene, an extraordinary carbonaceous material, holds immense promise across a range of domains, including electronics, catalysis, energy applications, and adsorption. Monolithic nanomaterials stand out for their substantial CO_2 capture capacities, distinguishing them from metal-organic frameworks or zeolites [1–6]. Sustainable technologies typically serve as the foundation for a wide range of goods and services that enhance the quality of life, save expenses, and minimize or completely eliminate their negative effects on the environment. The chemical process industry's sustainable development depends on the utilization of graphene-based monoliths. They facilitate the environment-friendly synthesis of products by consuming less energy and, in some situations, preventing the creation of waste and byproducts. The so-called integrated approach to environmental protection, which includes, among other things, the integration of multiple processes, including chemical reaction, separation, heat exchange, and momentum transfer, benefits greatly from the use of monoliths, especially when implemented in an organized manner [7–9]. Among the various porous carbonaceous materials, graphene oxide (GO) stands out, recognized for its potential in CO_2 capture [10]. This unique property makes it a compelling candidate for optimizing adsorption efficiency [11,12]. From Greek, the word "monolith" was derived. Mono, which means "single," and lithos, which means "stone," are combined to create this word. The term "honeycomb structure" can be used to describe a monolith structure; however, in technical terms, "monolith" refers to a considerably broader meaning—generally, a massive, monolithic block made of a single building material [9]. The fabrication of monoliths graphene oxide-based materials by self-assembly process involving graphene oxide [13,14]. The material is characterized by its hexagonally arranged two-dimensional graphitic structure with sp^2 and sp^3 hybridization of carbon atoms [15]. Notably, monolithic graphene oxide (MGO) boasts a multifaceted surface chemistry, encompassing oxygen functional groups such as carboxyl, carbonyl, hydroxyl, and epoxy, distributed predominantly in the basal planes and outer regions [16–18]. MGO constitutes a three-dimensional porous structure with remarkable properties, including reticulated porosity, expansive surface area, lightweight nature, and flexibility, rendering it particularly suitable for diverse applications, notably adsorption processes [13,14,19–21]. In the context of escalating anthropogenic CO_2 emissions, the chemical industry's role in environmental deterioration is undeniable [22–25].

1.2 Climate change and CO_2 emission

Carbonaceous products cause global warming due to the emission of combustion and burning of fossil fuels, as well as increased motor vehicle practice. The key greenhouse gases influencing global climate change encompass CO_2, CH_4, O_3, N_2O, PFCs, HFCs, and SF_6 [26,27]. The surge in CO_2 concentration is attributed to the activities of the energy, transportation, and industrial sectors, including facilities like steel mills and refineries, which generate greenhouse gases (GHGs) by combusting fossil fuels such as coal and oil [28–30]. Due to anthropogenic happenings, the chemical industry plays a vital role in increased CO_2 levels in the atmosphere and the environment [22–25]. Thus, released anthropogenic CO_2 is utilized by various factors [31]. So, CO_2 capture technology plays an essential role in decreasing the concentration of CO_2 in the atmosphere. Amine adsorption is growing and is widely utilized by CCS technology. However, the regeneration study of adsorbents is costly, which is the main drawback of this adsorbent [32]. CCS technology has been used for CO_2 capture of solid adsorbents as practicable alternatives. As per the guidelines set forth by the Environmental Protection Agency (EPA), the worldwide atmospheric concentration of carbon dioxide has surged by over 100 parts per million (44%) in the past 250 years. Figure 1.1 illustrates the global emissions of greenhouse gases from 1950 to 2020. This increase is evident in the shift from 275–285 parts per million during the pre-industrial era to approximately 410 parts per million in 2021, with projections suggesting a potential rise to around 450 parts per million by 2025. Taking land sector sequestration into consideration, emissions experienced a 6% increase in 2021. The predominant factor driving this uptick in greenhouse gas emissions was the heightened combustion of fossil fuels, leading to a 7% surge in CO_2 emissions compared to 2020. The primary catalyst for this spike in emissions from fossil fuel use was the economic recovery following the peak of the COVID-19 pandemic. The consequential reliance on fossil fuels for energy needs has, in turn, contributed to a rise in the average global temperature, resulting in the retreat of glaciers, elevated sea levels, and increased surface ice melting [33,34]. Over the past few decades, there has been a notable reduction in Arctic ice, with a nearly 40% shrinkage observed. Additionally, global sea levels have risen by 0.20 meters from 1901 to 2020. The escalation in CO_2 levels has led to a 0.1 pH reduction, resulting in increased ocean acidity and consequential impacts on marine life [35–37]. Furthermore, there is a discernible trend toward the heightened occurrence of large-scale storms, heatwaves, droughts, torrential rainfall, and wildfires in recent years. Therefore, there is a consideration to stabilize CO_2 concentration at 450 ppm. This escalating trend in CO_2 levels is projected to result in an increase in the average global temperature ranging from 2 to 6 °C by the end of the twenty-first century [38,39]. Figure 1.2 illustrates the Inventory of U.S. Greenhouse Gas Emissions and Sinks from 1990 to 2021.

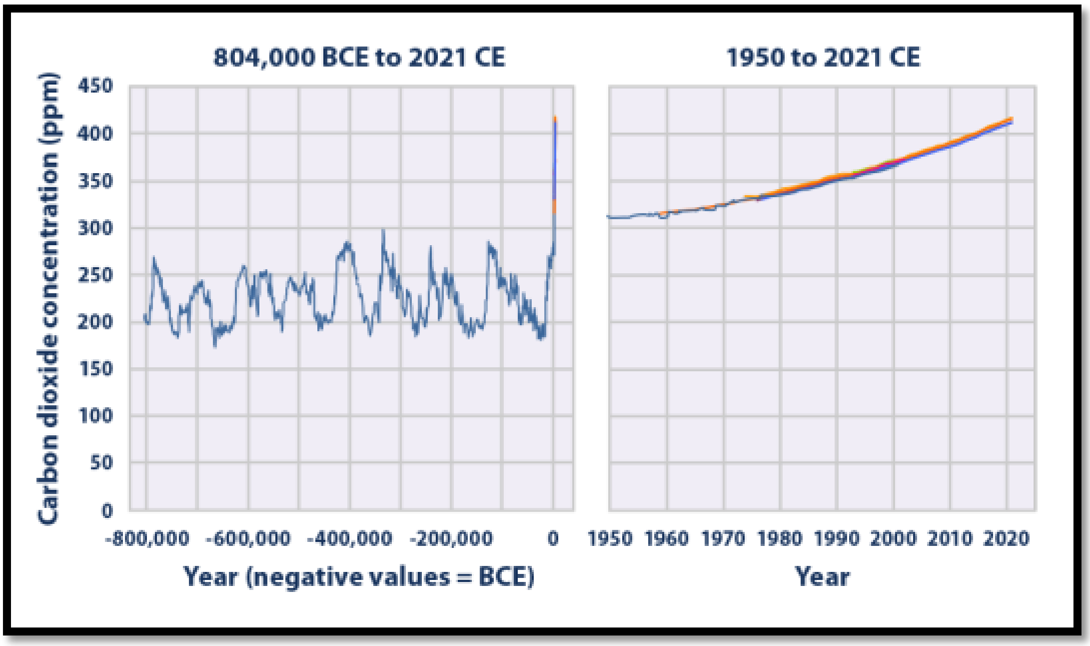

Figure 1.1 Global emissions of greenhouse gases from 1950 to 2020.

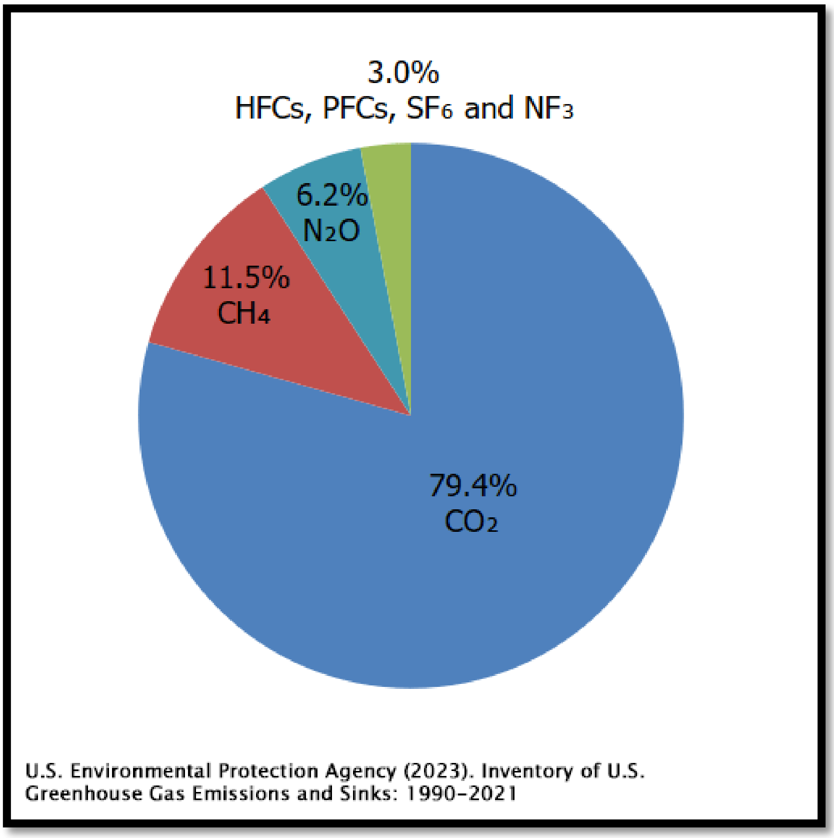

U.S. Environmental Protection Agency (2023). Inventory of U.S. Greenhouse Gas Emissions and Sinks: 1990-2021

Figure 1.2 The Inventory of U.S. Greenhouse Gas Emissions and Sinks: 1990–2021.

1.3 Carbon dioxide capture and sequestration

Figure 1.3 illustrates the comprehensive CCS technique, encompassing the extraction of CO_2 from energy sources with subsequent containment and storage, preventing its release into the environment. Several pivotal considerations impact the cost implications of applying CCS to fossil fuels, such as the scale of the capture plant, fuel costs, distance from capture site to storage facility, and technological characteristics of the power plant, among others. A negligible portion of the overall cost is attributed to the pipeline's transportation of compressed CO_2 to the storage site [35].

1.4 CO_2 capture technologies

Illustrated in Figure 1.3, the fundamental concept of CCS involves the initial capture of CO_2 emissions. There are essentially three distinct carbon capture methods: (1) oxy-fuel combustion, (2) pre-combustion, and (3) post-combustion. These methods vary depending on the fuel source, CO_2 partial pressure, and gas flow pressure. Figure 1.4 provides a concise overview of the CO_2 capture strategies. In the oxy-fuel combustion process, akin to the post-combustion system, the primary approach involves the separation of O_2 from N_2. In this method, the fuel undergoes combustion in oxygen, causing the separation of O_2 from N_2 before the separation of CO_2 from N_2. Condensation simplifies the separation of the resulting flue gas, predominantly composed of CO_2 and steam. The CO_2 capture process preceding combustion, known as pre-combustion, involves the conversion of fossil fuels into syngas, primarily composed of CO and H_2. Subsequently, additional H_2 and CO_2 are generated by further reacting CO with steam. The extracted CO_2 is then stored, while the high concentration of H_2 gas can serve as a valuable energy source. In contrast to post-combustion, pre-combustion CO_2 separation seems more energy-efficient and cost-effective [40]. Ensuring the sequestration of CO_2 from NO_x and SO_2 flue gas, post-combustion involves the absorption of CO_2 after burning fossil fuels with air. Refer to Table 1.1 for a comprehensive breakdown of the pros and cons associated with different carbon capture strategies.

Table 1.1 Pros and cons of carbon capture techniques.

Types of carbon capture	Pros	Cons
Pre-combustion carbon capture	Economical	Required comprehensive support system
	Increased CO_2 concentration and elevated output pressure serve to enhance sorption efficiency.	Inefficiencies in the water-gas shift reaction contribute to suboptimal performance.
Post-combustion carbon capture	A more economically efficient approach to harnessing energy from fuel.	The regeneration of solvents necessitates a significant energy input.
	Relevance across a wide spectrum of pressure and temperature conditions.	The solvent content is limited by its viscosity and tendency to foam.
	Elevated kinetics performance.	Degradation of the solvent
Oxy-fuel combustion carbon capture	Decreased gas volume requiring processing and a reduced need for boiler size.	Burning pure oxygen poses a challenging task.
	CO_2 separation is not required	The substantial production costs associated with cryogenic production lead to high expenses.
	Capability to decrease energy consumption when employing membranes.	Diminished process efficiency.

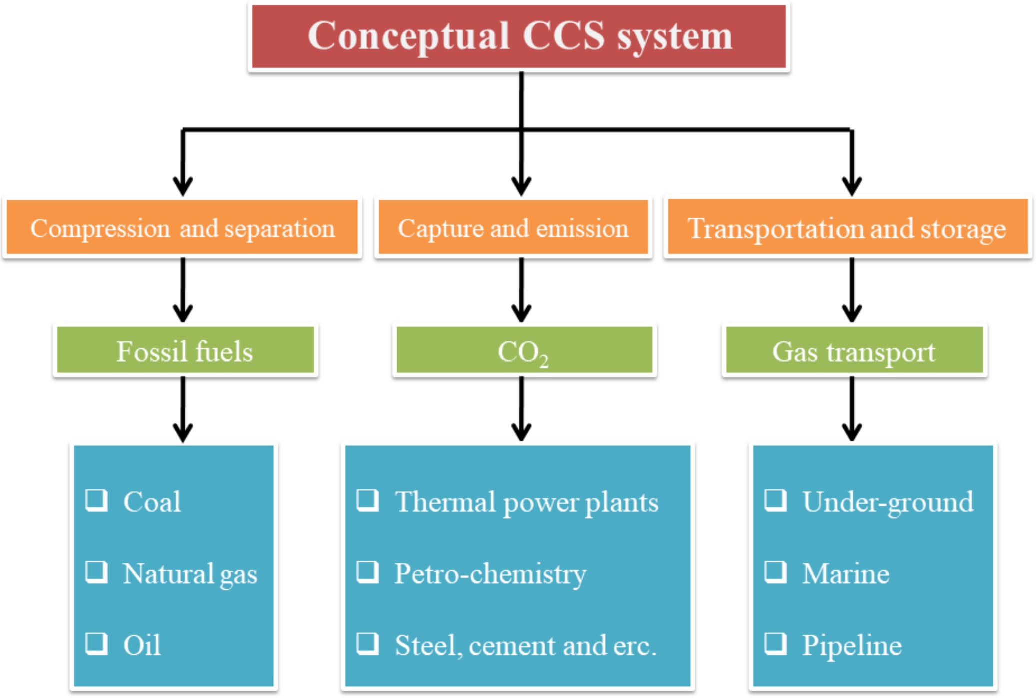

Figure 1.3 Principle of the CCS.

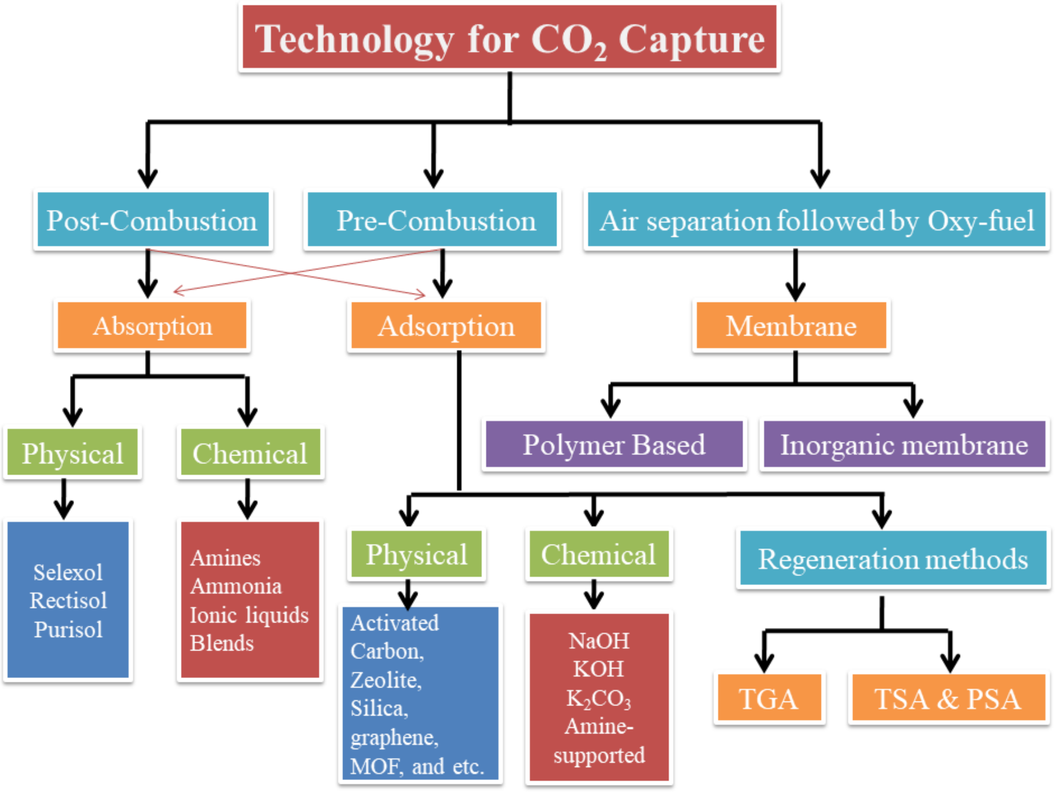

Figure 1.4 Types of CO_2 capture technologies.

1.4.1 Absorption

Within the petroleum and chemical sectors, the absorption carbon capture technique, depicted in Figure 1.4, stands out as the most developed and well-established method for CO_2 separation. CO_2 is chemically absorbed from the exhaust gas into an absorbent solution during this procedure, including amines like rectisol (chilled methanol), ammonia solution, diethanol amine (DEA), and methyldiethanol amine (MDEA), among others. This leaves the residual gas stream unburdened as it passes through the absorption column [41–43]. Methylethanol amine (MEA) emerged as the most effective in CO_2 absorption, demonstrating an impressive absorption rate of nearly 90% of the gas. Presently, a coal-fired power station has conducted successful tests on a 1tCO_2/h pilot plant, showcasing its capabilities using a 30% MEA solution [44,45]. Due to its faster reaction rate compared to MEA, piperazine has garnered attention, as has an anion-functionalized ionic liquid [46]. However, challenges arise due to piperazine's inferior volatility compared to MEA [46,47].

1.4.2 Adsorption

Adsorption using solid adsorbents has received much attention due to its ability to reduce the energy penalty. Its imminent applicability is supported by several advantageous qualities, including high adsorption capacity, selectivity, rapid kinetics, and robust mechanical and thermal stability [48]. As a practical alternative, solid adsorbents have garnered attention for their CO_2 capture capabilities, including many solid adsorbents have been observed for CO_2 adsorption [49], likely activated carbon [50–53], Zeolite [54,55], silica [56,57], graphene-based materials [13,14,24,58–63]. Notably, monolithic solid sorbents offer a straightforward route for CO_2 capture, leveraging their distinct porous structures, graphitic nature, stability, and versatility, as exemplified by graphene oxide (GO) [10] to enhance adsorption efficacy [11,12,58]. Based on the literature review, we have developed monolithic materials. The resultant materials have various characteristics and properties, such as being lightweight, low density, able to deform and absorb energy, open porosity, good morphology, high surface area, excellent CO_2 adsorption capacity, and many more.

1.4.3 Membrane separation

A membrane crafted from either polymer or ceramic is utilized to selectively permit the passage of carbon dioxide while obstructing other constituents of the flue gas. The membrane, a pivotal element in this method, incorporates both ceramic and polymer materials. It features a substantial, cost-effective, non-selective layer that furnishes mechanical support for the adjoining thin, selectively permeable layer [64]. The primary challenge in this process lies in the low pressure and low CO_2 content. This technique is applied for the extraction of CO_2 from natural gas and the separation of O_2 from N_2.

1.5 The mechanism underlying the adsorption process

Adsorption can be envisioned as the dynamic interplay of equilibrium, diffusion, and reaction processes involving the transfer of molecules from a liquid or gas phase onto a solid surface. This intricate phenomenon occurs as the molecules traverse the channels within a densely packed column, either concurrently or counterfactually [65]. The primary practical determinants of adsorption capacity are the reaction rate of adsorption and the mass transfer. Additionally, adsorption induces a deficiency in bonds on surface molecules, rendering them energetically favorable for further molecule adsorption. Conversely, desorption pertains to the incapacity of particles to disengage from the surface. A comprehensive explanation of the four stages in adsorption unfolds as follows: (1) Initially, isolated sites on the adsorbent’s surface initiate the adsorption of gas molecules at low pressure; (2) With an elevation in gas pressure, the area of adsorbed molecules expands, culminating in the formation of a monolayer; (3) Subsequent increments in gas pressure instigate the initiation of multilayer coverage, with smaller sample pores being filled initially; and (4) A further escalation in gas pressure leads to complete coverage of the sample, filling all of its pores [66]. In addition to this principle, it is crucial to underscore the adsorption mechanism, a pivotal aspect of the process. Adsorption processes can be categorized into two main types: chemical and physical. Distinctions between these mechanisms encompass factors such as specificity, molecular layer formation, surface area involvement, bonding characteristics, characterization methods, and the overall impact of various parameters. The mechanisms underlying chemical and physical adsorptions are depicted in Figure 1.5(a, b).

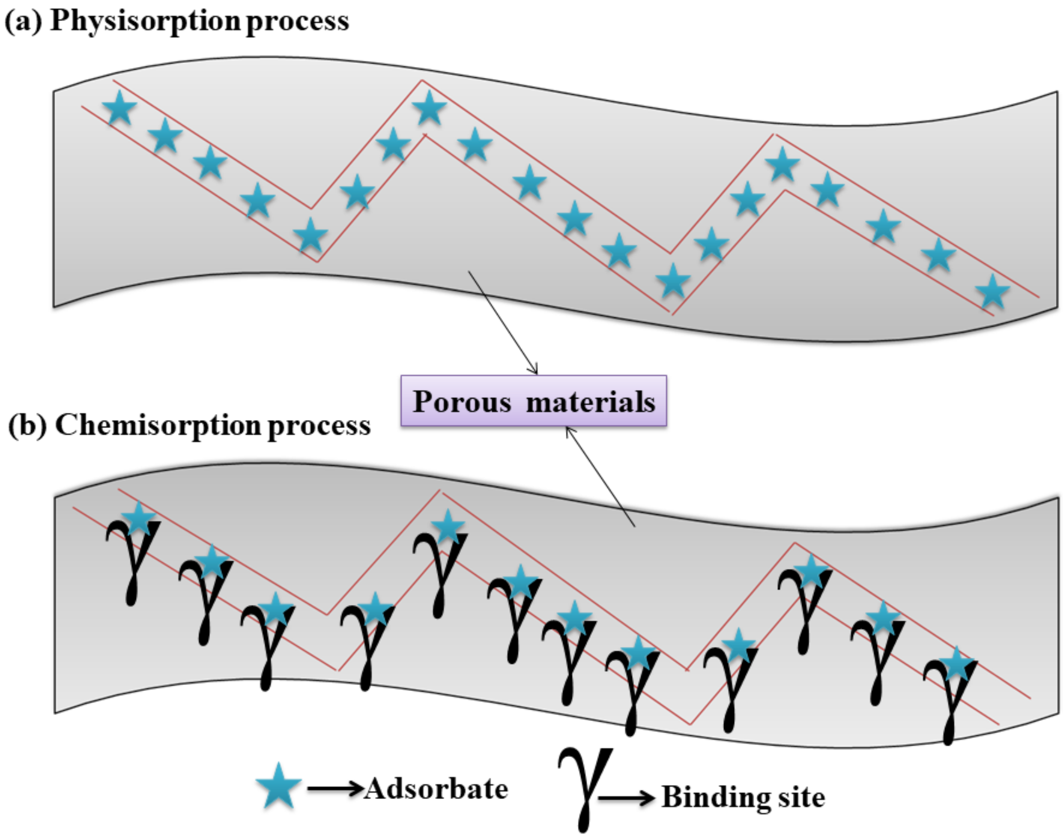

Figure 1.5 Mechanisms of (a) physisorption and (b) chemisorption process.

1.6 Types of adsorbents

The materials represent a subset of adsorbents suitable for CO_2 capture. This category aligns with other effective options, such as zeolites, silica, metal-organic frameworks, and carbon/graphene [39,67]. Considering the advantages and disadvantages of each adsorbent, including factors like low energy consumption, complete regenerability, and high adsorption capacity, is essential for optimizing the CO_2 capture process. Achieving compliance with both NETL and DOE standards through a singular solution poses a significant challenge. Ultimately, the most successful adsorbents will be those capable of performing effectively in real-world CO_2 collection processes.

1.6.1 Zeolite-based adsorbents

Adsorbents commonly studied for CO_2 capture encompass zeolites like zeolite Y [68,69], 4A [70], 5A [71], and 13X [72,73]. Zeolite materials exhibit a range of advantageous properties, such as surface area porosity, which makes them easily adaptable to individual requirements and various applications. Cations like Li, Na, and Al in zeolites may influence the heat of adsorption of CO_2, as an escalation in negative charges correlates with the surge in the Q_{st} [74]. The extensive range of pore structures within zeolites, including tiny pores with six, eight, or nine tetrahedral rings; medium pores with ten tetrahedral rings; and large pores with one-membered rings and ultra-large structures, collectively contribute to the diverse adsorption capabilities of zeolites [75]. The pores of modified zeolites can expedite the swift passage of gases, enhancing CO_2 adsorption efficiency and facilitating effective CO_2 regeneration [76]. Employing this method enables the efficient integration of the zeolite phase, a factor of potential significance at an industrial scale. Further exploration of the efficacy of CO_2 adsorption using PEI-modified 13X zeolite reveals a notable 2.3-fold increase in CO_2 absorption capacity compared to unmodified 13X zeolite [77]. The robustness of this study lies in the prospect that the branched structure of the impregnated molecular amine zeolite composite could enhance adsorption potential under optimal reaction parameters. The kinetic modeling study offered insights into this phenomenon. The anticipation was that the engineered zeolite-based adsorbent could provide an economical approach for manipulating flue gas conditions, extending its applicability across a broader spectrum of CO_2 capture applications. Additionally, the study delved into exploring the impact of PEI types (branched or linear) and molecular weight on the efficiency of CO_2 collection [78]. The latter's results showed that the adsorption capability of CO_2 reduced as PEI's molecular weight increased. The adsorption capacity of branched PEIs (impregnated polyethyleneimine) was actually higher than that of linear PEIs because of their increased mobility.

1.6.2 Silica-based adsorbents

Mesoporous silica materials stand out in CO_2 capture applications due to their expansive surface area, customizable porous structure, and enhanced gas diffusion capabilities. The heightened concentration of surface hydroxyl groups facilitates a more seamless grafting process for amine groups, consequently elevating the adsorption capacity. Pioneering in its approach, this study marks the first of its kind to employ amine-impregnated mesoporous silica, coupled with thermogravimetric analysis, for effective CO_2 adsorption [79]. Polyethyleneimine (PEI) was impregnated at different loadings onto MCM-41 silica, renowned as the "molecular basket," employing the wet impregnation method [80–83]. Additionally, the study investigated how moisture influenced the adsorption capability of PEI-impregnated MCM-41 [81]. The thermogravimetric investigation of diethanolamine (DEA) impregnation in MCM-41 (PE-MCM-41) revealed a noteworthy capacity of 2.93 mmol g^{-1} under a 5% CO_2 atmosphere at 25 °C [50,84–86]. Tetraethylene pentaamine (TEPA) and polyethyleneimine (PEI) were impregnated onto monolithic silica. Under identical conditions, it was observed that the maximum gravimetric adsorption capacity reached 3.75 mmol g^{-1} for monolithic silica with 65% PEI loading, surpassing the performance of PEI-modified KIT-6 [87,88]. However, a limitation associated with TEPA use became evident, as the decrease in uptake capacity was observed after undergoing five adsorption/desorption cycles. SBA-15-TEPA retained 86% of its initial CO_2 adsorption capacity after undergoing ten adsorption-desorption cycles utilizing a simulated gas combination [89]. This substantial difference could be attributed to the enhanced affinity of the primary amine sites for the Lewis acid (CO_2) at lower pressures [90].

1.6.3 Metal organic frameworks-based adsorbents

By amalgamating organic ligands and metal cations, MOFs emerge as a contemporary category of solid sorbents. MOFs employ three primary approaches—those with open metal sites, ultra-microporous architectures, and amine-functionalized MOFs—to effectively capture CO_2 [91]. The phrase "coordinated unsaturated sites" is commonly known as open metal sites within MOFs [92,93]. Metal ions with strong basic properties, such as Ca, Mg, Zn, Li, Mn, and Cu, hold the potential for constructing highly efficient MOF structures. To optimize the adsorption of CO_2 through these open metal sites, it is essential to aggregate metal particles systematically using a controlled process. Additionally, integrating traditional magnesium and copper metal ions, along with urea groups, enhances CO_2 adsorption [94–96]. Amine-functionalized MOFs hold the potential for CO_2 capture due to the tunability offered by these functional groups [25,97,98]. Indeed, nitrogen atoms, constituting the amine group, represent a specific type of electronegative atom. Apart from their inclination to form triple bonds with themselves and other elements, nitrogen atoms can create robust bonds, frequently employed to provide active sites for CO_2 adsorption. Two commonly used methods for grafting amine functional groups onto MOFs are well-established. The initial step involves creating a strong bonding contact between the positive nitrogen atom and the vacant orbital of the open metal cation, facilitating the attachment of the amine to open metal sites. Subsequently, organic ligands are linked to the amine group. Notably, employing ethylenediamine (EDA) for amine grafting has proven to significantly enhance both CO_2 adsorption capacity and kinetics [99,100] and acid-grafted chitosan nano adsorbent [101]. The nanomaterials mentioned earlier exhibit potential as CO_2 adsorbents due to their capacity to minimize the energy required for regeneration and separation [102]. These procedures are broadly categorized into two primary families: physical and chemical changes, representing the most widely employed methods.

1.6.4 Carbon/graphene-based adsorbents

Carbon-based adsorbents, with a notable emphasis on materials such as graphene and carbon nanotubes (CNTs), are widely acknowledged as crucial CO_2 adsorption agents due to their abundant availability, cost-effectiveness, expansive surface area, versatile pore structure, capacity for surface functionalization, and straightforward regeneration process. Graphene is commonly described as a dense sheet of sp^2-bonded carbon atoms arranged in a hexagonal pattern. Various forms of graphene exist, including graphene oxide, graphene nanoplatelets (GNPs), single-layer graphene, few-layer graphene, multilayer graphene, and reduced graphene oxide, which stand out as the primary derivatives of graphene. Graphene derivatives exhibit the capability to autonomously organize into porous three-dimensional materials [13,14,58,103]. As an illustration, Chowdhury and Balasubramanian engineered meticulously structured graphene-based materials (GBMs) boasting a substantial specific surface area and an intricately interconnected hierarchical pore network [103,104]. Crucially, precise regulation of gas flow channels and pores through diverse stacking methods enables the attainment of resilient CO_2 adsorption/desorption cycles characterized by rapid adsorption kinetics and outstanding CO_2/N_2 stability. Furthermore, the integration of functional chemicals, such as oxygen-containing groups, has been proven to enhance the efficacy of porous materials for CO_2 absorption [14,24,95]. The synthesized three-dimensional hydrothermal reduced graphene oxide (3D-HrGO) exhibits a substantial pore capacity and expansive surface area [105,106]. Owing to its distinctive textural features and a diverse array of chemical interactions, such as hydrogen bonds forming between CO_2 and HrGO, polar contacts, and acid-base interactions, the graphene-based adsorbent showcased superior CO_2 capture efficiency. To augment the CO_2 absorption capabilities of both CNTs and graphene-based adsorbents, incorporating heteroatoms with functional groups like N, S, O, and P as dopants has proven to be an effective enhancement strategy [107,108] Graphite, commonly employed in the production of carbon nanotubes (CNTs), boasts an extensive surface area and a tubular structure, rendering it highly porous and potentially valuable for applications involving gas adsorption and storage. The outer diameter of both single and multilayer nanotubes typically falls within the range of three to one hundred nanometers. Moreover, they exhibit excellent electrical and thermal conductivity. The advancement of high-performance adsorbents relies on surface modification of CNTs, achieved through either covalent or non-covalent functionalization. These inherent characteristics render them highly promising materials for the efficient and selective adsorption and desorption of carbon dioxide. To optimize CO_2 adsorption efficiency, researchers are currently exploring the surface modification of grafted adsorbents using polymerizing materials [109]. This process involves coating MWCNTs to enhance both pore volume and surface area. Notably, polyethyleneimine (PEI) has been recently immobilized onto CNTs to fabricate microtubular sorbents [110]. Similarly, a CO_2 sorbent was fashioned through the immobilization of TEPA onto functionalized CNTs. The researchers envisaged that the combination of MWCNTs with the TEPA sorbent could be employed for CO_2 adsorption [111]. In addition, modified CNTs incorporating CaO pellets have been explored due to their cost-effectiveness and capacity to absorb substantial quantities of CO_2 [112].

1.7 Thesis motivation and objectives

Many researchers have been observed attempting the creation of carbon adsorbents through methods such as the physical or chemical activation of initial materials or direct carbonization. Moreover, they endeavored to evaluate the absorption capability predominantly at room temperature in a static environment. However, a limitation in their studies is evident in both the synthesis and performance evaluation aspects. Furthermore, assessing adsorbents under static conditions yields higher uptake capacity values, which may not accurately portray their performance in real-world flue gas applications. To bridge this gap, a study was conducted wherein the textural properties were augmented using the self-assembly process of a graphene oxide-based adsorbent. This involved initially reducing oxalic acid (OxA)/malic acid (MaA) with various mass ratios, followed by the physical and chemical activation of a subset of monolithic adsorbents. The study concluded with an investigation into CO2 adsorption for the same set of adsorbents. Moreover, CO_2 adsorption was conducted using select monolithic adsorbents in dynamic conditions, which were considered more realistic than static conditions.

The objectives are:

- To synthesize and characterize the monolithic graphene oxide (MGO) based adsorbents.
- To modify/activate the as-synthesized MGO adsorbents by the physical or chemical activation process.
- To evaluate the CO_2 adsorption performance of as-synthesized adsorbents at various temperatures and CO_2 concentrations.
- To study the adsorption isotherms and kinetics using different models.

1.8 Thesis overview

The thesis is structured into six chapters, focusing on the preparation of three distinct types of monolithic graphene oxide-based adsorbents. These were developed through the self-assembly process of graphene oxide, followed by reduction using oxalic acid (OxA)/malic acid (MaA) with varying mass ratios. Samples were prepared and activated through both physical (UV treatment) and chemical ((NaOH/KOH) methods to enhance their efficacy in capturing CO_2. Chemical, surface, and textural characteristics were meticulously examined and characterized. Dynamic adsorption-desorption studies were conducted under flue gas simulation conditions to evaluate their CO_2 capture capabilities. Scheme 1 illustrates the schematic overview of the entire thesis project.

Chapter 1 (Introduction and Literature Review): This section outlines current environmental challenges, provides a brief overview of CO_2 capture, and delves into diverse adsorbent types, with a specific focus on carbon/graphene-based adsorbents, aligning with the primary focus of the current study.

Chapter 2 (Experimental Materials and Characterization Methods): This chapter provides an overview of the experimental procedures conducted in this research, organized into distinct sections. Firstly, elaborate on the materials, chemicals, and experimental methods employed to characterize and assess the performance in adsorption-desorption experiments. Additionally, the chapter presents the experimental setup employed for the adsorption study. Lastly, this section is dedicated to the discussion of diverse adsorption kinetic models, isotherm models, and thermodynamic parameters.

Chapter 3: This section delves into the synthesis of monolithic graphene oxide-based adsorbent through the self-assembly process of graphene oxide and subsequent oxalic acid reduction with varying mass ratios, further activated through UV treatments. The CO_2 adsorption performance of the prepared monoliths has been thoroughly assessed. The optimal sample from this series underwent additional examination under simulated flue gas conditions at diverse adsorption temperatures. Comprehensive investigations encompass the kinetics, isotherms, and thermodynamics of CO_2 adsorption on the optimized sample, complemented by an energy calculation for the desorption process.

Chapter 4: We synthesized a robust monolithic reduced graphene oxide through a self-assembly reduction process of graphene oxide at 90 °C, employing varying weight ratios of oxalic acid (1:1, 1:0.500, and 1:0.250). Subsequently, the as-synthesized monoliths underwent carbonization and chemical activation, with NaOH weight proportions of 1:1, 1:2, and 1:3, at an activation temperature of 600 °C. The properties of the synthesized graphene-based adsorbent were systematically explored, and its CO_2 adsorption effectiveness was observed under dynamic conditions. The optimized sample underwent comprehensive investigation, including the fitting of kinetic and isotherm models to experimental data, along with the calculation of thermodynamic parameters.

Chapter 5: We have synthesized monolithic reduced graphene oxide-based adsorbents through a meticulous self-assembly process involving different mass ratios of GO/malic acid (MaA) (1:0.250, 1:0.500, and 1:1 by weight). Building upon this foundation, we further modified MGO 0.250 through KOH by chloroacetic acid method, leading to the creation of MGO 0.250_KOH, which was subjected to CO_2 capture assessments. The comprehensive investigation encompassed an array of parameters, including morphology, specific surface area, crystal defects, functional group identification, and CO_2 capture efficiency.

Chapter 6 (Conclusions and recommendations): This section succinctly summarizes the presented data and provides references for future research.

Chapter 2 – Experimental Materials and Characterization Methods

2.1 Materials

Graphite powder (GP), $NaNO_3$, H_2SO_4, $KMnO_4$, H_2O_2, HCl, and oxalic acid ($C_2H_2O_4$) were used to synthesize monolithic reduced graphene-oxide. High-purity nitrogen gas (concentration 99.98 %) and carbon dioxide gas (concentration 50 %, 40 %, and 20 %) were purchased from Sigma Gases & Services (New Delhi), India, for CO_2 capture performance purposes.

For synthesis, a diverse range of materials, including graphite powder, $NaNO_3$, H_2SO_4, $KMnO_4$, H_2O_2, HCl, $C_2H_2O_4$, and NaOH. In the pursuit of optimizing CO_2 capture performance, Sigma Gases & Services, based in New Delhi, India, supplied high-purity nitrogen gas with a concentration of 99.98%, along with carbon dioxide gases at concentrations of 50% and 20%.

Graphite powder, $NaNO_3$, H_2SO_4, $KMnO_4$, H_2O_2, HCl, malic acid ($C_4H_6O_5$), chloroacetic acid ($C_2H_3ClO_2$), and KOH from Sigma-Aldrich were used to synthesize KOH-treated monolithic graphene oxide-based adsorbent. High-purity nitrogen gas (concentration 99.99 %) and carbon dioxide gas (concentration 99.98 %) were purchased from Sigma Gases & Services (New Delhi), India, for CO_2 capture performance purposes.

2.2 Characterization methods

2.2.1 X-ray diffraction (XRD)

The XRD patterns of the prepared adsorbents were collected by Rigaku SmartLAB SE (Japan), analyzing adsorbents in the 5^o to 60° scan rates with the 2-θ range. When exposed to Cu-Kα irradiation with λ is 1.4999 Å, the diffractograms were recorded at 40 kV and 30 mA. Steps value of 1.002° m^{-1} and a step time of 10^o m^{-1} were used.

2.2.2 Raman spectroscopy

HORIBA LabRAM HR Evolution Raman spectrometer (JOBIN YVON Technology) recorded the Raman spectra of prepared samples in the Raman shift range 500 to 3500 cm^{-1}. The 50x magnification of an object that possesses a long working distance, 1% laser intensity capacity, and the size of lenses 100 µm were applied with the collection of scattered light. Furthermore, the instrument was employed to scrutinize the existence and placement of the D-(disordered) and G-(graphitic) peaks, along with assessing their respective intensity ratios.

2.2.3 Fourier transform infrared (FTIR) spectroscopy

The chemical structure and surface functional groups of the adsorbents were estimated by the FTIR spectra assembled on a SHIMADZU IRTracer-100 (FOURIER TRANSFORM INFRARED SPECTROMETER). Samples were scanned with the wavenumber region 4000 to 400 cm^{-1} by a 35±1 scan rate.

2.2.4 Thermogravimetric analysis (TGA)

TGA measurements of samples were performed using a Thermal analyzer instrument (TA - Q500). In the analytical procedure, a quantity ranging from 5 to 10 mg of the sample was carefully placed into a platinum pan. Subsequently, the sample underwent controlled heating, starting from 25 °C and reaching 700 °C at a consistent rate of 10 ºC per minute, all conducted under a continuous N_2 flow rate at 50 ml per minute.

2.2.5 Scanning electron microscopy (SEM)

JSM-6510 was used to assess the morphology of the adsorbents at a 20 kV accelerating voltage. To avoid sample charging issues, the sample was coated with a 50 µm thickness using an automatic sputter coater (Polaron) prior to analysis.

2.2.6 Field emission scanning electron microscopy (FE-SEM)

CARL ZEISS SIGMA-500 was used to assess the morphology of the adsorbents at a 20 kV accelerating voltage. To avoid sample charging issues, the sample was coated with a 50 μm thickness using an automatic sputter coater (Polaron) prior to analysis.

2.2.7 High-resolution transmission electron microscopy (HR-TEM)

JEOL JEM-2100 was used to evaluate the morphology of the adsorbents operating at a voltage of 200 kV. Prior to analysis, the samples were prepared by applying a drop of the carbon adsorbent dispersion in toluene onto a carbon-coated copper grid.

2.2.8 Surface area and pore size distribution

BET analysis of N_2 adsorption-desorption isotherm was performed at 77 Kelvin on an automated gas sorption analyzer (Autosorb-IQ, Quntachrome Instruments). For the adsorption measurements, each adsorbent was degassed at 273 Kelvin for six hours. The specific surface area (external and internal surface area) and porosity (%) were calculated by using nitrogen adsorption uptake and relative pressure (p/p_o). The BET surface area achieved from the N_2 adsorption isotherms at 77 Kelvin and pore size distributions (PSDs) achieved through the Barrett-Joyner-Halenda (BJH) methods.

2.2.9 X-ray photoelectron spectroscopy (XPS)

Thermo Fisher SCIENTIFIC instrument (ESCLAB QXi Inc., US), XPS employs carried out utilizing a monochromatic X-ray source. A monochromatic Al-kα source, operating with a 15 kV anode potential, was employed in the Kratos Axis Ultra DLD system for this purpose. The high-resolution spectra were acquired with an emission current of 10 mA and a pass energy of 20 eV, whereas the survey spectra were captured using a pass energy of 50 eV. A constant pressure of 2×10^{-9} torr was maintained within the analytical chamber. The C1s and O1s peak binding energy was used for surface charging and calibration. Origin-software was used for data processing, and the spectra were fitted with mixed Gaussian-Lorentzian baseline subtraction and curve deconvolution to determine the atomic composition.

2.3 Performance evaluation of adsorbents

2.3.1 Adsorption/desorption study setup

The modified thermogravimetric analyzer was used to obtain the CO_2 adsorption capacities of the synthesized adsorbents under different operating conditions (adsorption temperatures, 25°C to 50 °C and CO_2 concentrations flow 20 to 100 %). The adsorbent (~20 mg) was initially taken in a platinum pan and then heated at 150 ºC for two hours using N_2 flow (50 ml min^{-1}) to ensure the elimination of unwanted moisture. The furnace was then cooled to the desired adsorption temperature (25 and 100 ºC) for the respective CO_2 adsorption. Afterward, the N_2 gas was changed to CO_2 without any change in the flow rate. The weight gain of the adsorbent with time was observed to estimate CO_2 uptake capacity. Now, N_2 was again passed to the gas stream for the desorption process at 150 °C for two h and purging with 100 % N_2. The regenerability of the adsorbents was investigated by repeating this adsorption-desorption process four times.

2.3.2 Experimental data evaluation

The TA Instruments (TGA Q_{500}, United States) was used to evaluate the adsorption capacity of a monolithic sorbent by Equation 2.1:

$$q_t = \frac{\mathrm{m(t)} - \mathrm{m}(t_0)}{44(m_0)} \times (mol/gm) \qquad (2.1)$$

The mass of the introduced effective solid monolithic sorbent is indicated as (m_o), the initial weight signal value at the onset of adsorption is denoted as m(t_o), and the weight signal value at time t during the adsorption process is represented as m(t).

2.3.3. Selectivity measurements

Selectivity was calculated for CO_2 over N_2 (SCO_2)) using Equation 2.2 [59].

$$S_{CO_2} = \frac{x_{CO_2}/x_{N_2}}{y_{CO_2}/y_{N_2}} \qquad (2.2)$$

Where, x_{CO_2} and x_{N_2}= mole fractions of CO_2 and N_2 in the adsorbed phase, y_{CO_2} and y_{N_2} = molar ratios of CO_2 and N_2 in the gas phase.

Equation 2.3 [59,113] can subsequently be utilized to determine the purity of the captured CO_2.

$$Purity\ (\%) = \frac{x_{CO_2}}{x_{CO_2}+x_{N_2}} \tag{2.3}$$

The selectivity experiments focusing on CO_2/N_2 were executed at 25 °C, 1 bar pressure and CO_2/N_2 binary gas mixture with 50 % CO_2 and 50 % N_2 concentration flows.

2.3.4 Dynamic CO_2 adsorption/desorption measurements

The breakthrough curves for the samples assess the dynamic CO_2 adsorption capacity of ca. 1.0 mmol g^{-1} at 25 °C, 1 bar pressure, and CO_2/N_2 binary gas mixture with 50 % CO_2 and 50 % N_2 concentration flows. This shows that N_2 has a lower adsorption capability than CO_2. Initial values of C/C_o for $N_2 > 1$ indicate that N_2 initially occupies the adsorbent's active sites, but with time, N_2 is gradually replaced by CO_2, revealing that the adsorbent has a higher affinity for CO_2 [51,114,115].

2.4 Adsorption kinetics study

In order to determine the adsorption rate and the adsorbent's capacity to adsorb a larger amount of adsorbate, adsorption kinetic studies are necessary [116–120], the formula provided in Equations 2.5, 2.7, and 2.8.

2.4.1 Pseudo-first-order model:

Equation 2.4 was employed to successfully fit the pseudo-first-order adsorption model [121]:

$$\frac{dq_t}{dt} = k_1(q_e - q_t) \tag{2.4}$$

where, k_1 is the pseudo-first-order adsorption rate constant (min^{-1}). Integrating Equation 2.4 with boundary conditions: $q_t|_{t=0}$ =0 and $q_t|_{t=t}$ =q_t, yields

$$log = \frac{q_e}{q_e-q_t} = \frac{k_1}{2.303}t$$

This equation can be rearranged, and we get:

$$q_t = q_e\,(1 - e^{-k_1 t}) \tag{2.5}$$

Here, q_t (mmol g^{-1}) is the CO_2 adsorption capacity at any time t (in min), q_e is the capacity in mmol g^{-1} at equilibrium, and k_1 is the corresponding rate constant.

2.4.2 Pseudo-second-order model:

Equation 2.6 was employed to successfully fit the pseudo-second-order adsorption model [122]:

$$\frac{dq_t}{dt} = k_2(q_e - q_t)^2 \tag{2.6}$$

where, k_2 (g $mmol^{-1}$ min^{-1}) is the pseudos-econd-order rate constant. Integrating Equation 2.6 with initial conditions: $q_t|_{t=0}$ =0 and $q_t|_{t=t}$ =q_t, yields

$$q_t = \frac{k_2 q_e^2 t}{1 + k_2 q_e t} \tag{2.7}$$

Here, k_2 is the constant.

2.4.3 Elovich kinetic model:

Equation 2.8 was employed to successfully fit the Elovich adsorption model [123]:

$$q_t = \frac{1}{\beta}\, ln\,(\alpha\beta + 1) \tag{2.8}$$

Here, α initial adsorption rate and β desorption constant for the corresponding model constant and q_t is the amount adsorbed at the time (t).

2.4.4 Error evaluation:

Equation 2.9 was utilized for accurate error (%) evaluation.

$$Error\ (\%) = \sqrt{\frac{\sum\left[\left(q_{t(exp)} - q_{t(pred)}\right)/q_{t(exp)}\right]^2}{N-1}} \times 100 \tag{2.9}$$

Here, $q_{t(exp)}$ and $q_{t(pred)}$ are the respective experimental and predicted CO_2 adsorption capacities at any time (t), and N is the number of measurements.

2.5 Adsorption isotherms study

2.5.1 The Langmuir isotherm model:

Equation 2.10 was employed to successfully fit the Langmuir adsorption isotherm model [124]:

$$q_e = \frac{q_m K_L P}{1 + K_L P} \tag{2.10}$$

Here, q_e is the CO_2 adsorbed (mmol g^{-1}) at equilibrium, P is the CO_2 partial pressure in (atm), q_m is the maximum monolayer adsorption capacity, and K_L (atm^{-1}) the Langmuir constant.

2.5.2 The Freundlich isotherm model:

Equation 2.11 was employed to successfully fit the Freundlich adsorption isotherm model [125]:

$$q_e = K_F P^{1/n} \tag{2.11}$$

Here, $K_{.F}$ and n are the constants revealing the adsorption capacity and intensity, respectively. Also, n is the empirical constant associated with the adsorption driving force, and its values lie from 1 to 10.

2.5.3 The Temkin isotherm model:

Equation 2.12 was employed to successfully fit the Temkin adsorption isotherm model [126]:

$$q_e = B\, ln(K_T P) \tag{2.12}$$

where, K_T (atm^{-1}) and $B = RT/b$ with b (J mol^{-1})

2.6 Thermodynamics study

2.6.1 Thermodynamic parameters

Gibbs free energy, ΔG^0 (kJ mol^{-1}) estimated by using Equation 2.13, whereas standard enthalpy change, ΔH° (kJ mol^{-1}) as well as standard entropy change (ΔS^0) (kJ mol^{-1} K^{-1}) can be measured from Van't Hoff plot [127] using Equation 2.14. In addition, the Clausius-

Clapeyron equation [128] was applied to calculate the isosteric heat of adsorption, Qst (kJ mol^{-1}), represented in Equation 2.15.

$$\Delta G^{\circ} = -RT\ln\left(K_{eq}\right)$$

(2.13)

$$\ln\left(K_{eq}\right) = -\frac{\Delta H^{\circ}}{R}\frac{1}{T} + \frac{\Delta S^{\circ}}{R} \tag{2.14}$$

$$Q_{st} = -R\left[\frac{\partial \ln P}{\partial\left(\frac{1}{T}\right)}\right]_{q_e} \tag{2.15}$$

$$K_d = \frac{q_e}{C_e} \tag{2.16}$$

Where R (8.314 J mol^{-1} K^{-1}) is gas constant; Q_{st} (at a given q_e) is the isosteric heat of CO_2 adsorption,

2.6.2 Energy duty for desorption

By employing Equation 2.17, we determined the energy required for the desorption of adsorbed CO_2 on the adsorbent. Subsequently, Equation 2.18 was utilized to ascertain the sensible heat needed to elevate the temperature during the desorption process.

$$Q_{th} = Q_{st} + sensible\ heat \tag{2.17}$$

$$Sensible\ heat = \frac{C_p \Delta T}{adsorption\ capacity} \tag{2.18}$$

Where, C_p (J g^{-1} K^{-1}) = heat capacity.

Concerning activation energy, the isosteric heat of adsorption delineates the distinction between adsorption and desorption. Here is an illustration corresponding to the given Equation 2.19.

$$Q_{st} = -R\left[\frac{\partial \ln P}{\partial\left(\frac{1}{T}\right)}\right]_{q_e} \tag{2.19}$$

Here, q_e (kJ mol^{-1}).

Chapter 3 – UV Activated Oxygen-Enriched Monolithic Graphene Oxide-Based Adsorbents for CO_2 Capture

3.1 Synthesis of monolithic graphene oxide-based adsorbents

3.1.1 Synthesis of monolithic graphene oxide

Modified Hummer's method was used to synthesize graphene oxide (GO) [129]. Typically, the synthesis of monolithic graphene oxide was prepared by the self-assembly process of graphene oxide [13]. A measured amount (5 mg/ml) of GO aqueous dispersion was prepared by ultra-sonication for 1 hour. After that, this dispersion was stirred for 3 hours at 90 °C and cooled to room temperature, and then oxalic acid (OxA) was added to various mass ratios (by weight) of GO/OxA (1:1, 1:0.500, 1:0.250) mixture was prepared. This homogeneous mixture was then heated in a hot air oven for 2 hours at 90 °C to reduce and form a monolithic hydrogel. After that, the prepared wet monolith was cleaned and washed by centrifugation (at 7000 RPM for 10 minutes) to eliminate the extra OxA. Finally, the wet monolith was freeze-dried to remove the adsorbed water by HyperCOOL Cooling Trap HC3055 (Korea) at -55 °C and pressure of 0.6 mbar for 24 hours. Scheme 3 represents the synthesis route of monolithic graphene oxide-based adsorbents. The monolithic graphene oxides (MGOs) were prepared using different mass ratios of oxalic acid (OxA) by weight (mg), and each sample was assigned a specific name, as shown in Table 3.1.

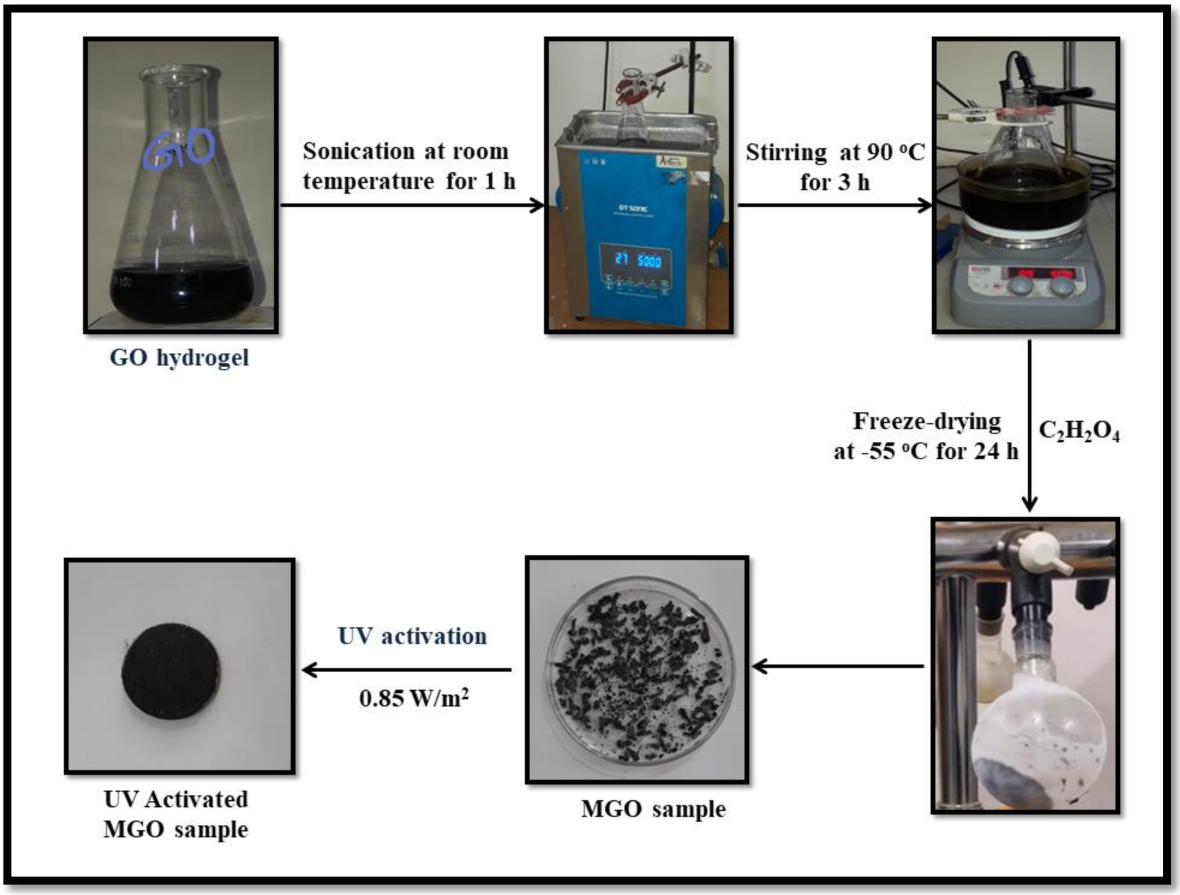

Scheme 3 Synthesis of the monolithic graphene oxide-based adsorbents.

Table 3.1 Preparation of MGOs in different mass ratios of GO: OxA (by weight in mg).

Samples	GO: OxA	Temp. (°C)	Sample volume (V)	Void volume (V_v)	Solid volume (V_s)	Porosity (n)	Density (g^{-1} cm^3)
MGO 0.250	1: 0.250	90	0.0785	0.0635	0.015	0.808	0.191
MGO 0.500	1: 0.500	90	0.0785	0.0605	0.018	0.770	0.229
MGO 1.000	1: 1.000	90	0.0785	0.0585	0.020	0.745	0.254

3.1.2 Activation of MGO 0.250 adsorbent by various UV-treatment times

UV light activation of MGO 0.250 was carried out in a cupboard equipped with UV light with an output energy of 350 to 360 nm. Here, MGO 0.250 was shown to UV treatment in variable times of 1 h to 15 h. The resultant samples were tagged as MGO 0.250 UV_x; here, x is activation period in h, and applying this method, we get to UV light-activated adsorbents and label them as MGO 0.250 UV_1, MGO 0.250 UV_2, MGO 0.250 UV_2.5, MGO 0.250 UV_5, MGO 0.250 UV_10, and MGO 0.250 UV_15 as shown in Table 3.2.

Table 3.2 UV treatment of MGO 0.250 adsorbent for different time durations.

Samples Name	Energy	Activation Time	Temperature	Intensity
MGO 0.250	-	-	-	-
MGO 0.250 UV_1	350 nm	1 h	25 °C	0.85 W/m^2
MGO 0.250 UV_2	350 nm	2 h	25 °C	0.85 W/m^2
MGO 0.250 UV_2.5	350 nm	2.5 h	25 °C	0.85 W/m^2
MGO 0.250 UV_5	350 nm	5.0 h	25 °C	0.85 W/m^2
MGO 0.250 UV_10	350 nm	10.0 h	25 °C	0.85 W/m^2
MGO 0.250 UV_15	350 nm	15.0 h	25 °C	0.85 W/m^2

3.2 Characterization of adsorbents

3.2.1 Characterization of monolithic materials

The GO-based monoliths were synthesized through the oxalic acid (OxA) reduction of graphene oxide in an aqueous dispersion at 90 °C, employing various OxA and GO mass ratios. The reduction temperature plays an essential role in determining the GO reduction process and governs the reduced graphene oxide (rGO) and its structure. GO platelets are widely recognized to include epoxy, –OH, and –COOH groups [130]. During reduction, these groups are eliminated. The dispersion rises throughout reduction, and the resulting rGO self-organizes to minimize the interface. This reduction-induced transformation underpins the emergence of a porous and hierarchically organized morphology within the monolithic constructs. Intriguingly, the density of the monoliths exhibits an ascending trajectory with the augmentation of OxA content. This correlation suggests a denser, more tightly knit structure attributable to the expedited reduction process. A cylindrical shape cut from monolith, and the calculation achieved aspects of physical and engineering properties such as mass (15 to 20 mg), volume ($V=\pi r^2 h=3.14\cdot(0.5)^2\cdot 0.1\approx 0.0785$ cm³), density (0.191 to 0.254 g^{-1}cm^3), height (0.1 cm), diameter (1 cm), porosity (0.745 to 0.808) available for flow of gas, void volume (0.0585 to 0.0635 cm³), solid volume (0.015 to 0.020 cm³), etc. as summarized in Table 3.1.

3.2.1.1 FT-IR analysis

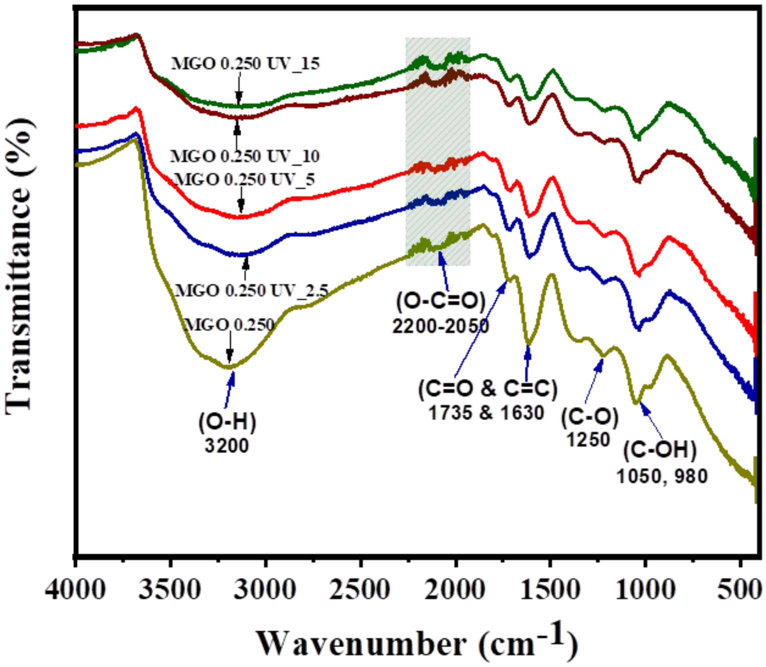

Figure 3.1 FTIR spectra of as-synthesized samples.

FTIR spectra of MGO 0.250 and MGO 0.250 UV_x samples, as illustrated in Figure 3.1. In MGO, different oxygen functionalities on the surface are apparent. The distinctive transmission peaks are directly related to stretching vibrations; the peaks were ascertained at ca. 1735, 2200-2050, 3200, 1250, 1050, and 1630 cm^{-1}, respectively, for the C=O, O–C=O, O–H, epoxide C–O, alcoholic C–O, and un-oxidized aromatic groups [11,131]. These peaks were shown to present at a similar position for the MGO UV_x sample, although the distinctive peak of O–C=O groups was detected to maximize and intensify the MGO 0.250 UV_10 sample while reducing the fashion was shown for the MGO 0.250 UV_15 sample. This demonstrates that UV treatment of 5 h to 10 h time frame may promote additional oxidation by explaining the formation of O–C=O groups on the MGO surface [132]. A fashion was shown in the O–C=O asymmetric stretching mode peak at 2230 cm^{-1}, and it is probable to confirm C–C bond breaking and development of defect [132–135]. Also, the peak at 1250 cm^{-1} of the epoxide C–O group reduces from the start of the UV treatment.

3.2.1.2 EDS analysis

Table 3.3 Elemental composition of MGO 0.250 and MGO 0.250 UV_x adsorbents.

Adsorbent	Atomic % of C	Atomic % of O	C/O ratio
MGO 0.250	65.52	34.48	1.90
MGO 0.250 UV_2.5	65.49	34.51	1.89
MGO 0.250 UV_5	65.38	34.62	1.88
MGO 0.250 UV_10	64.32	35.68	1.80
MGO 0.250 UV_15	65.98	34.02	1.93

Energy dispersive spectroscopy (EDS) of MGO 0.250 and MGO 0.250 UV_x samples was used to evaluate the elemental composition percentage (%) as displayed in Table 3.3 displays the atomic content of oxygen (O) and carbon (C). The surface oxygen functionality is promoted by the MGO 0.250 of the C/O ratio, which was 1.90. The C/O ratios fall after ten-hour UV treatment, which indicates that surface oxygen functionalities have improved. Specifically, for MGO 0.250 UV_10, the C/O ratio of 1.80 was detected. Still, the C/O ratio increased and then decreased surface oxygen functionalities; indeed, the C/O ratio increased by 1.93 during a 15 h UV treatment. The relevant change of the O–C=O functionality discovered in the region of 2200-2050 cm^{-1} was mentioned in the preceding sentence and is well supported by FTIR data, which is a substantial change in the C/O ratio.

3.2.1.3 XRD analysis

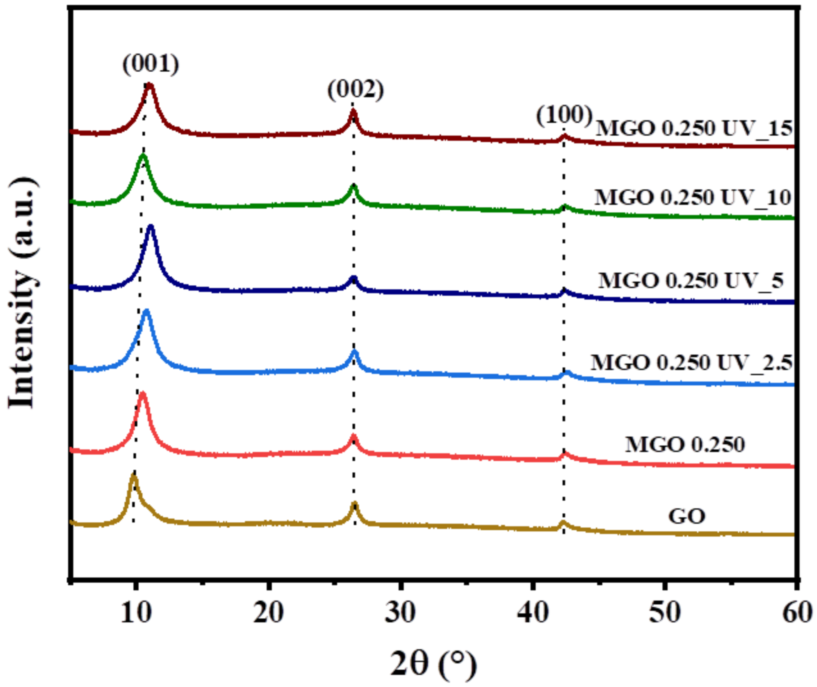

Figure 3.2 XRD patterns of as-synthesized samples.

XRD patterns of GO, MGO 0.250, and activated MGO 0.250 UV_x samples are presented in Figure 3.2. The distinctive crystal diffraction peak at 10.70°, 26.90°, 42.75° which corresponds to (0 0 1), (0 0 2), (1 0 0) of GO, and MGO as revealed in Figure 3.2 [136]. According to Bragg's equation, $n\lambda = 2d\sin\theta$; interlayer spacing for MGO 0.250 for this peak is 8.16 Å [137]. The peak intensity slightly changes for UV activation conditions: up to 5 h, peak intensity slightly decreases; up to 10 h, peak intensity slightly increases; and up to 15 h, peak intensity slightly decreases. This effect is recognized due to the increase and decrease of the oxygen functionalities, as shown in Figure 3.5, which works on MGO interlayer interactions and the crystalline structure of the MGO layers. This fashion was observed with UV-light treatment due to the predominance of surface oxygen functionality, indicating crystalline structural instability. The distinctive crystal diffractions peak presented at 10.44, 10.77, and 10.33° for MGO 0.250 UV_5, MGO 0.250 UV_10, MGO 0.250 UV_15, and the interlayers spacing of 8.83, 9.05, 8.74 Å, respectively. As shown, interlayer spacing increases due to more oxygen functional groups, and an oxidation process occurs [138,139], as mentioned above by FTIR and EDS analysis. In contrast, it partially eliminates the oxygen functional groups through the long UV treatment beyond ten hours.

3.2.1.4 Raman spectral analysis

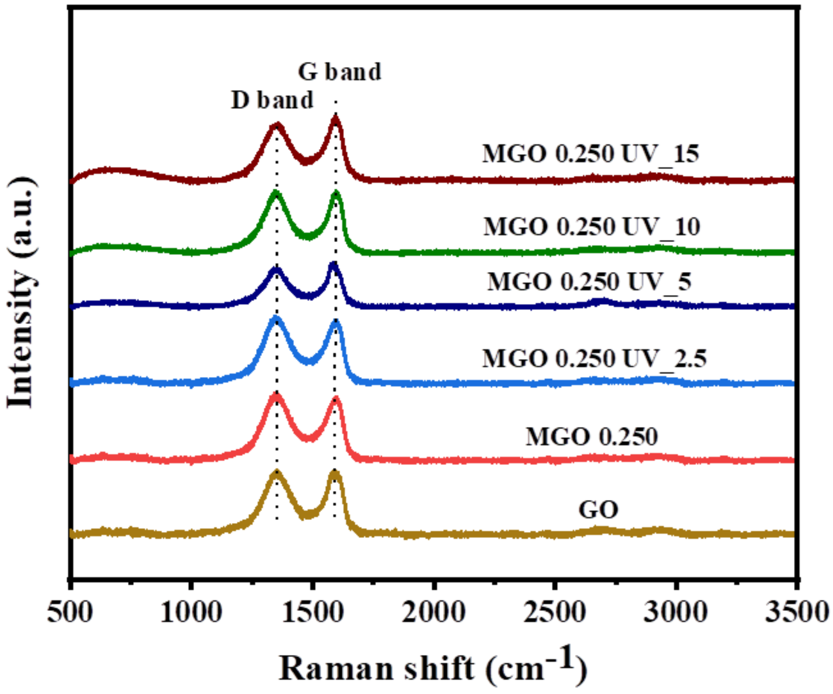

Figure 3.3 Raman spectra of as-synthesized samples.

Raman spectral analysis of GO, MGO 0.250, and MGO 0.250 UV_x samples are shown in Figure 3.3. The peak of adsorbents appeared at 1300 and 1500 cm^{-1} for the D band and G bands, respectively. When sp^3 carbon atoms are present, the D band shows out-of-plane vibrations caused by a structural defect, but the G band shows in-plane vibrations caused by first-order 2g mode scattering when sp^2 carbon atoms are present [131,140,141]. For MGO 0.250, the D band and G band are almost the same intensity; as a result, this shows a small quantity of crystal lattice defects generated from the intense oxidation procedure, which is useful for producing MGO [10]. In the MGO 0.250 UV_x, the intensity of the D band also slightly rises with the treatment of UV light up to 10 h; still, treatment of UV light beyond the ten-hour reduction process was observed. We observed a rise in D band intensity up to 10 h UV light treatment was attributed to the oxidation caused by the UV light treatment, which increased lattice defects and may have caused a decrease in the crystalline size of sp^2 domains [140,142]. Beyond ten-hour UV light treatment, the strength of the D band is related to suppressing the oxygen functional group and possibly partially healing the lattice defect [130,143]. Up to 5 h UV light treatment, G band intensity was almost unaffected; then, for MGO 0.250 UV_10, the intensity was increased. Evidence of the degree of disorder, including contributing elements like flaws, ripples, and edges, can be found in the adsorbents' D and G band intensity ratio, i.e. (I_D/I_G) [144]. The intensity ratio of the D and G band (I_D/I_G) of adsorbents slightly increased up to 10 h UV treatment time with the values of 1.019, 1.021, 1.054, 1.068, 1.071 for GO, MGO 0.250, MGO 0.250 UV_2.5, MGO 0.250 UV_5, MGO 0.250 UV_10, respectively. With a rise in UV light activation beyond ten h, the ratio of I_D/I_G further reduced with the values of 1.012 for MGO 0.250 UV_15, as the values of I_D and I_G are enclosed in Table 3.4.

Table 3.4 Raman spectral analysis data of GO, MGO 0.250, and MGO 0.250 UV_x adsorbents.

Adsorbent	**D – Band**	**G – Band**	**I_D/I_G**
GO	359	352	1.019
MGO 0.250	370	360	1.021
MGO 0.250 UV_2.5	390	370	1.054
MGO 0.250 UV_5	310	290	1.068
MGO 0.250 UV_10	375	350	1.071
MGO 0.250 UV_15	400	395	1.012

3.2.1.5 Surface area and pore volume analysis

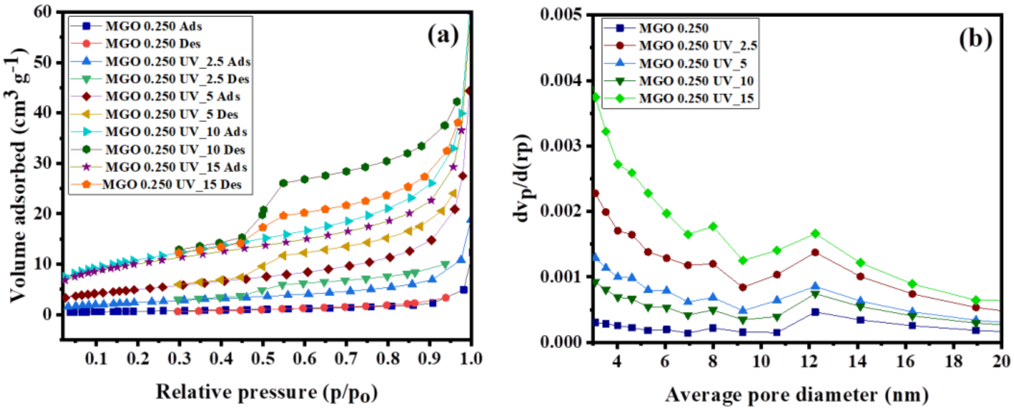

Figure 3.4 (a) N_2 adsorption-desorption isotherm and (b) pore size distribution curves of different adsorbents.

BET analysis of N_2 adsorption-desorption isotherm was performed at 77 Kelvin on an automated gas sorption analyzer (Autosorb-IQ, Quntachrome Instruments). For the adsorption measurements, each adsorbent was degassed at 273 Kelvin for six hours. The specific surface area (external and internal surface area) and porosity (%) were calculated by using nitrogen adsorption uptake and relative pressure (p/p_o). The BET surface area achieved from the N_2 adsorption isotherms at 77 Kelvin; the N_2 adsorption-desorption curve is shown in Figure 3.4(a). The type-IV isotherms agree with the existence of the mesoporous nature of the adsorbent, and the average pore diameter lies in the range of 5.0 nm to 20.0 nm. This observation analyzed the specific surface area (SSA) increases with UV treatment, as shown in Table 3.5. The calculated BET surface areas and total pore volumes of the as-prepared MGO 0.250_x were much more significant than those of MGOs. The MGO 0.250 UV_10 exhibits the most significant BET surface area (577.3 m^2 g^{-1}) and total pore volume (1.59 cm^3 g^{-1}), which most likely results from the development of more porosity, despite having particular surface areas of our created MGO 0.250 UV_x that are significantly less than the 2630 m^2 g^{-1} predicted surface area of a single graphene sheet [145]. However, they still match or exceed those of graphene aerogel (512 m^2 g^{-1}) [146], graphene sponge (418 m^2 g^{-1}) [147], and graphene nanoplates (480 m^2 g^{-1}) [148]. The Barrett-Joyner-Halenda (BJH) method's pore size distributions (PSDs) showed that holes with a diameter of less than 20 nm provided the majority of the pore volume, as shown in Figure 3.4(b), with a more apparent PSD in the 4 to 16 nm range, suggesting that all MGOs has small mesopores in the basal plane as shown in Table 3.5. The MGOs precursor volume was raised, and the SSA and total pore volume significantly increased, resulting in a more compacted structure for MGO 0.250 UV_10. However, the PSD shift maximum from 3.65 nm for MGO 0.250 UV_5 to 3.80 nm for MGO 0.250 UV_10 shows increased oxygen functionality levels, producing MGOs with larger holes. This result is likewise compatible with alterations in the I_D/I_G ratio of the adsorbents, and the MGO 0.250 can conveniently be used to change the samples' concurrent porosity with UV treatment (2.5 h to 15 h).

Table 3.5 BET data of MGOs and MGO 0.250 UV_x adsorbents.

Adsorbent	**SSA (m^2 g^{-1})**	**Total pore volume (cm^3 g^{-1})**	**Pore volume (cm^3 g^{-1})**	**Average pore diameter (nm)**	**Porosity (%)**
MGO 1.000	289.2	0.69	0.4	5 to 20	57.97
MGO 0.500	297.7	0.75	0.46	5 to 20	61.33
MGO 0.250	311.1	0.88	0.65	5 to 20	73.86
MGO 0.250 UV_2.5	429.5	1.25	0.98	5 to 20	78.40
MGO 0.250 UV_5.0	520.9	1.37	1.20	5 to 20	87.59
MGO 0.250 UV_10	577.3	1.59	1.42	5 to 20	89.30
MGO 0.250 UV_15	396.0	1.10	0.84	5 to 20	76.36

3.2.1.6 SEM analysis

After treatment with UV light, SEM image characterization was performed to obtain evidence about the monolith's structure, surface morphology, and porosity. The surface morphology of GO, MGO 0.250, and MGO 0.250 UV_x was observed by using the SEM image, as shown in Figure 3.5. The porous morphology is subjected to studies by the low amount of OxA having larger pores. Significantly, the surface roughness of MGO 0.250 seemed to improve with a UV-treatment time of 2.5 h to 15 h, and it is recognized to have morphological disorders such as the introduction of the ripple, wrinkles, thin sheets, and related structures in these monoliths as revealed in Figure 3.6. Indeed, these images emphasized SEM image observations that were associated with an increase in surface roughness after UV light treatment.

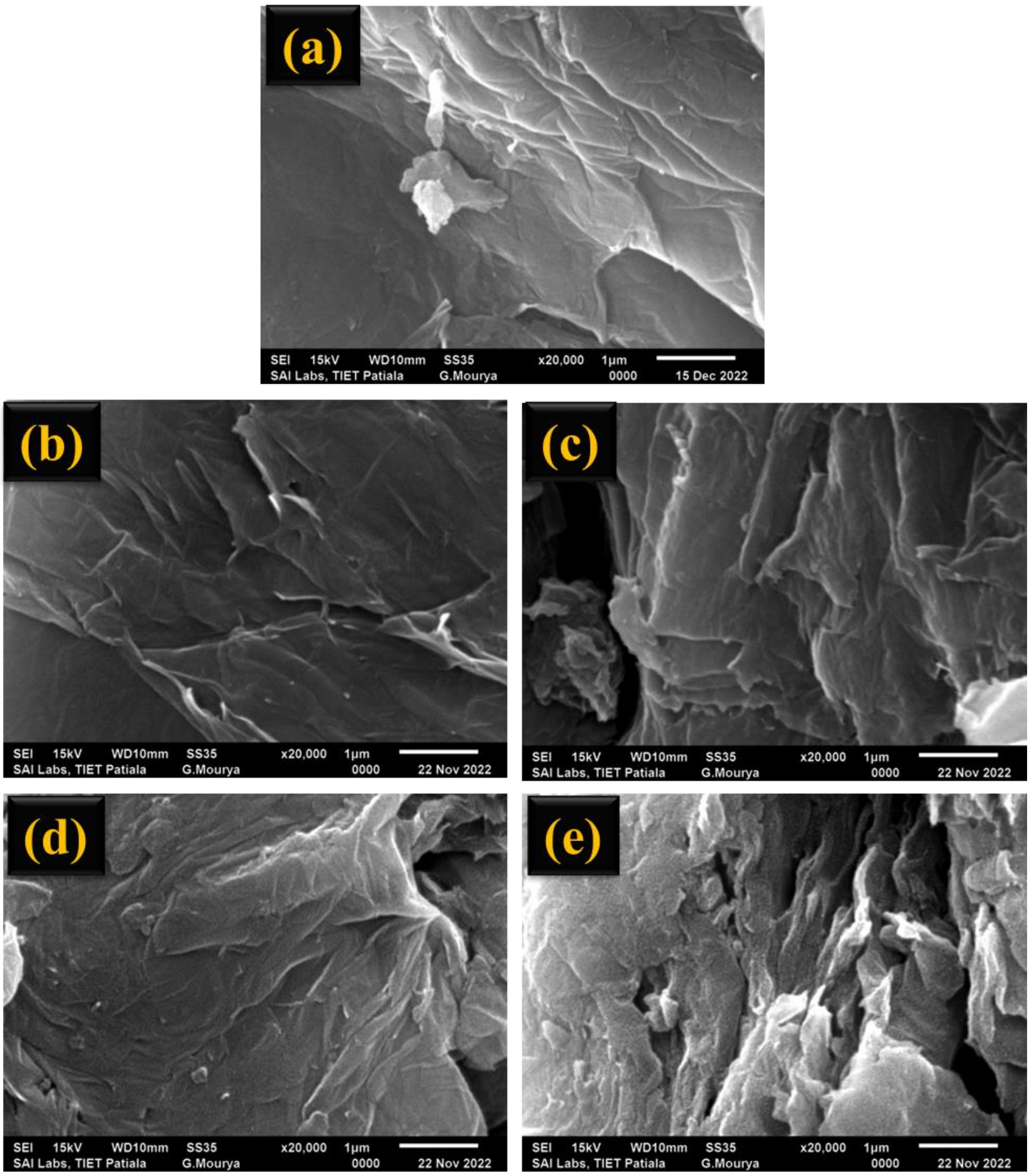

Figure 3.5 SEM images of (a) GO, (b) MGO 0.250, (c) MGO 0.250 UV_5, (d) MGO 0.250 UV_10, and (e) MGO 0.250 UV_15 adsorbents.

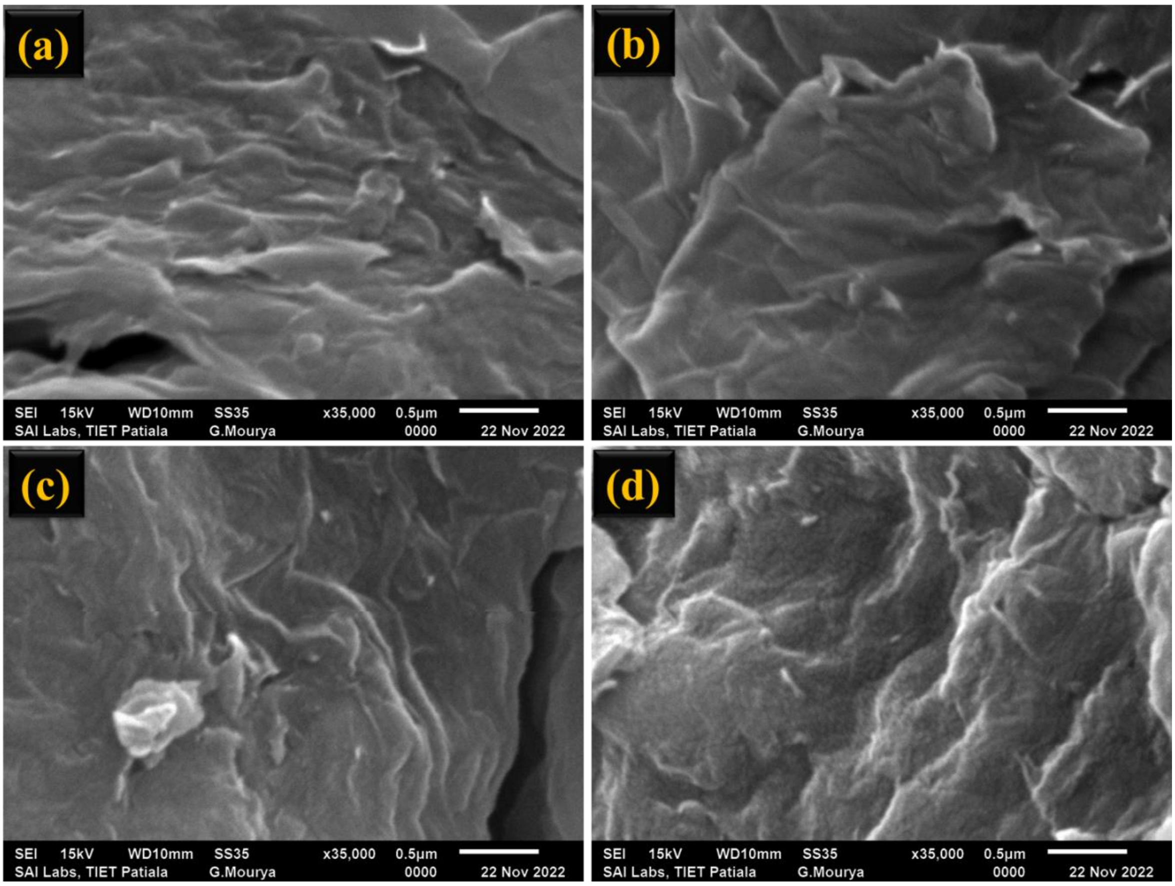

Figure 3.6 SEM images of (a) MGO 0.250, (b) MGO 0.250 UV_5, (c) MGO 0.250 UV_10, and (d) MGO 0.250 UV_15 adsorbents.

3.2.2 The CO_2 capture mechanism of monolithic materials

The CO_2 capture mechanism depends on the physiochemical properties of the adsorbent. The shape and size of the pores have been significant, and there should be enough pores for effective interactions during the CO_2 capture process. Additionally, the adsorbent needs to have an abundance of pores with a large surface area to achieve excellent CO_2 adsorption. The correlation between porosity and CO_2 adsorption can be seen in the impact of porosity on CO_2 adsorption performance. Figure 3.7(a) shows that the mesopores percentage increases with CO_2 capture performance increases. The increase in CO_2 capacity is mainly due to the rise in the mesopores percentage in the range of 57.97 to 76.36 %. To calculate the exact range of mesopores percentage for CO_2 adsorption and the correlation between the CO_2 capacity on the MGOs and MGO 0.250 UV_x samples as displayed in Table 3.5 and Figure

3.7(b, c) and their cumulative pore volume in specific ranges (d < 1 nm and d > 1 nm). Figure 3.7(b, c) revealed that the best linear relationship ($R^2 = 0.99$) is observed in the range of d < 1 nm, where the R^2 value is higher than that of the d > 1 nm range. The MGO 0.250 UV_10 adsorbent's CO_2 adsorption capacity was enhanced by pores with a d < 1 nm range.

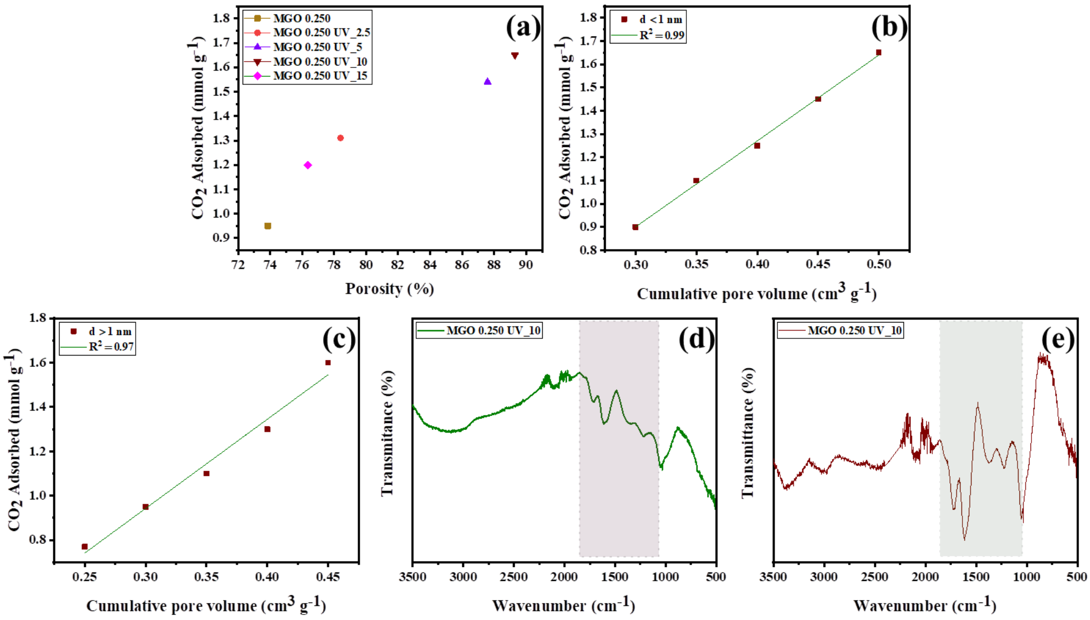

Figure 3.7 (a) Relation between CO_2 adsorption capacity with mesopore % of MGO 0.250 and MGO 0.250 UV_x adsorbents, and linear relation between CO_2 adsorption capacity with cumulative pore volume (b) d < 1 nm, (c) d >1 nm, (d) FT-IR spectra before CO_2 adsorption for MGO 0.250 UV_10 adsorbent and (e) FT-IR spectra after CO_2 adsorption for MGO 0.250 UV_10 adsorbent.

To gain insights into the adsorption mechanism, we conducted FT-IR spectroscopy analysis on MGO 0.250 UV_10 while adsorbing CO_2 under conditions of 25 °C and 50% CO_2 concentration flow. The FT-IR spectra, as depicted in Figure 3.7(e), allowed us to identify specific adsorption peaks. Notably, significant differences were observed between the two spectra (carbamate and bicarbonate) in the 1800-1050 cm^{-1} range and isolated the spectra by subtracting the spectrum of pure carbon before CO_2 adsorption as presented in Figure 3.7(d, e). This analysis revealed that the peak corresponding to COO^- indicated the development of carbamate, while the presence of HCO_3^- suggested the formation of bicarbonate. These findings support the understanding that 2D porous graphene can effectively self-assemble into a 3D hierarchical porous graphene structure [105,149,150].

3.3 CO_2 adsorption performance

3.3.1 CO_2 adsorption performance of monolithic materials

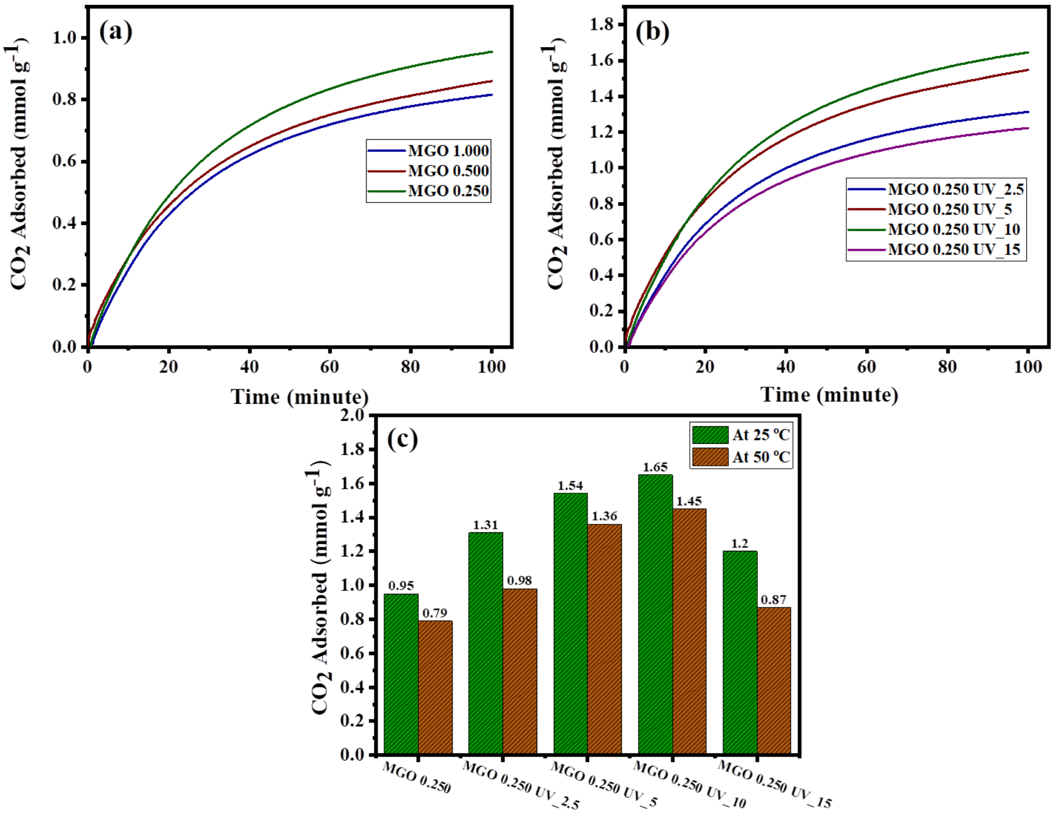

Figure 3.8 CO_2 adsorption performance at 25 °C for (a) MGOs, (b) MGO 0.250 UV_x adsorbents, and (c) CO_2 adsorption performance at 25 °C and 50 °C by a bar graph.

The CO_2 adsorption capacity of synthesized MGOs and MGO 0.250_x adsorbents was performed as shown in Figure 3.8(a, b) and graphically in Figure 3.8(c). The exact values are also enclosed in Table 3.6. The CO_2 adsorption capacity surges to its highest for MGO 0.250 UV_10 adsorbent. The former possessed narrow slit pores, resulting in an approximate CO_2 adsorption capacity of ca. 1.65 mmol g^{-1}, around two times more than the latter's ca. 0.81 mmol g^{-1}. As evidence, in the primary stage, the CO_2 adsorption capacity decreases for one hour of UV treatment, CO_2 adsorption capacity surges to its highest at ten hours of UV treatment, and CO_2 adsorption capacity decreases for extended UV treatment beyond ten hours duration. The above trend followed and agrees with specific surface area, pore volume, and porosity (%) as mentioned in Table 3.5; FTIR spectral data also showed that oxygen functional groups improved after 10 hours of UV treatment before being suppressed, EDS shows the least of carbon and oxygen ratio for ten hours UV treatment increased. As the UV treatment progressed, FTIR measurements at 1250 cm^{-1} showed a decrease in the peak intensity of the epoxide C–O group. As a result of this comment, we have observed a fall in CO_2 adsorption capacity for one hour of UV treatment. The adsorption capacity of MGO 0.250 was decreased beyond ten hours of UV treatment durations, perhaps the effect of suppression and de-oxygenation of the functional groups. Subsequently, the best UV treatment period was found, which increased MGO 0.250 adsorption capacity up to 90 % by UV treatment for ten hours. The CO_2 adsorption at equilibrium time implies the adsorption capacity, which can be calculated by employing Equation 2.1. Consistent with pressure up to 1 bar and low adsorption temperature (25 °C), the adsorption capabilities increase. The equilibrium CO_2 absorption increased in the following order: MGO 1.000 (0.81 mmol g^{-1}) < MGO 0.500 (0.86 mmol g^{-1}) < MGO 0.250 (0.95 mmol g^{-1}) < MGO 0.250 UV_15 (1.20 mmol g^{-1}) < MGO 0.250 UV_2.5 (1.31 mmol g^{-1}) < MGO 0.250 UV_5 (1.54 mmol g^{-1}) < MGO 0.250 UV_10 (1.65 mmol g^{-1}). The reason is that MGO 0.250 UV_10 had the smallest mesopore size of any of the samples, the highest SSA, and the best CO_2 capture performance. The literature also explains how smaller pores contribute to low-pressure CO_2 adsorption [151].

Table 3.6 CO_2 adsorption capacity of MGO and MGO 0.250 UV_x adsorbents at 25 °C and 50 °C.

Adsorbents	**Ads. Time (min)**	**Adsorption Temperature (^oC)**	**CO_2 conc. (%)**	**Adsorption capacity (mmol g^{-1})**
MGO 1.000	100	25	50	0.81
MGO 0.500	100	25	50	0.86
MGO 0.250	100	25	50	0.95
MGO 0.250 UV_1	100	25	50	0.78
MGO 0.250 UV_2	100	25	50	1.19
MGO 0.250 UV_2.5	100	25	50	1.31
MGO 0.250 UV_5	100	25	50	1.54
MGO 0.250 UV_10	100	25	50	1.65
MGO 0.250 UV_15	100	25	50	1.20
MGO 0.250	100	50	50	0.79
MGO 0.250 UV_5	100	50	50	1.36
MGO 0.250 UV_10	100	50	50	1.45
MGO 0.250 UV_10	100	25	40	1.46
MGO 0.250 UV_10	100	25	20	1.20

Furthermore, as shown in Table 3.7, the CO_2 adsorption in MGO 0.250 UV_10 is superior to or equivalent to that in other graphene-based materials under the condition of CO_2 concentration flows at 50 % and temperature at 25 °C. The amounts of CO_2 adsorbed on MGO 0.250 UV_10 dropped from ca.1.65 mmol g^{-1} to ca.1.45 mmol g^{-1} at the pressure of 1 bar when the adsorption temperature was raised from 25 °C to 50 °C. However, this capacity for CO_2 adsorption is greater than the ca. 1.71 mmol g^{-1} at 30 °C obtained for 3D graphene [152], 1.51 mmol g^{-1} at 27 °C obtained for carbon nanotubes (CNTs) [153], 1.40 mmol g^{-1} at 25 °C measured for HGF-II [59], 0.55 mmol g^{-1} at 25 °C measured for activated carbons [154]. A further decrease in CO_2 uptake at 50 °C is anticipated to result from endothermic adsorption. However, the adsorbed levels of CO_2 are still ca.1.45 mmol g^{-1} at 1 bar, as shown in Table 3.6.

Table 3.7 Comparison table of CO_2 adsorption performance of MGO 0.250 UV_10 with other reported adsorbents.

Adsorbent	**Activation method**	**Experimental conditions**		**CO_2 Adsorbed (mmol g-1)**	**Ref.**
		CO_2 conc. (%)	**Temp. (°C)**		
MGO 0.250 UV_10*	UV treatment for 10 h	50	25	1.65	Present study
MGO 0.250 UV_10*	UV treatment for 10 h	50	50	1.45	Present study
Potassium based AC	Chemical/K_2CO_3 (25 °C)	0.5	20	0.87	[155]
Carbon monolith	Chemical/KOH (25 °C)	15	30	0.66	[156]
HGF-II	Chemical/HNO_3 (500 °C)	100	25	1.40	[59]
CNTs	Chemical/$SOCl_2$/NH_4OH (350 °C)	60	27	1.58	[153]
EDA	Chemical/COOH (85 °C)	100	25	2.00	[157]
M90_0.5	Chemical/$C_6H_8O_6$ (90°C)	100	25	2.10	[13]
10UV-GOF	UV treatment for 10 h	100	25	1.85	[24]

Additionally, it has been observed that different researchers are using various activation techniques to modify the adsorbents for the purpose of CO_2 adsorption. UV treatment is one of the most excellent activation methods for improving the porosity characteristics and adsorption capacity of the adsorbents. When the results are compared to those of other studies, it is observed that the activated adsorbents developed in the current study exhibit greater adsorption capabilities. This result supports the idea that MGO 0.250 UV_10 would be useful for CO_2 capture. The technology facilitated the comprehensive regeneration of a substantial amount of adsorbed CO_2 from emissions of coal-fired power plants, making it available for future utilization or sequestration.

3.3.2 Regeneration study

A regeneration study of the activated adsorbents was done at various temperatures (50 °C, 75 °C, and 100 °C), as shown in Figure 3.9. UV treatment enhanced CO_2 recovery (%) of the activated adsorbents, and it was verified at different temperatures, as shown in Table 3.8. The recovery rates of 88.40 % and 98.80 % were observed for MGO 0.250 and MGO 0.250 UV_10, respectively, at 100 °C. The proportion of CO_2 recovery % was instantly enhanced by raising the regeneration temperature. As a result, the MGO 0.250 UV_10 adsorbents were almost entirely reversible at 100 °C, with 98.80 % recoveries occurring, as illustrated in Table 3.8. The regeneration study of MGO 0.250 and MGO 0.250 UV_10 adsorbents are assigned to the modification of reaction potential vary with CO_2 graphitic surface [19]. As shown by the XRD data discussed above, an increase in the interlayer dissociation upon MGO 0.250 UV_10 adsorbent is expected to enhance desorption by stopping CO_2 captured within MGO interlayer galleries upon the report from active sites.

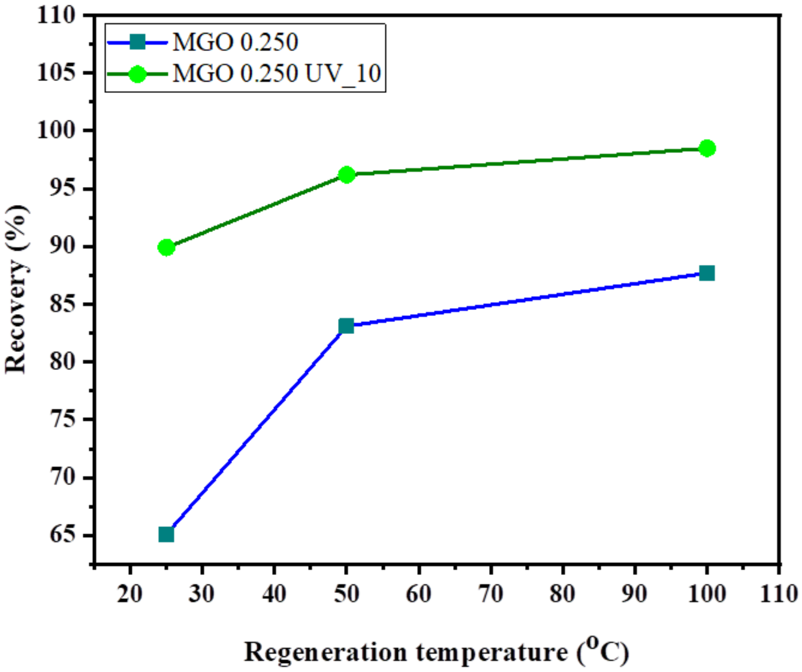

Figure 3.9 Regeneration study of MGO 0.250 and MGO 0.250 UV_10 adsorbents.

Table 3.8 Adsorption-desorption cycle of MGO 0.250 and MGO 0.250 UV_10 adsorbents.

Adsorbent	CO_2 Adsorbed (mmol g^{-1}) at 25 °C	CO_2 Desorbed (mmol g^{-1})				Recovery % of Adsorbed CO_2			
		25 °C	50 °C	75 °C	100 °C	25 °C	50 °C	75 °C	100 °C
MGO 0.250	0.95	0.60	0.79	0.83	0.84	63.1	83.1	87.3	88.4
MGO 0.250 UV_10	1.65	1.48	1.56	1.60	1.63	89.7	94.5	96.9	98.8

3.3.3 Selectivity

The selectivity experiments for CO_2/N_2 were conducted at 25°C using the prepared adsorbents, and the influence of UV activation on the adsorbent was investigated. Figure 3.10 presents the results obtained for the UV-activated adsorbents (MGO 0.250 UV_10), indicating a significant decrease in N_2 adsorption capacity after UV activation. However, there was an increase in CO_2 uptake, resulting in an enhanced CO_2/N_2 selectivity of the UV-activated samples (MGO 0.250 UV_10) by approximately three times compared to the MGO 0.250 adsorbent at 1 bar. These results are linked to Table 3.9, where selectivity values of 22.00, 23.57, and 20.00 were achieved at 1 bar for MGO 0.250 UV_5, MGO 0.250 UV_10, and MGO 0.250 UV_15, respectively, showing significant improvement compared to the MGO 0.250 with a selectivity value of 9.50. Considering the presence of various industrial emission sources, the use of these adsorbents for CO_2 capture at 1 bar pressure conditions holds significant technological importance. The studies concluded that the MGO 0.250 UV_10 adsorbent proved to be an excellent alternative for efficient CO_2 recovery from flue gases [24,51,59,114].

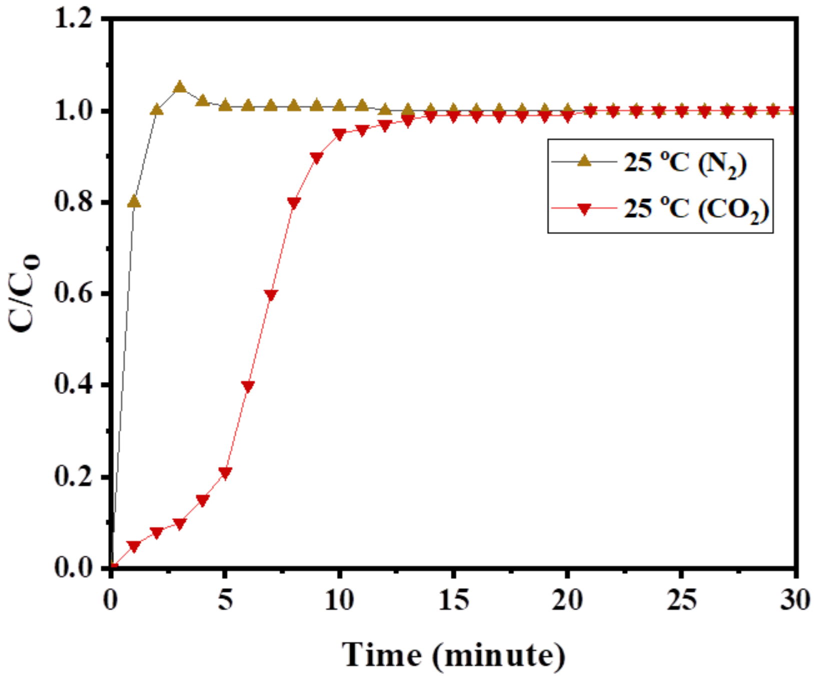

Figure 3.10 CO_2/N_2 selectivity curve.

Table 3.9 CO_2/N_2 adsorption selectivity on MGO 0.250, MGO 0.250 UV_5, MGO 0.250 UV_10, and MGO 0.250 UV_15 adsorbents at 25 °C.

Adsorbent	**CO_2 Adsorbed (mmol g^{-1})**	**N_2 Adsorbed (mmol g^{-1})**	**CO_2/N_2 Selectivity**
	1 bar	**1 bar**	**1 bar**
MGO 0.250	0.95	0.10	9.50
MGO 0.250 UV_5	1.54	0.07	22.00
MGO 0.250_2 UV_10	1.65	0.07	23.57
MGO 0.250 UV_15	1.20	0.06	20.00

3.3.4 Breakthrough curves

The breakthrough curves for the MGO 0.250, MGO 0.250 UV_5, MGO 0.250 UV_10, and MGO 0.250 UV_15 samples are revealed in Figure 3.11, which assess the dynamic CO_2 adsorption capacity of ca. 1.0 mmol g^{-1} at 25 °C, 1 bar pressure and CO_2/N_2 binary gas mixture with 50% CO_2 concentration flows. It was noted that N_2 was instantly identified, whereas CO_2 began to emerge in the effluent after some time. This shows that N_2 has a lower adsorption capability than CO_2. Initial values of C/C_o for $N_2 > 1$ indicate that N_2

initially occupies the adsorbent's active sites, but with time, N_2 is gradually replaced by CO_2 [51,114].

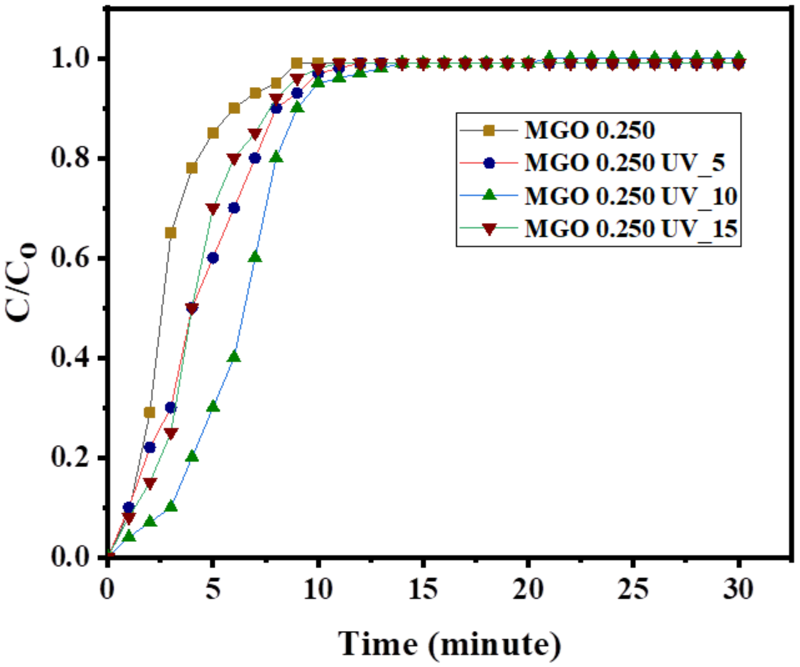

Figure 3.11 Breakthrough curves for CO_2 adsorption of MGO 0.250 and MGO 0.250 UV_x adsorbents.

3.3.5 Adsorption-desorption isotherms

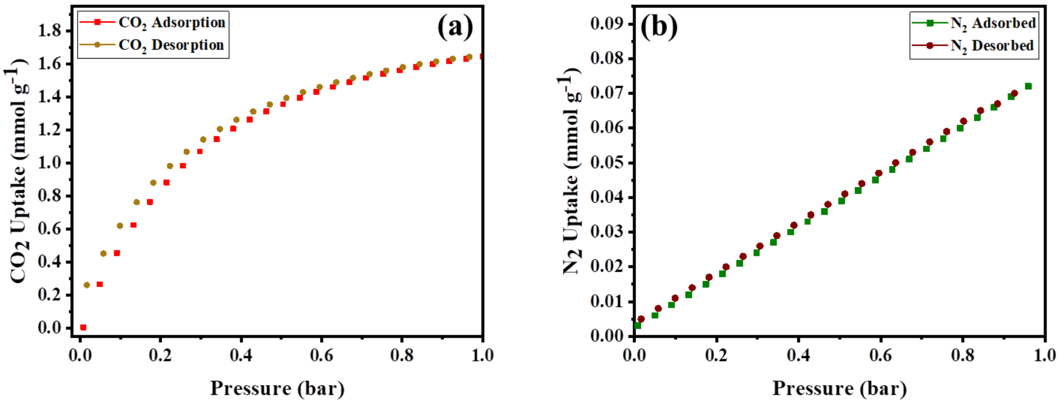

Figure 3.12 Adsorption-desorption curve of (a) pure CO_2 and (b) pure N_2 by MGO 0.250 UV_10 adsorbent.

Adsorption-desorption isotherms show pure component of MGO 0.250 UV_10 at 25 °C, the concentration of pure CO_2 flow (50 %), and at 1 bar pressure (P_o= P_{CO2}+P_{N2}=1bar). The volumetric adsorption capacity of CO_2 on MGO 0.250 UV_10 is shown in Figure 3.12(a). The adsorption capacity was observed to rise as the pressure increased, and the adsorption capacity went on to 1.65 mmol g^{-1} at 1 bar. According to Figure 3.12(b), MGO 0.250 UV_10 has an extremely low N_2 adsorption capability of 0.07 mmol g^{-1} at 25 °C. The MGO 0.250 UV_10 adsorbent, in addition, offers a better selectivity for CO_2. Additionally, the adsorption-desorption isotherms for CO_2 and N_2 exhibit hysteresis adsorption, which implies that just a small amount of energy is required to reuse the adsorbent. From this comprehensive finding, we have compared various published research articles that exhibited CO_2 uptake [24,59,153,158].

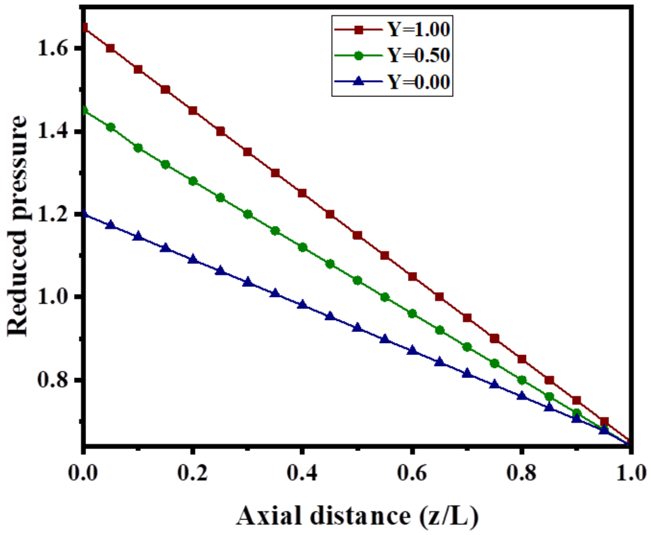

Figure 3.13 Axial pressure profile of MGO 0.250 UV_10 adsorbent for various feed combinations during adsorption at 25 °C and constant volume flow rate.

It is noteworthy that, as shown in Figure 3.13, feed combination significantly impacts the final axial pressure profile. The pressure drops are inversely proportional to the feed's mole fraction of the absorbed gas (CO_2). When using a pure N_2 and CO_2 feed, the pressure drops ca. 50 % and ca. 49.9 % of the original pressure, respectively. This evolution tendency, though, might be going the other way. This depends on the physical characteristics of the gas mixture's ingredients. If these characteristics are held constant throughout the whole process, this could cause simulation results to be inaccurate, especially for steps that are followed by noticeable shifts in gas setup, temperature, and pressure. It should be noted that Ergun's law, which only considers viscosity and ignores density, was employed to calculate momentum for feeds of pure N_2, pressure drop is ca. 50 % of the starting pressure ($\mu = 1.00 \times 10^{-3}$ kg mol^{-1} at 25 °C and 1 bar) and feeds of pure CO_2, pressure drop is ca. 49.9 % of the starting pressure ($\mu = 0.99 \times 10^{-3}$ kg mol^{-1} at 25 °C and 1 bar), respectively. For a pure CO_2 flow, pressure drop values were calculated using the Ergun momentum equations. Consider the situation where the molar flow rate remains constant. When pressure drop is ignored, this flow rate's value equals that of the resulting value (In this instance, both velocity and pressure are consistent throughout the entire process). In the absence of a pressure drop, applying either a volume flow rate or a molar flow rate produces the same simulation outcomes. Because of this, one can use any boundary conditions to perform an adsorption step without a pressure drop. From this comprehensive finding, we have compared published research articles that exhibited pressure drops of various feed compositions of CO_2 uptake at 25 °C [159–162]; the pressure drop was almost similar in this reported literature. Although the dynamic capacity is more critical for CO_2 capture from specific applications in flue gas,

3.3.6 Multiple adsorption-desorption cycles

The multiple adsorption-desorption cycles of the MGO 0.250 UV_10 adsorbent were performed, as shown in Figure 3.14. In the adsorption-desorption cycles, the sample MGO 0.250 UV_10 displays a stable adsorption performance of ca. 1.65 mmol g^{-1} with no loss in efficiency. After adsorption, ca. 1.348 MJ of heat energy per kg of CO_2 is needed for CO_2 to be desorbed. The sample's CO_2 uptake remained steady after several cycles (MGO 0.250 UV_10), indicating its excellent cyclic stability and regenerability. These findings emphasize the advantage of the UV treatment of MGOs for shifting adsorbed CO_2, as shown in Table 3.8.

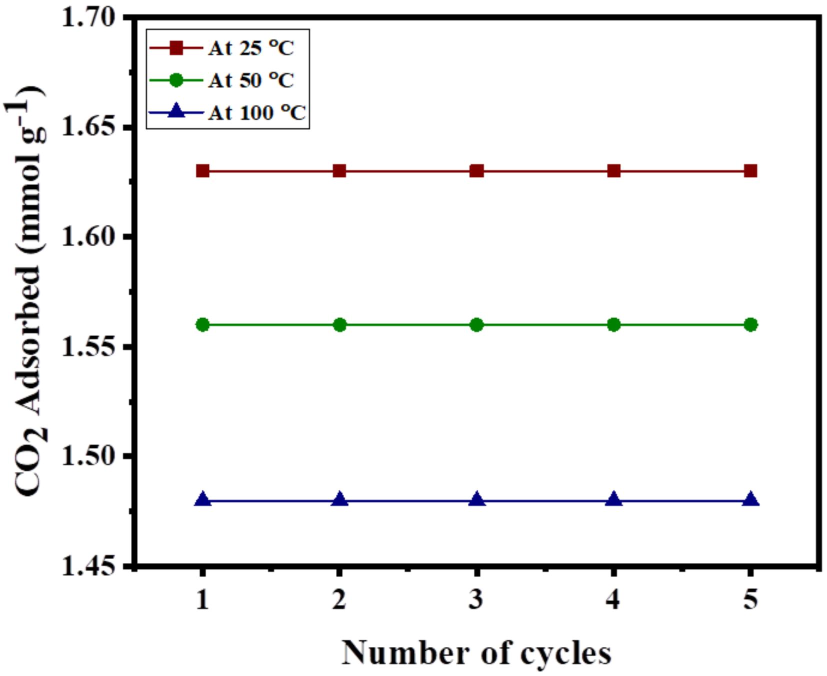

Figure 3.14 Multiple CO_2 uptake cycles of MGO 0.250 UV_10 adsorbent at 25 °C, 50 °C, and 100 °C.

3.4 Adsorption kinetic study

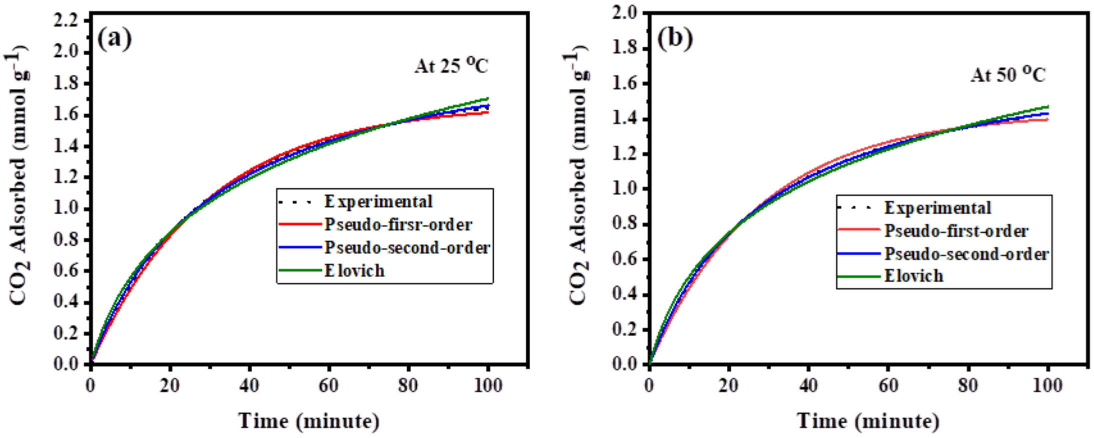

Figure 3.15 Kinetic models fit: (a) at 25 °C and (b) at 50 °C by CO_2 adsorption data of MGO 0.250 UV_10 adsorbent.

The MGO 0.250 UV_10 exhibits faster adsorption kinetics for CO_2 adsorption under the experimental conditions at 1 bar, temperatures (25 $^{\circ}$C and 50 $^{\circ}$C), and the concentrations of CO_2 flow 50 %. We have investigated the effect of temperature at 25 °C and 50 °C in both cases, showing faster kinetics. Notably, at 25 °C, adsorbents exhibit slightly slower kinetics than at 50 °C. At 25 °C, surface coverage increases compared to at 50 °C. At 50 °C, the adsorbent exhibits faster kinetics, emphasizing the chemisorption's enhanced effect. As can be seen in Figure 3.15(a, b), high adsorption rates were used for CO_2 uptake, reaching the highest possible rate of CO_2 absorption, which result is more compatible compared to many earlier experiments [59,114,163–165]. Owing to the sample's increased oxygen functional group reactivity, the potential for rapid adsorption was attributed to diffusional restrictions [166]. As a result, physisorption type of fitting, e.g., by van der Waals interaction [167]. These findings unequivocally show that MGO 0.250 UV_10 can disperse CO_2 from flue gases while functioning with incredibly fast adsorption/desorption cycle durations, which would be advantageous economically for commercial deployment. Therefore, the adsorption kinetic studies for the adsorption process provide the ability of the efficiency of the adsorbent to the higher adsorbate and give the data for calculating the adsorption rate [118], the equation as explained in Equation 2.5, 2.7, and 2.8. In this experimental study, we have examined the MGO 0.250 UV_10 adsorbents using different kinetic models, as illustrated in Figure 3.15(a, b), and the kinetic fitting of experimental CO_2 adsorption data by different kinetic models. The kinetic studies for the CO_2 adsorption process followed the pseudo-second-order kinetic model, with higher R^2 values and low error percentages (%). Similarly, it illustrates the kinetic fitting models based on CO_2 adsorption experiment data using MGO 0.250 UV_10 adsorbent. The calculated values that match to the CO_2 capture experimental data regarding time were found using the pseudo-first-order, pseudo-second-order, and Elovich kinetic models. From this observation, we have observed that the pseudo-second-order kinetic model best fitted the range of CO_2 adsorption with a higher R^2 value and lower error percentage (%), as illustrated in Table 3.10.

Table 3.10 Kinetic models and parameters of MGO 0.250 UV_10 adsorbent.

Kinetic models	**Parameters**	**Sample (MGO 0.250 UV_10)**	
		25 ^oC	**50 ^oC**
Pseudo-first-order	q_e	1.6312	1.4426
	k_1	0.0351	0.0347
	R^2	0.9858	0.9882
	Error (%)	3.5922	2.9586
Pseudo-second-order	q_e	1.6952	1.4835
	k_2	0.0184	0.0143
	R^2	0.9912	0.9932
	Error (%)	2.7418	2.3103
Elovich	β (q_e)	1.5820	1.3728
	α (k_n)	0.0908	0.0860
	R^2	0.9827	0.9816
	Error (%)	4.1188	4.3241

3.5 Adsorption isotherm study

An adsorption isotherm study was carried out to calculate the adsorption mechanism and play the role of adsorbent and adsorbate in the CO_2 adsorption process. In this study, we have considered the effect of temperature at 25 °C and 50 °C, as shown in Figure 3.16(a, b). The three standard isotherm models from experimental CO_2 adsorption data fitted to models like Langmuir, Freundlich, and Temkin, the equation as explained in Equations 2.10, 2.11, and 2.12. At 25 °C, the K_F values, i.e., $n < 1$, recommend the most favorable adsorption of CO_2 at low temperatures than at 50 °C [168]. The experimental and calculated values of R^2 are summarized as shown in Table 3.11 in different isotherm models, with higher R^2 values verifying the best-fitted experimental data. Adsorption strength is measured by the isosteric differential heat of adsorption (Q_{st}), which depends on the heterogeneity of the adsorption site, interactions between gas and solids at the surface, their nature, as well as the dynamics change with surface coverage [169]. The Clausius-Clapeyron equation was applied to the CO_2 isotherms as depicted in Figure 3.16(a, b) to determine the Q_{st}. We observed that the Freundlich isotherm model shows a heterogeneous substance on the adsorbent surface. The K_F values, i.e., $n < 1$, recommend the most favorable adsorption of CO_2 at low temperatures [168].

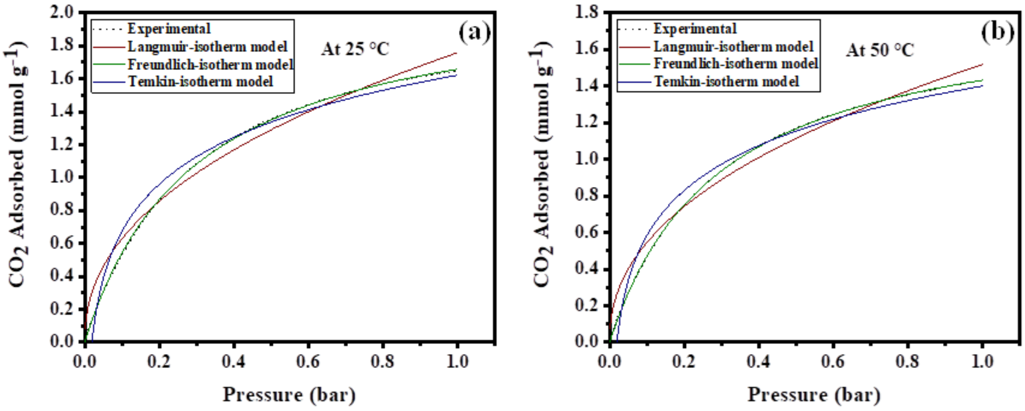

Figure 3.16 Isotherm models fit: (a) at 25 °C and (b) at 50 °C by adsorption data of MGO 0.250 UV_10 adsorbent.

Table 3.11 Isotherm model and its parameters for CO_2 adsorption by MGO 0.250 UV_10 adsorbent.

Isotherm model	**Parameters**	**Temperature**	
		25 °C	**50 °C**
Langmuir	q_m (mmol g^{-1})	1.7586	1.5178
	K_L (atm^{-1})	0.4464	0.4445
	R^2	0.9720	0.9735
Freundlich	K_F (atm^{-1})	0.3824	0.3754
	N	0.4516	0.4453
	R^2	0.9996	0.9998
Temkin	K_T (atm^{-1})	0.4121	0.4110
	B (KJ mol^{-1})	21.6538	21.6425
	R^2	0.9518	0.9521

3.6 Thermodynamic study

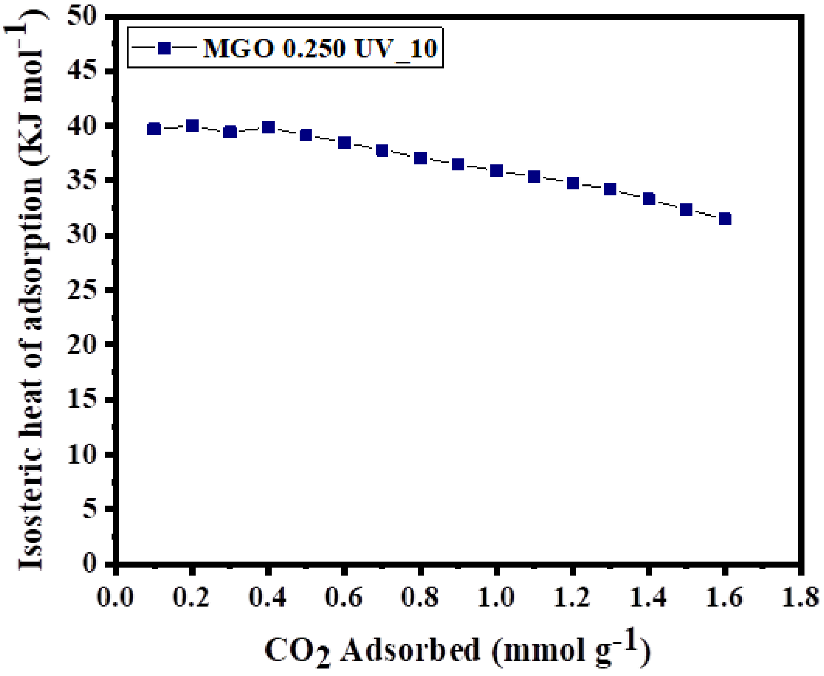

Figure 3.17 Plot of Q_{st} against surface loading (q_e) for CO_2 adsorption on MGO 0.250 UV_10 adsorbent.

The CO_2 adsorption for thermodynamic parameters plays a vital role informed by the CO_2 interaction of adsorption sites with the adsorbent surface. The Gibbs free energy (ΔG°) adsorbed CO_2 in KJ mol^{-1} was estimated using Equation 3.1. The Van't Hoff plot [170] can be used to calculate the standard entropy change (ΔS°) in JK^{-1} mol^{-1} and the standard enthalpy change (ΔH°) in kJ mol^{-1} by Equation 2.14. The Q_s in kJ mol^{-1} represented in Equation 2.15 were calculated by Clausius-Clapeyron equation [171]. Calculated values of thermodynamic factors are shown in Table 3.13. The MGO 0.250 UV_10 adsorbent exhibits a higher heat of adsorption, which implies an enhanced interaction of CO_2 on the surface of MGO 0.250 UV_10 adsorbent, validating the idea that the impact of chemisorption is increased after UV treatment. Instead, the heat of adsorption appears to decrease as surface coverage improves in the UV-treated adsorbents, as shown in Figure 3.17. This behavior is evidence of the highly heterogeneous surface adsorption sites that are accessible [172].

The value of ΔH° was positive (+13.1154139 kJ mol^{-1}), showing the adsorption process is endothermic. Furthermore, the negative values of ΔG° signify that the adsorption process is spontaneous and feasible [168]. The value of ΔS° was positive (+3.63705207 kJ mol^{-1}), which shows the greater affinity of adsorbents and proposes the surge in the randomness/disorder at the surface of solid/gas applying the Clausius-Clayperon equation as expressed in Equation 3.2. The calculating isosteric heat (Q_{st}) values for MGO 0.250 UV_10 at various q_e starting from 31.50 kJ mol^{-1} to 39.70 kJ mol^{-1} as shown in Table 3.12, and exhibited a significant Q_{st}. In contrast, the activated adsorbent exhibited a significant increase in the isosteric heat, particularly with increasing CO_2 loadings, extending an extreme of approximately 36.59 KJ mol^{-1}, which indicates the proximity to saturation. The Fowler-Guggenheim model's explanation for the interaction energy between adsorbed CO_2 molecules [173] attributes this behavior to strong lateral contacts among the CO_2 molecules. The presence of intermolecular forces resulting from quadrupole-to-quadrupole interactions between the adsorbed CO_2 quadrupoles on the faulty graphene surface [174] further supports this phenomenon. Consequently, the Q_{st} values displayed a more pronounced trend at higher surface loadings than lower surface loadings, owing to the greater abundance of CO_2 molecules. The randomness/disorders varied; the Q_{st} values were recorded at different temperatures. Surface coverage increased, satisfying the heterogeneous behavior of MGO 0.250 UV_10 surface adsorption sites. In addition, the heat of desorption (Q_{st}) values are more significant than recorded values of 28.40 to 10.50 kJ mol^{-1} for various adsorbents [175].

$$\Delta G^0 = -RTlnK_d \tag{3.1}$$

The variables, in this case, are the ΔG^o, R, T, and the adsorption equilibrium constant (lnK_d).

$$\ln(P) = -\frac{\Delta \mathrm{H}}{\mathrm{RT}} + C \tag{3.2}$$

The following variables are present: P, R, T, C (constant), and ΔH.

Table 3.12 Thermodynamic parameters (ΔG°, ΔH°, ΔS°) and Q_{st} of MGO 0.250 UV_10 adsorbent.

Adsorbent	**Temp. (K)**	**lnK_d**	**C_e**	**q_e**	**ΔG° (KJ mol^{-1})**	**ΔH° (KJ mol^{-1})**	**ΔS° (JK^{-1} mol^{-1})**	**Q_{st}**
MGO 0.250 UV_10	298	0.045	1.0	0.1	-1.18923456	13.1154139	3.63705207	39.7
	303	0.172	1.0	0.2	-3.58483844			40
	313	0.316	1.0	0.3	-6.74366752			39.4
	323	0.431	1.0	0.4	-11.6214834			39.9
				0.5				39.1
				0.6				38.5
				0.7				37.8
				0.8				37.1
				0.9				36.5
				1				35.9
				1.1				35.4
				1.2				34.8
				1.3				34.2
				1.4				33.3
				1.5				32.4
				1.6				31.5

Table 3.13 Thermodynamic parameters (ΔG°, ΔH°, ΔS°) of MGO 0.250 UV_10 adsorbent.

Adsorbent	**Temp (K)**	**K_d**	**ΔG° (KJ mol^{-1})**	**ΔH° (KJ mol^{-1})**	**ΔS° (JK^{-1} mol^{-1})**
MGO 0.250 UV_10	298	0.045	-1.18923456	13.1154139	3.63705207
	303	0.172	-3.58483844		
	313	0.316	-6.74366752		
	323	0.431	-11.6214834		

3.7 Adsorption-desorption mechanism

Understanding the CO_2 adsorption-desorption mechanism is linked to the kinetic thermodynamic parameters of the interaction between CO_2 and the adsorbent surface. In our study, we observed that for the adsorption study, CO_2 capture performance increased as the adsorption temperature decreased and for the desorption study temperature increased, CO_2 capture performance decreased, as seen in Table 3.8. The value of ΔH° was positive (+13.1154139 kJ mol^{-1}), showing the adsorption process is endothermic. Furthermore, the negative values of ΔG° signify that the adsorption process is spontaneous and feasible [168].

Furthermore, the Gibbs free energy (ΔG°) of the adsorbed CO_2, calculated in kJ mol^{-1}, was found to be relatively larger, indicating a faster rate of reaction, as depicted in Figure 3.15. This observation can be attributed to the presence of intermolecular forces, specifically quadrupole-to-quadrupole interactions between the adsorbed CO_2 quadrupoles and the defective graphene surface [174]. The CO_2 uptake exhibited high adsorption rates and reached maximum CO_2 adsorption. This result suggests that the sample's increased reactivity of oxygen functional groups, as shown in Figure 3.1 and Figure 3.7(d, e) contributed to a faster reaction rate, ultimately benefiting the potential for rapid adsorption. It is worth noting that the diffusion restrictions imposed by the system might have played a role in achieving this rapid adsorption as well as excellent desorption. Consequently, MGO 0.250 UV_10 demonstrates a chemisorption-based mechanism, primarily driven by van der Waals interactions [167]; this finding is satisfied by kinetic and thermodynamic data as discussed in the kinetic and thermodynamic study section.

3.8 Conclusions

In this study, we have synthesized monolithic graphene oxide-based adsorbents through the self-assembly process of graphene oxide and observed that MGO 0.250 (GO/OxA: 1:0.250) showed a CO_2 adsorption performance of 0.95 mmol g^{-1}. To further improve the CO_2 capture performance, we subjected MGO 0.250 to UV activation for different durations. The CO_2 capture performance depends upon various factors, i.e., morphology, surface area, and crystal structure, that were examined by different characterization techniques, such as SEM, BET, XRD, Raman, and FTIR analysis confirmed that the best optimum adsorbents of MGO 0.250 UV_10 show an increase in maximum CO_2 capture in comparison to all the synthesized adsorbents due to its highest porosity, basicity, and crystal/structural defects. MGO interlayer distance and D-band in Raman spectra show structural defects. The optimized adsorbent, MGO 0.250 UV_10, demonstrated the highest

CO_2 capture performance of approximately 1.65 mmol g^{-1}, owing to its elevated BET surface area of 577.3 m^2 g^{-1}. Additionally, in the regeneration study at 100 °C, the recovery % of the adsorbed CO_2 improved from 88.40 % for MGO 0.250 to 98.8 % for MGO 0.250 UV_10. It showed that it desorbed fast after adsorption and established a stable capacity after the adsorption-desorption cycles. The kinetic studies verified that the pseudo-second-order model is the best-fitted model due to higher R^2 values and a low error percentage (%). In contrast, the isotherm studies showed that the Freundlich model is the best fit due to the higher R^2 value. The thermodynamic studies show that the adsorption process is endothermic with the $\Delta H°$ value of +13.1154139 KJ $mol^{-1,}$ and the chemisorption is a characteristic property. The isosteric heat of adsorption (Q_{st}) depends on the heterogeneity of the adsorption site. Significantly, the monolithic graphene oxide-based adsorbents, specifically MGO 0.250 UV_10, displayed excellent dynamic CO_2 capture capacity (> 1 mmol g^{-1}) when subjected to simple UV activation. The adsorbents possess remarkable CO_2 capture capacities, selectivity, and regenerability, making them highly advantageous as a cost-effective pretreatment method for the CO_2 capture capacity of graphene-based adsorbents was increased using a most straightforward UV treatment, which has the potential to be simple to apply in the industrial sector at low CO_2 partial pressure.

Chapter 4 – Chemically Activated Carbon-Enriched Monolithic Graphene Oxide-Based Adsorbents for CO_2 Capture

4.1 Synthesis of monolithic reduced graphene oxide-based adsorbents

4.1.1 Synthesis of monolithic reduced graphene oxide

Graphene oxide was synthesized using the modified Hummer's method [129]. The self-assembly process of graphene oxide was frequently employed in this synthesis [13]. GO aqueous dispersion with a specified concentration (5 mg/ml) was generated through one hour of ultrasonication. After undergoing a three-hour stirring process at 90 °C, the system is cooled at 25 °C; the GO/OxA combination was prepared in various mass ratios (by weight) through the addition of oxalic acid. Specifically, the mixture was formulated at ratios of 1:1, 1:0.500, and 1:0.250. Subsequently, to achieve cohesive monolithic hydrogel, the homogeneous mixture underwent a two-hour hearing process at 90 °C. Following the preparation, the wet monolith underwent centrifugation to remove residual oxalic acid. To remove adsorbed water, the wet monolith underwent a final step of freeze-drying for 24 hours at -55 °C and a pressure of 0.6 mbar, utilizing the HyperCOOL Cooling Trap HC3055 from Korea. Scheme 4 illustrates the synthesis process of the monoliths. Distinct names were assigned to each synthesized MGOs as outlined in Table 4.1.

Table 4.1 Preparation process for MGO from GO:OxA (at ratios ranging from 1:0.250 to 1:1.000).

Samples name	GO: OxA	Temperature °C	Density (g^{-1} cm^3)
MGO 0.250	1: 0.250	90	0.030
MGO 0.500	1: 0.500	90	0.036
MGO 1.000	1: 1.000	90	0.040

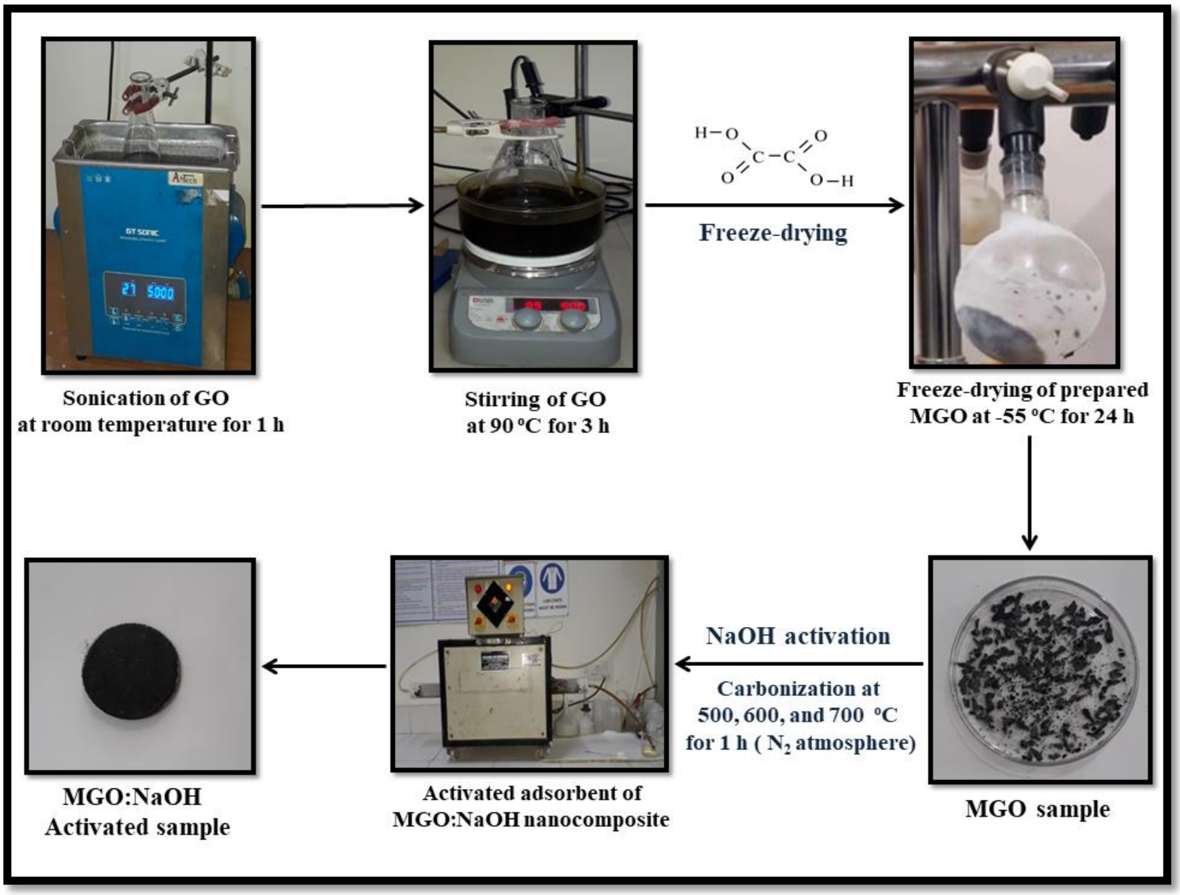

Scheme 4 Fabrication of monolithic adsorbents utilizing GO/rGO.

4.1.2 Synthesis of chemically activated adsorbent

The synthesis of chemically activated adsorbent was carbonized in successive processes [59,163,164,176]. The selected sample of MGO 0.250 was subjected to optimization at various temperatures, as documented in Table 4.2. The first process was to manually infuse MGO 0.250 with NaOH at varying weight ratios (MGO 0.250:NaOH=1-3), then the mixture was dried for 12 hours at 90 °C. The resultant prepared mixture was loaded on a clay boat and then located in the middle of the horizontally tubular furnace; after that, it ejected with N_2 (50 mL min^{-1}) for 10 minutes to blush out the air in the tubular furnace. Then, the samples were annealed at 600 °C with a ramping rate of 10 °C min^{-1} in the N_2 environment for 1 hour. The prepared chemically activated samples were left to cool naturally at 25 °C; then, the samples were rinsed with a 5% HCl solution, DI-water and dried in an oven for 12 hours at 60 °C to get MGO 0.250 nanocomposites. By employing this method, chemically activated adsorbents were produced, and distinct names were assigned to each synthesized MGO 0.250_x, as detailed in Table 4.3. The resulting samples were identified as MGO 0.250_x, with x representing the activation ratio of NaOH. Production yield was determined using the FPY method. The resulting MGO 0.250_2 adsorbent exhibited a production yield of 80.31%, as indicated in Table 4.4.

Table 4.2 Optimization of MGO 0.250 at 500, 600, and 700 °C.

Adsorbent	**Activation temperature (°C)**	**CO_2 Adsorption capacity (mmol g^{-1})**
MGO 0.250	500	1.05
MGO 0.250	600	1.23
MGO 0.250	700	1.15

Table 4.3 Chemical activation of MGO 0.250_x using different mass ratios of MGO 0.250 to NaOH

Samples Name	**Activation Time**	**Activation Temperature**	**MGO 0.250 : NaOH (weight in mg)**
MGO 0.250	-	-	-
MGO 0.250_1	1 h	600 °C	1:1
MGO 0.250_2	1 h	600 °C	1:2
MGO 0.250_3	1 h	600 °C	1:3

Table 4.4 Production yield of NaOH-activated adsorbent (MGO 0.250_2).

S.N.	**Process @ 1 (MGO 0.250)** **GO + OxA → MGO 0.250 + H_2O** **(1000 mg)+(250 mg) → (1050 mg)**				**Process @ 2 (MGO 0.250_2)** **MGO 0.250 + NaOH → MGO 0.250_2 + H_2O** **(1050 mg) + (2100 mg) → (3150 mg)**				**RTY Yield**
	Production Quantity	Obtained Quantity	Rejection Quantity	FPY Yield	Production Quantity	Obtained Quantity	Rejection Quantity	FPY Yield	
1	1250 mg	1050 mg	250 mg	84.00 %	3150 mg	2530 mg	620 mg	80.31 %	68.44 %

4.2 Characterization of adsorbents

4.2.1 Characterization of monolithic materials

The reduction of graphene oxide through a self-assembly process with oxalic acid at 90 °C resulted in the formation of monoliths, with the structural foundation primarily composed of GO. The control over the rGO and its structural characteristics is contingent upon the reduction temperature, a parameter that concurrently dictates the dynamics of the graphene oxide (GO) reduction process. Graphene oxide (GO) platelets are extensively acknowledged for containing epoxy, hydroxyl (-OH), and carboxyl (-COOH) groups, which are subsequently eliminated during the reduction process [130]. This process develops a porous hierarchical morphology in monolithic structures in the above-illustrated process. As revealed in Table 4.1, these monolithic adsorbents show ultra-low density. The ultra-low density range of prepared monolithic adsorbents was 0.03 to 0.04 g^{-1} cm^{3}. The mass-to-volume ratio, employing a range of 15 to 20 mg for mass and 0.5 cm^3 for volume, was employed in the calculation of density. After treatment with OxA, the density of monoliths increases with the increase in OxA, indicating that these monoliths are more compact due to the quicker process.

4.2.1.1 XRD analysis

Figure 4.1 illustrates XRD patterns of GO, MGOs, and MGO 0.250_x samples. The (0 0 1), (0 0 2), and (1 0 0) crystal planes are denoted by distinctive diffraction peaks at 10.70°, 26.90°, and 42.75°, respectively of GO, MGOs, and MGO 0.250_x [14,136,177]. The peak intensity slightly changes after carbonization at 600 °C for different mass ratios of MGO 0.250:NaOH; the peak intensity for MGO 0.250_1 (1:1) and MGO 0.250_3 (1:3) slightly decreases, whereas for MGO 0.250_2 (1:2) peak slightly increases. The discernment of this effect originates from the fluctuations in oxygen functionalities, marking the evident rise and subsequent decline in their presence, which was also confirmed from XPS survey scan analysis as revealed in Figure 4.7. The distinctive crystal diffraction peaks presented at 26.10, 25.20, 25.50, and 25.83° for MGO 0.250, MGO 0.250_1, MGO 0.250_2, and MGO 0.250_3, respectively.

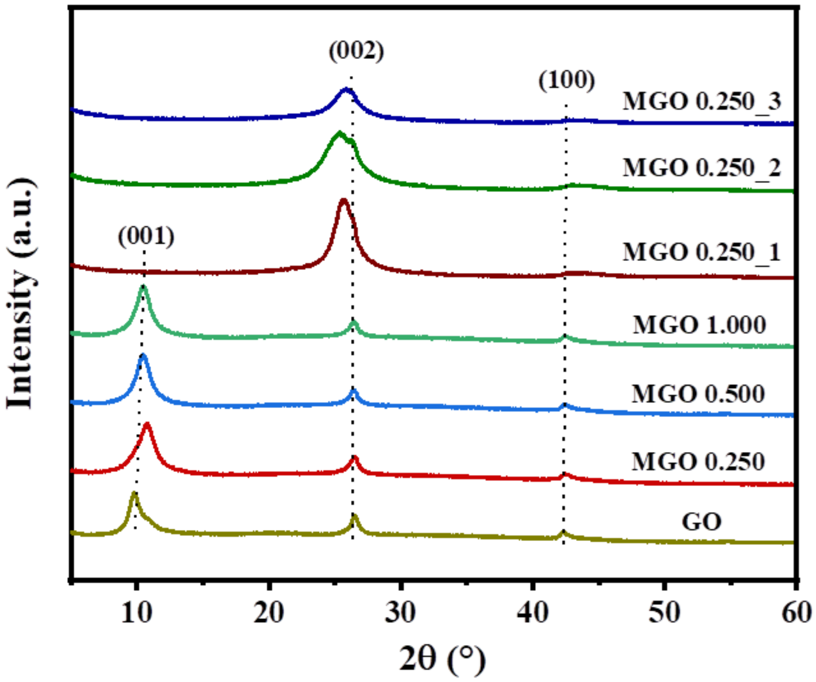

Figure 4.1 Wide-angle XRD patterns of GO, MGOs, and MGO 0.250_x adsorbents.

4.2.1.2 Raman spectral analysis

Raman spectral analysis of GO, MGOs, and MGO 0.250_x samples are revealed in Figure 4.2. The occurrence of the adsorbent peaks at 1300 cm^{-1} and 1500 cm^{-1} can be attributed to the D and G bands [14,131,140,141,177]. The D and G bands virtually equalize in intensity for MGO 0.250, indicating a modest amount of crystal lattice defects produced by a strong oxidation process and helpful for creating MGOs [10]. The I_D/I_G ratio slightly increases after activation with the values of 1.02, 1.06, 1.07, 1.09, 1.24, 1.38, and 1.31 for GO, MGO 1.000, MGO 0.500, MGO 0.250, MGO 0.250_1, MGO 0.250_2, and MGO 0.250_3 respectively. The rising I_D/I_G ratio serves as an indicative measure of the degree of disorder, with the presence of edges, ripples, and faults emerging as substantial contributing factors [144]. This may be due to the attack of NaOH on the oxygenic defect regions, which decreases the O/C atomic ratios of the adsorbents.

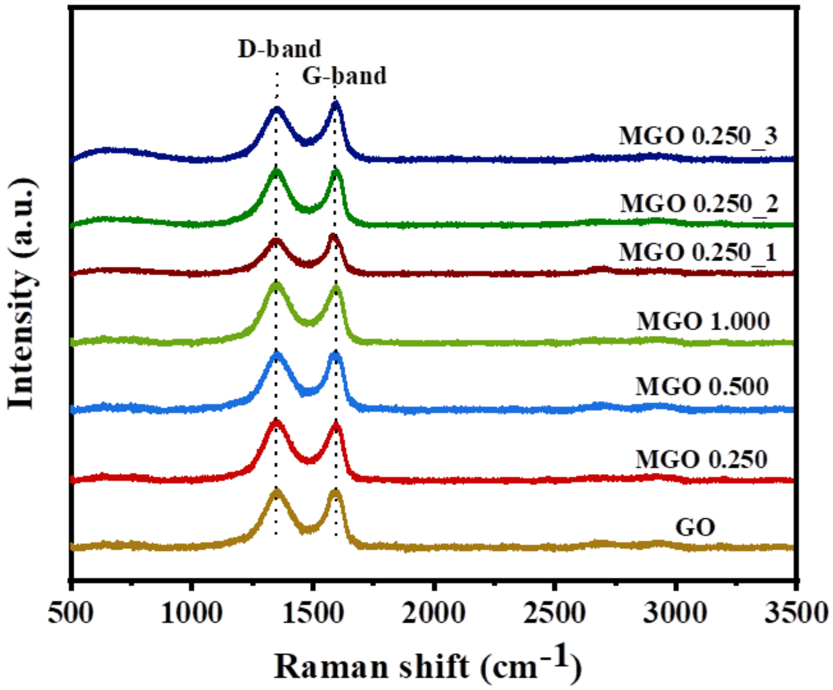

Figure 4.2 Raman spectra of GO, MGOs, and MGO 0.250_x adsorbents.

4.2.1.3 TGA analysis

Figure 4.3 shows the Thermogravimetric Analysis (TGA) curves for both MGO 0.250 and NaOH-activated MGO 0.250. The MGO 0.250 experiences loss of weight at 120 °C, ascribed to the presence of residual oxygen functional groups on its surface. After that, activated MGO 0.250 exhibits weight loss occurring between 400 °C and 600 °C, most likely due to the oxygen in the samples being oxidized and decomposed. The weight loss is in the following order: MGO 0.250 > MGO 0.250_1> MGO 0.250_3 > MGO 0.250_2. It was observed that MGO 0.250_2 is the most thermally stable adsorbent.

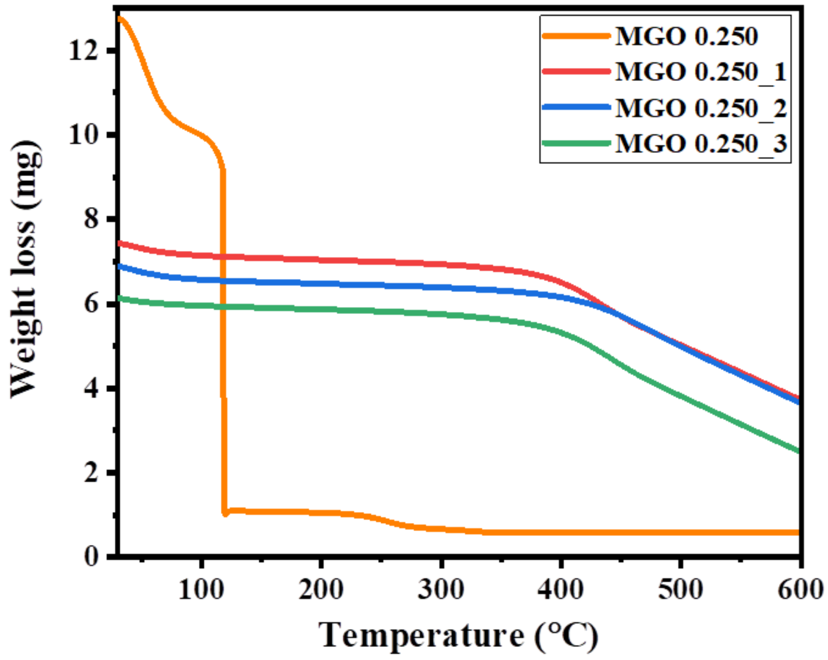

Figure 4.3 Thermogravimetric analysis curves for MGO 0.250, MGO 0.250_x, and GO adsorbents.

4.2.1.4 Surface area and pore volume analysis

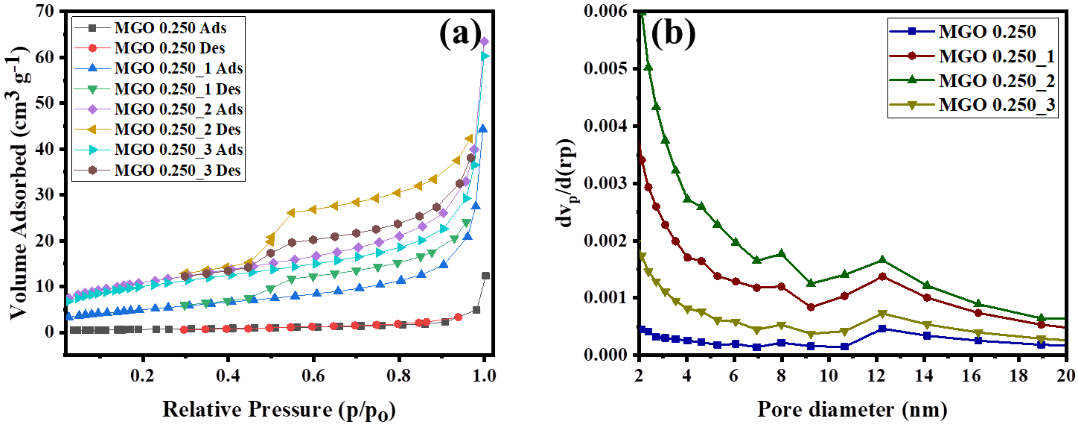

Figure 4.4 (a) N_2 adsorption-desorption isotherm curves, and (b) pore size distribution curves of different adsorbents.

The N_2 adsorption isotherms and the corresponding adsorption-desorption curve are illustrated in Figure 4.4(a) and as indicated in Table 4.5. Type-IV isotherms affirm the mesoporous character with pore diameter ranging between 5.0 and 20.0 nm. This study investigates the augmentation of specific surface area (SSA) subsequent to NaOH treatment. This phenomenon is likely attributed to the heightened porosity, which is particularly prominent in MGO 0.250_2, boasting a surface area of 753.9 m^2 g^{-1} and a total pore volume of 1.97 cm^3 g^{-1}. Despite certain MGO 0.250_x samples exhibiting surface areas considerably smaller than the projected 2630 m^2 g^{-1} for an individual graphene sheet, our findings remain noteworthy [145]. Nevertheless, these values surpass those of graphene aerogel, which stands at 512 m^2 g^{-1} [146], graphene sponge at 418 m^2 g^{-1} [147], and graphene nanoplates at 480 m^2 g^{-1} [148]. Figure 4.4(b) illustrates the PSDs obtained through the BJH method, highlighting that the predominant portion of the pore volume is attributed to apertures with a diameter below 20 nm. Notably, distinct PSDs emerge within the 5 to 16 nm range, signifying the presence of small mesopores across all MGOs in the basal plane. MGO 0.250_2 exhibits a more densely packed structure, as evidenced by Table 4.5. The shift in the maximum of the pore size distribution PSDs, transitioning from 3.59 nm for MGO 0.250_3 to 3.95 nm for MGO 0.250_2, suggests that elevating NaOH levels resulted in the formation of MGO with larger pores. Adjusting the MGO 0.250 to NaOH ratios conveniently allows for the concurrent modulation of the samples' porosity.

Table 4.5 Porous properties and elemental compositions of adsorbents under different conditions

Adsorbent	**SSA (m^2 g^{-1})**	**V_{total} (meso+micro) (cm^3 g^{-1})**	**V_t (meso) (cm^3 g^{-1})**	**Meso pore (%)**	**Average pore diameter (nm)**	**Elemental composition (%)**			
						C	**O**	**N**	**H**
MGO 1.000	289.2	0.69	0.46	66.66	5 to 20	67.91	30.84	-	1.25
MGO 0.500	297.7	0.75	0.51	68.00	5 to 20	66.97	31.93	-	1.10
MGO 0.250	311.1	0.88	0.61	69.31	5 to 20	65.21	33.98	-	0.81
MGO 0.250_1	520.8	1.19	0.85	71.42	5 to 20	73.10	23.79	2.40	0.71
MGO 0.250_2	753.9	1.97	1.55	78.68	5 to 20	72.57	25.01	1.90	0.52
MGO 0.250_3	668.6	1.60	1.21	75.62	5 to 20	69.60	28.21	1.50	0.69

4.2.1.5 FE-SEM, SEM, and HR-TEM analysis

Characterization through FE-SEM imaging aimed to collect information pertaining to porosity, surface morphology, and the monolith structure. Leveraging the FE-SEM image, the surface morphology of MGOs and MGO 0.250_x was examined, as illustrated in Figure 4.5. Research tends to prioritize the investigation of porous morphology, given the lower presence of OxA and the more discernible pores. Notably, the activation of MGO 0.250 with NaOH weight ratios ranging from 1:1 to 1:3 resulted in a discernible improvement in surface roughness. The resulting MGO 0.250_2 adsorbent exhibited morphological disorders, as depicted in SEM and HR-TEM images presented in Figure 4.6 [14,149,150,177]. When the water contact angle was more significant than (>90°), the MGO 0.250_x displayed poor wetting, while a slight contact angle (<90°) corresponds to larger surface wetting [178]. From Figure 4.5, the FE-SEM image observations connected to an increase in surface roughness after NaOH activation were also seen in these images. Contrastingly, it manifests a planar yet twisted shape, suggesting the influence of NaOH in augmenting the pore structure and consequently modifying the morphology of the graphene layers [179].

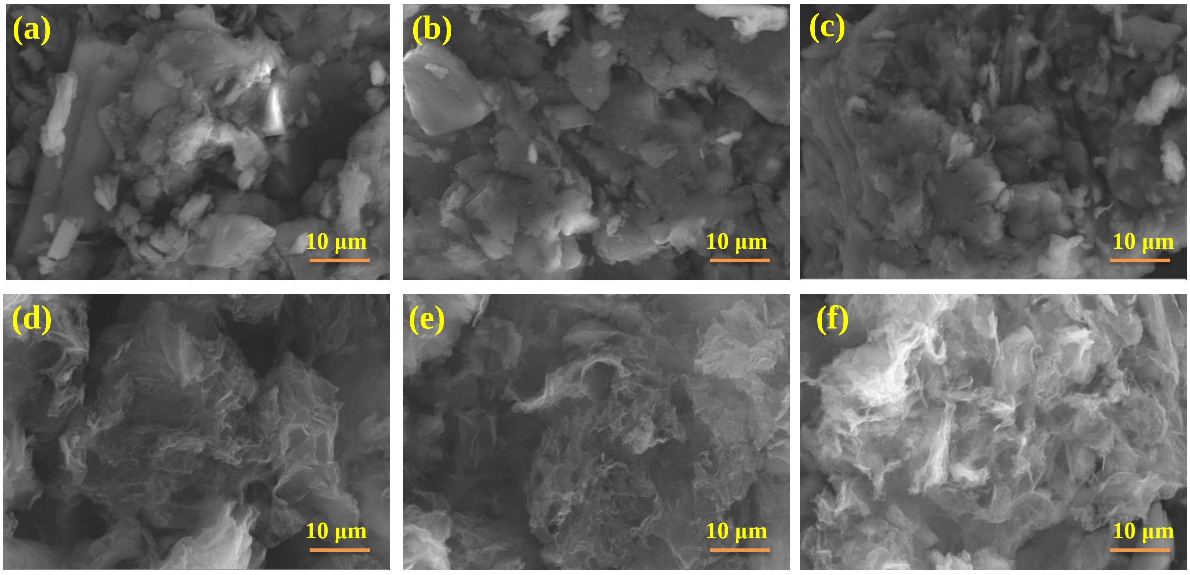

Figure 4.5 FE-SEM images of (a) MGO 1.000, (b) MGO 0.500, (c) MGO 0.250, (d) MGO 0.250_1, (e) MGO 0.250_2, and (f) MGO 0.250_3.

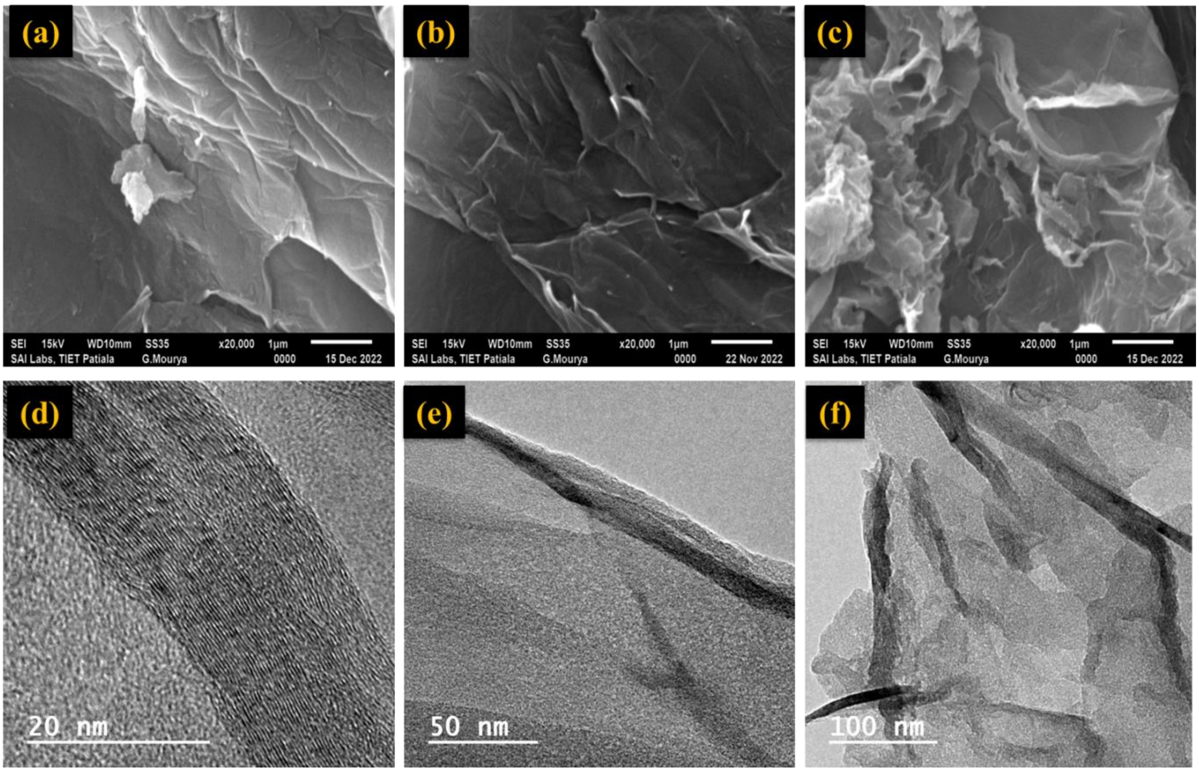

Figure 4.6 SEM images of (a) GO, (b) MGO 0.250, (c) MGO 0.250_2, and (d to f) HR-TEM image of MGO 0.250_2.

4.2.1.6 XPS analysis

Surface functionalities and O/C ratios of the synthesized adsorbents were determined through XPS analysis. Curves with binding energies approximately at 284.55 to 284.81 eV (C1), 284.96 to 285.24 eV (C2), 285.38 to 286.64 eV (C3), and 287.16 to 287.67 eV (C4) were employed for deconvoluting the C1s peak, depicted in Figure 4.8(a, c) [180–183]. In the case of MGO 0.250 and MGO 0.250_2, the C/O ratio experienced an increase from 1.919 to 2.901, attributed to the removal of various oxygen groups during NaOH activation, as depicted in Figure 4.7. Curves with binding energies approximately at 531.10 to 532.16 eV (O1), 532.76 to 533.46 eV (O2), and 533.12 to 534.90 eV (O3) were employed for deconvoluting the O1s peak, depicted in Figure 4.8(b, d) [181–183]. Table 4.6 reveals a notable relative area % for the O2, O3, and wear track surface chemical shifts in MGO 0.250_2, underscoring their significance [177,184,185]

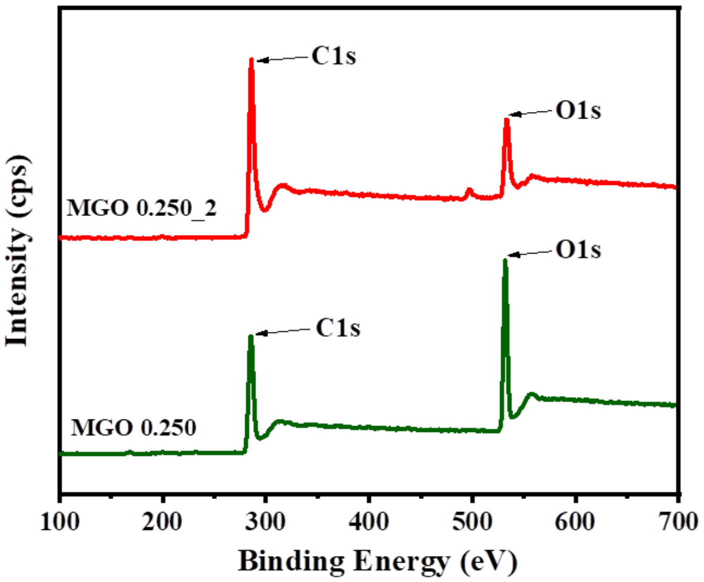

Figure 4.7 X-ray photoelectron spectroscopy survey spectra of MGO 0.250 and MGO 0.250_2 adsorbents.

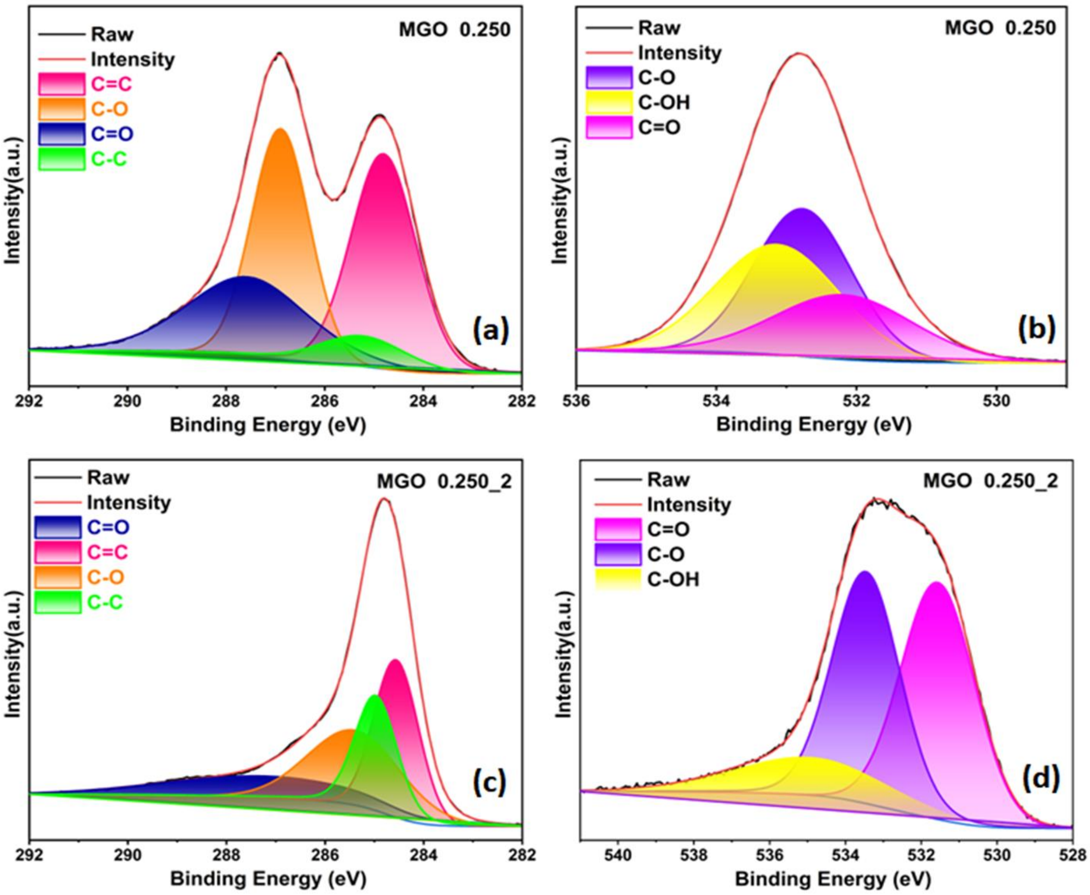

Figure 4.8 XPS spectrum of (a, c) C1s and (b, d) O1s.

Table 4.6 XPS data for MGO 0.250 and MGO 0.250_2 adsorbents.

Sample		**C1**	**C2**	**C3**	**C4**	**O1**	**O2**	**O3**
MGO 0.250	BE (eV)	284.81	285.24	286.64	287.67	532.16	532.76	533.12
	FWHM (eV)	1.47	2.55	1.21	2.90	2.31	1.64	2.07
	Area %	30.63	25.01	15.41	28.95	39.75	35.11	25.14
MGO 0.250_2	BE (eV)	284.55	284.96	285.38	287.16	531.56	533.46	534.90
	FWHM (eV)	1.06	1.01	2.24	4.76	2.29	2.11	4.77
	Area %	34.50	23.69	31.44	10.37	32.10	37.65	30.25

4.3 CO_2 adsorption performance

4.3.1 CO_2 adsorption performance of monolithic materials

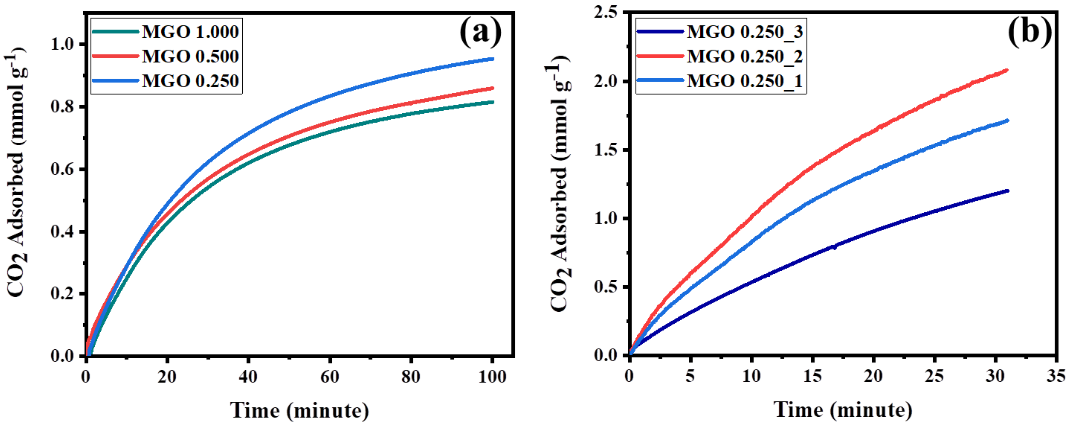

Figure 4.9 CO_2 capture performance of (a) MGOs and (b) MGO 0.250_x at 25 °C.

Figure 4.9(a, b) presents the assessment of CO_2 adsorption capacity for MGOs, and MGO 0.250_x. The precise CO_2 adsorption values for the optimized conditions are detailed in Table 4.2 and Table 4.7. The MGO 0.250_2 adsorbent attains its peak in the initial stage; the former exhibits a CO_2 capture capacity of approximately 2.10 mmol g^{-1}, surpassing the latter by about 2.6 times, as the former's capacity. The gaps created by graphene's layer-by-layer self-assembly process may be responsible for some of the CO_2 adsorptions on MGOs. In addition, all the MGOs showed a sharp increase in CO_2 capture performance [99,100,186];

therefore, accessing all of the MGOs pores was possible. Furthermore, the pressure range's isotherm under investigation did not show an apparent plateau. The ascending order of equilibrium CO_2 absorption at 25 °C and pressure 1 bar is as follows: MGO 0.250_1 with 1.20 mmol g^{-1}, followed by MGO 0.250_3 with 1.71 mmol g^{-1}, and MGO 0.250_2 leading with the highest capacity at 2.10 mmol g^{-1}. MGO 0.250_2 emerged as the optimal candidate, showcasing the highest surface area and optimal CO_2 adsorption performance. The literature also outlines the facilitation of low-pressure CO_2 adsorption through smaller pores [151].

Table 4.7 CO_2 adsorption capacity of MGOs, and MGO 0.250_x adsorbents at 25, 50 ^{o}C.

Adsorbents	**Ads. Time (min)**	**Adsorption Temperature (^{o}C)**	**CO_2 conc. (%)**	**Adsorption capacity (mmol g^{-1})**
MGO 1.000	100	25	50	0.81
MGO 0.500	100	25	50	0.86
MGO 0.250	100	25	50	0.95
MGO 0.250_1	30	25	50	1.20
MGO 0.250_2	30	25	50	2.10
MGO 0.250_3	30	25	50	1.71
MGO 0.250	100	50	50	0.79
MGO 0.250_2	30	50	50	1.35
MGO 0.250_2	30	25	20	1.70
MGO 0.250_2	30	50	20	1.11
MGO 0.250_2	30	100	50	0.80

Moreover, Table 4.8 indicates that MGO 0.250_2's CO_2 adsorption capability is similar to other graphene-based and carbonaceous materials at identical temperatures. increase in adsorption temperature from 25 °C to 50 °C, the amount of CO_2 adsorbed on MGO 0.250_2 decreased from around 2.10 mmol g^{-1} to approximately 1.35 mmol g^{-1}. The exothermic nature of adsorption is anticipated to contribute to the reduction in CO_2 adsorption at 50 °C.

Table 4.8 Comparing CO_2 adsorption performance between MGO 0.250_2 and other reported adsorbents.

Adsorbent	**Activation method**	**Experimental conditions**		**CO_2 Adsorbed (mmol g-1)**	**Ref.**
		CO_2 conc. (%)	**Temp. (°C)**		
MGO 0.250_2*	Chemical/NaOH (600 °C)	50	25	2.10	Present study
MGO 0.250_2*	Chemical/NaOH (600 °C)	50	50	1.35	Present study
3D graphene	Chemical/NaOH (500 °C)	50	25	1.71	[152]
HPGC-850	Chemical/ (850 °C)	100	0	1.76	[187]
PAN-KOH	Chemical/KOH (800 °C)	12.5	30	1.20	[51]
Carbon monolith	Chemical/KOH (25 °C)	15	30	0.66	[156]
EDA	Chemical/COOH (85 °C)	100	25	2.00	[157]
N-containing resin	Chemical/K_2CO_3 (700 °C)	100	25	1.90	[188]
HGF-II	Chemical/HNO_3 (500 °C)	100	25	1.40	[59]
WT-550-2	Chemical/KOH (550 °C)	10	25	4.54	[163]
MCF-700-0.2	Chemical/KOH (700 °C)	10	25	3.30	[176]
PHS-650-3	Chemical/KOH (650 °C)	10	25	4.18	[164]

4.3.2 Regeneration study

An investigation of the regeneration process for the activated adsorbents at four distinct temperatures (25, 50, 75, and 100 °C) is illustrated in Figure 4.10. As highlighted in Table 4.9, CO_2 recovery % experienced an increase with NaOH treatment, a phenomenon that was validated across a range of temperatures [19]. This effect is envisaged to occur by averting the entrapment of CO_2 within the MGO multilayer galleries, as reported by the active sites and demonstrated through the presented XRD data.

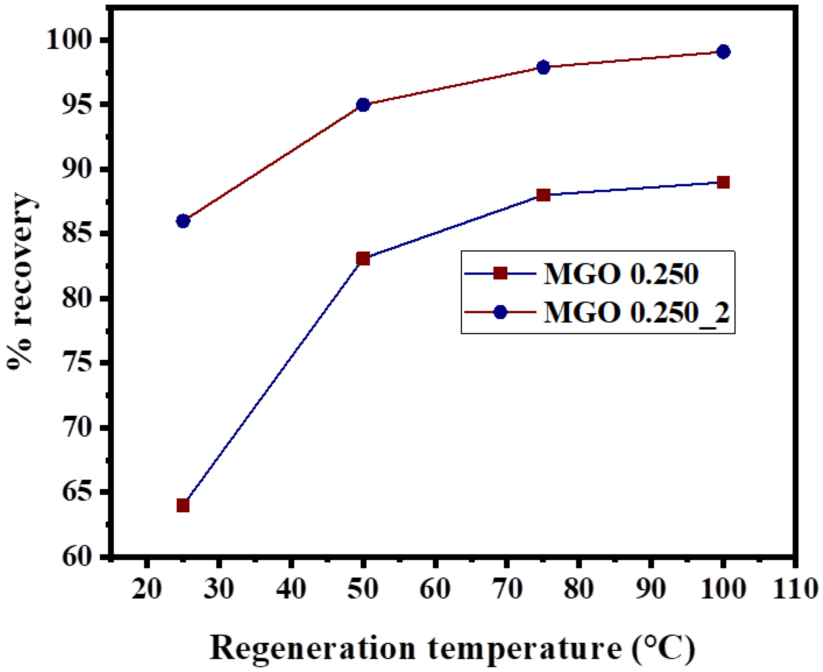

Figure 4.10 Regeneration study of MGO 0.250, MGO 0.250_2 adsorbents.

Table 4.9 Cycle of adsorption-desorption for adsorbents MGO 0.250 and MGO 0.250_2.

Adsorbent	**CO_2 Adsorbed (mmol g^{-1}) at 25 °C**	**CO_2 Desorbed (mmol g^{-1})**				**Recovery % of Adsorbed CO_2**			
		25 °C	50 °C	75 °C	100 °C	25 °C	50 °C	75 °C	100 °C
MGO 0.250	0.95	0.60	0.79	0.83	0.84	63.1	83.1	87.3	88.4
MGO 0.250_2	2.10	1.81	1.99	2.06	2.08	86.1	94.7	98.0	99.1

4.3.3 Selectivity

Produced adsorbents were employed in selectivity tests at 25°C, and the influence of NaOH-activated adsorbent was revealed in Figure 4.11. A significant decrease in N_2 adsorption is observed upon NaOH activation, as indicated by the results for MGO 0.250_2 on NaOH-activated adsorbents. In contrast to MGO 0.250 at 1 bar, the selectivity of MGO 0.250_2 experienced an approximately 3.7-fold increase, and this enhancement can be attributed to the improved CO_2 uptake. Table 4.10 reveals the outcomes of this study. For MGO 0.250_1, MGO 0.250_2, and MGO 0.250_3, selectivity values of 17.15, 35.00, and

34.20 were respectively recorded at 1 bar. According to the study's findings, the MGO 0.250_2 adsorbent is a great substitute for CO_2 recovery from flue gases [24,51,59,114].

Table 4.10 CO_2/N_2 adsorption selectivity on different adsorbents at 25 °C.

Adsorbent	**CO_2 Adsorbed (mmol g^{-1})**	**N_2 Adsorbed (mmol g^{-1})**	**CO_2/N_2 Selectivity**
	1 bar	**1 bar**	**1 bar**
MGO 0.250	0.95	0.10	9.50
MGO 0.250_1	1.20	0.07	17.14
MGO 0.250_2	2.10	0.06	35.00
MGO 0.250_3	1.71	0.05	34.20

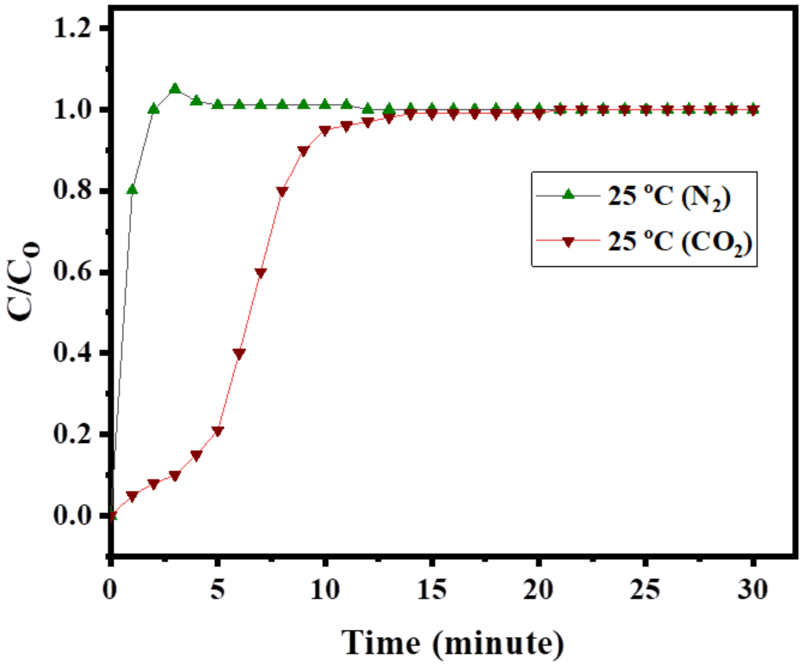

Figure 4.11 CO_2/N_2 selectivity curve of MGO 0.250 and MGO 0.250_x adsorbents.

4.3.4 Breakthrough curves

Figure 4.12 presents the breakthrough curves, evaluating the CO_2/N_2 binary gas mixture with a 50% CO_2 flowing at 25 °C and 1 bar pressure. The dynamic CO_2 adsorption capacity is approximately 1.0 mmol g^{-1}. CO_2 was observed to emerge in the effluent after a certain duration, whereas N_2 was promptly detected. This demonstrates that N_2 can't adsorb as well as CO_2. Initially, the active sites of the adsorbent are predominantly occupied by N_2, as evidenced by C/C_o for $N_2 > 1$. Nevertheless, as time progresses, there is a gradual displacement of N_2 by CO_2, highlighting the adsorbent's stronger affinity for CO_2 [51,114].

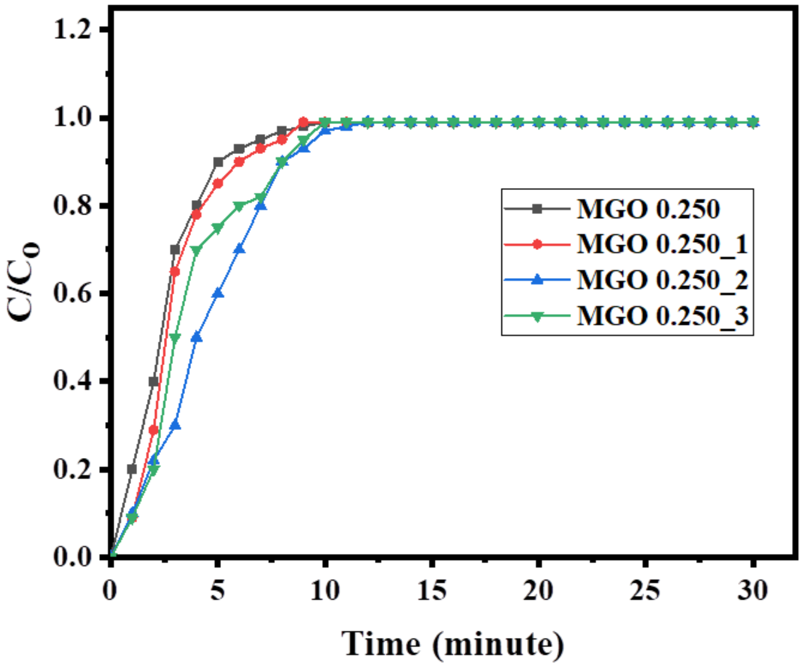

Figure 4.12 Breakthrough curves of MGO 0.250 and MGO 0.250_x adsorbents.

4.3.5 Multiple adsorption-desorption cycles

Figure 4.13 depicts the successive adsorption-desorption cycles of the adsorbent, with adsorption occurring at 25 °C and desorption at 150 °C. MGO 0.250_2 consistently exhibits adsorption of nearly 2.10 mmol g^{-1} throughout multiple adsorption-desorption cycles without any noticeable efficiency reduction. The desorption of CO_2 necessitates approximately 1.18 MJ of heat energy per kilogram of CO_2. Following numerous cycles, the CO_2 uptake remained consistently constant for MGO 0.250_2, showcasing its exceptional regenerability and cyclic stability outlined in Table 4.9. Due to the presence of metastable states between the sorbate and sorbent, the pressure falls below the thermodynamic equilibrium, signifying that MGO 0.250 encounters challenges in releasing the adsorbed CO_2 [189]. These findings underscore the advantage of treating MGOs with NaOH to facilitate the displacement of adsorbed CO_2.

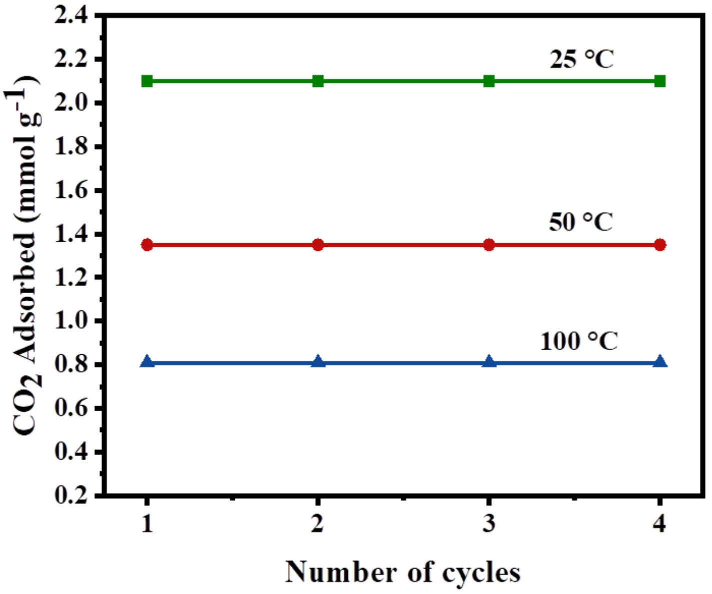

Figure 4.13 MGO 0.250_2 adsorbent underwent repeated cycles of CO_2 uptake at 25 °C, 50 °C, and 100 °C.

4.4 Adsorption kinetic study

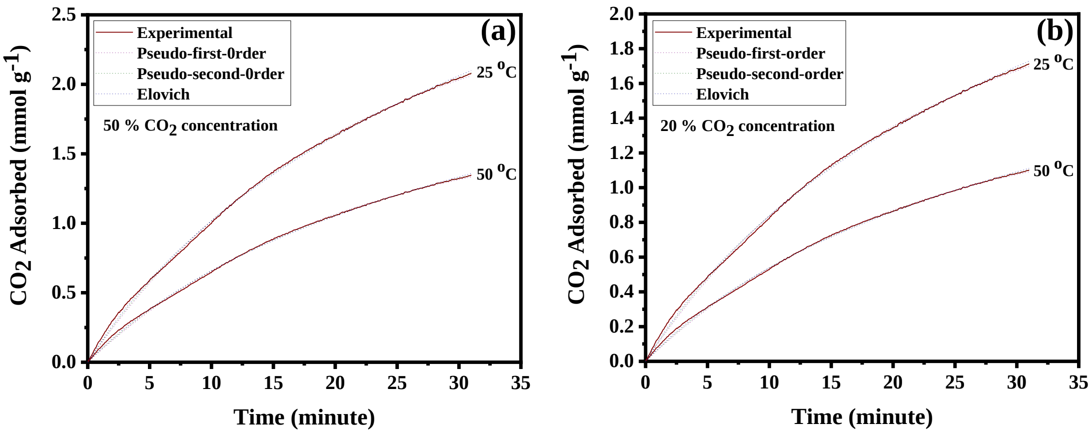

Figure 4.14 Experimental data fitting with kinetic models: (a) 50 % CO_2 concentration flow of MGO 0.250_2 adsorbent, and (b) 20 % CO_2 concentration flow of MGO 0.250_2 adsorbent.

Table 4.11 Kinetic models and parameters of MGO 0.250_2 adsorbent.

Kinetic models	**Parameters**	**Sample (MGO 0.250_2)**	
		25 °C	**50 °C**
Pseudo-first-order	q_e	2.10	1.35
	k_1	0.59	0.41
	R^2	0.977	0.979
	Error (%)	2.60	2.01
Pseudo-second-order	q_e	2.55	1.89
	k_2	0.45	0.39
	R^2	0.991	0.995
	Error (%)	1.69	1.33
Elovich	β (q_e)	2.15	1.36
	α (k_n)	0.56	0.41
	R^2	0.983	0.986
	Error (%)	2.22	1.83

In operational conditions with a pressure of 1 atmosphere, temperatures ranging from 25 to 50 °C, and CO_2 flow concentrations varying between 50% and 20%, the MGO 0.250_2 demonstrates enhanced CO_2 adsorption kinetics, exhibiting a faster rate of adsorption. Figure 4.14(a, b) depicts significant CO_2 uptake occurring at an elevated maximum of 94% CO_2 adsorption. This observation aligns more closely with the outcomes of previous experiments, reinforcing the consistency of the findings [59,114,163,164,190]. Diffusional constraints were suggested to be the cause of the sample's enhanced oxygen functionality and its propensity for quick adsorption. Consequently, the physisorption type of fitting, such as by van der Waals interaction, is revealed by MGO 0.250_2 [167]. These results unequivocally establish the capability of MGO 0.250_2 to operate with exceptionally short adsorption/desorption cycle lengths, presenting a notable economic advantage for commercial deployment. This material effectively demonstrates its potential to separate CO_2 from flue gases. In order to determine the adsorption rate and the adsorbent's capacity to adsorb a larger amount of adsorbate, adsorption kinetic studies are necessary [116–119], the formula provided in Equations 2.5, 2.7, and 2.8. Various kinetic models have been explored in this experimental study, as illustrated in Figure 4.14(a, b) because the lower error percentage (%) and higher R^2 values observed adhered to the pseudo-second-order kinetic model. This model is identified as more suitable than other models, as shown in Table 4.11.

4.5 Adsorption isotherm study

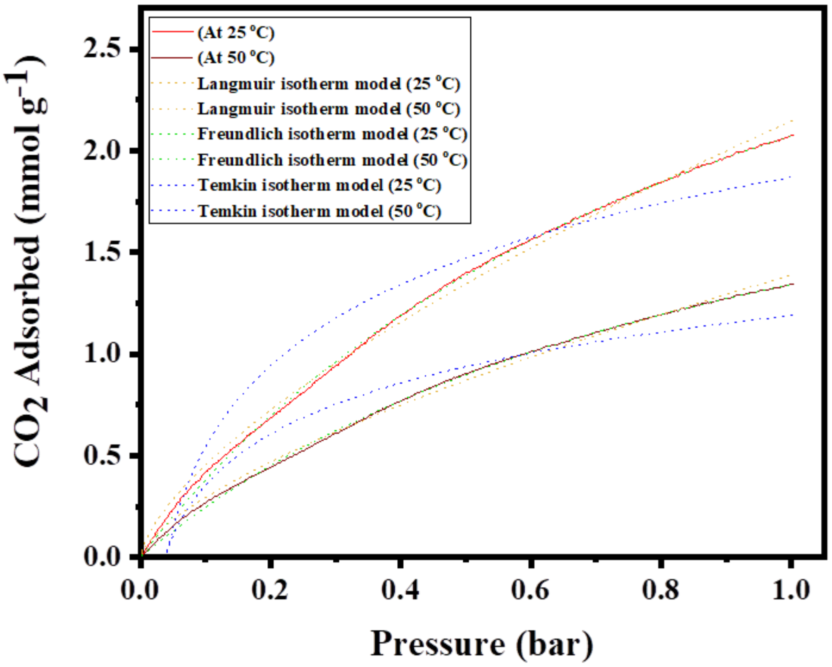

Figure 4.15 Experimental data fitting with isotherm model at 25 °C, 50 °C of MGO 0.250_2 adsorbent.

The determination of the adsorption mechanism and the elucidation of the roles played by the CO_2 adsorption procedure were achieved through an adsorption isotherm analysis. In this investigation, we employed Equations 2.10, 2.11, and 2.12 to detail the fitting of isotherm models—Langmuir, Freundlich, and Temkin to experimental CO_2 adsorption data. The computed and experimental R^2 values for various isotherm models are demonstrated in Table 4.12. As depicted in Figure 4.15, the superior R^2 values affirm

Freundlich isotherm model. This model has been identified as more suitable than other models. Adsorbent surface heterogeneity is illustrated by employing the Freundlich isotherm model. The optimum value for CO_2 adsorption at low temperatures is suggested by the K_F values ($n < 1$) [168]. The Freundlich model for MGO 0.250_2 adsorbent best fits experimental data with higher R^2 values, as observed in Table 4.12.

Table 4.12 Isotherm model and its parameters of MGO 0.250_2 adsorbent.

Isotherm model	**Parameters**	**Sample (MGO 0.250_2)**	
		25 °C	**50 °C**
Langmuir	q_m (mmol g^{-1})	2.146	1.388
	K_L (atm^{-1})	0.673	0.673
	R^2	0.995	0.995
Freundlich	K_F (atm^{-1})	1.009	1.009
	N	4.108	2.658
	R^2	0.999	0.999
Temkin	K_T (atm^{-1})	25.712	26.698
	B (KJ mol^{-1})	0.575	0.362
	R^2	0.882	0.880

4.6 Thermodynamic study

The determination of thermodynamic parameters crucially hinges on the interaction between CO_2 and the adsorption sites on the adsorbent surface during the CO_2 adsorption process. Equation 4.1 was used to measure the $\Delta G°$, whereas $\Delta S°$, $\Delta H°$ in KJ mol^{-1} can be determined through the Vant Hoff plot and Equation 2.14 [170], and the Q_{st} by Equation 2.15 [171]. Table 4.13 and Table 4.14 show calculated values of thermodynamic factors. The negative value of $\Delta H°$ (-11.1564133 KJ mol^{-1}) shows the process is exothermic; on the other hand, the value of $\Delta H°$ lies in the range between $< \pm 20$ KJ mol^{-1} showing the nature is predominantly physisorption [171]. Moreover, negative $\Delta G°$ values show the adsorption process is spontaneity and feasibility [168]. The positive $\Delta S°$ values (+4.7370520 JK^{-1} mol^{-1})

suggest an increased affinity of adsorbents, indicating a rise in randomness or disorder at the solid/gas surface. Utilizing the Equation 4.2, the Q_{st} values for MGO 0.250_2 were calculated at different q_e, ranging from 25.3 KJ mol^{-1} to 41.0 KJ mol^{-1}, with an average of approximately 33.8 KJ mol^{-1}, as detailed in Table 4.13. On the other hand, the isosteric heat of the activated adsorbent increased significantly, especially with higher CO_2 loadings, it reached approximately 41.00 KJ mol^{-1}. The adsorbed CO_2 molecules demonstrate strong lateral interactions with one another and are responsible for this behavior, according to the Fowler-Guggenheim model [173], which explains the interaction energy between the molecules. This phenomenon is further substantiated by the existence of intermolecular forces on the substandard graphene surface [174]. Recent investigations on CO_2 adsorption by carbonaceous materials have also reported a similar relationship between isosteric temperatures of adsorption and surface coverage [51,191,192].

The Q_{st} values were measured at various temperatures, revealing fluctuations in randomness and disorder. The increase in surface coverage aligns with the heterogeneous behavior of the surface adsorption sites of MGO 0.250_2. Moreover, in comparison to reported values ranging from 28.40 to 10.50 KJ mol^{-1} for different samples, the Q_{st} values are more significant [175], signifying the stronger attraction toward CO_2 heat of adsorption. A graph is plotted Q_{st} against 1/T (K^{-1}), as shown in Figure 4.16.

$$\Delta G^0 = -RTlnK_d \tag{4.1}$$

$$\ln(P) = -\frac{\Delta \mathrm{H}}{\mathrm{RT.}} + C \tag{4.2}$$

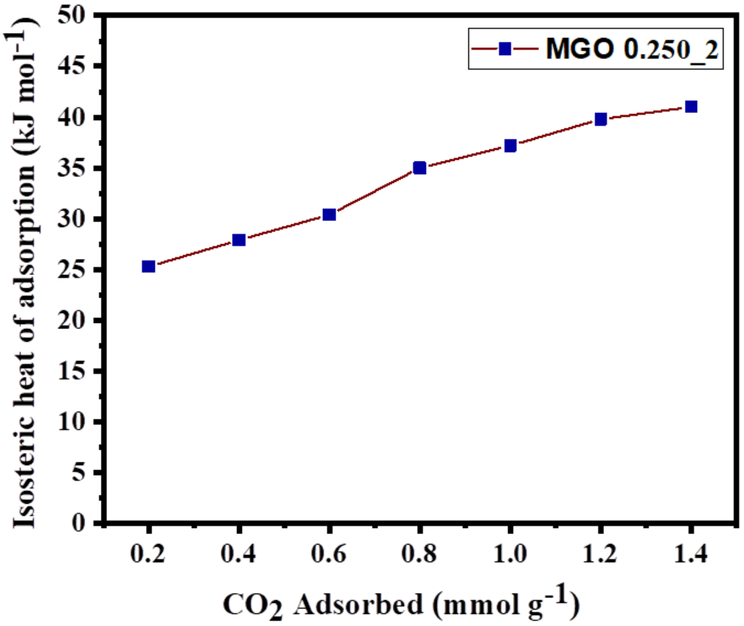

Figure 4.16 Plot of Q_{st} verses q_e for CO_2 adsorption by MGO 0.250_2 adsorbent.

Table 4.13 Thermodynamic parameters (ΔG°, ΔH°, ΔS°) of MGO 0.250_2 adsorbent.

Thermodynamic parameter of CO_2 adsorption						**Isosteric heat of adsorption**	
Adsorbent	**Temp (K)**	**K_d**	**ΔG° (KJ mol^{-1})**	**ΔH° (KJ mol^{-1})**	**ΔS° (JK^{-1} mol^{-1})**	**q_e (mmol g^{-1})**	**Q_{st} KJ mol^{-1}**
MGO 0.250_2	298	0.048	- 1.1189234	- 11.1564133	+ 4.7370520	0.20	25.3
	303	0.182	-4.4584838			0.4	27.9
	313	0.336	-7.8743667			0.6	30.4
	323	0.470	-13.2621483			0.8	35.0
						1.0	37.2
						1.2	39.8
						1.4	41.0

Table 4.14 Thermodynamic parameters (ΔG°, ΔH°, ΔS°) of MGO 0.250_2 adsorbent.

Adsorbent	**Temp. (K)**	**$\ln K_d$**	**C_e**	**q_e**	**ΔG° (KJ mol^{-1})**	**ΔH° (KJ mol^{-1})**	**ΔS° (JK^{-1} mol^{-1})**
MGO 0.250_2	298	0.048	1.0	1.05	-1.1189234	-11.1564133	4.7370520
	303	0.182	1.0	1.2	-4.4584838		
	313	0.336	1.0	1.4	-7.8743667		
	323	0.470	1.0	1.6	-13.2621483		

4.7 Mechanism of CO_2 capture performance enhancement

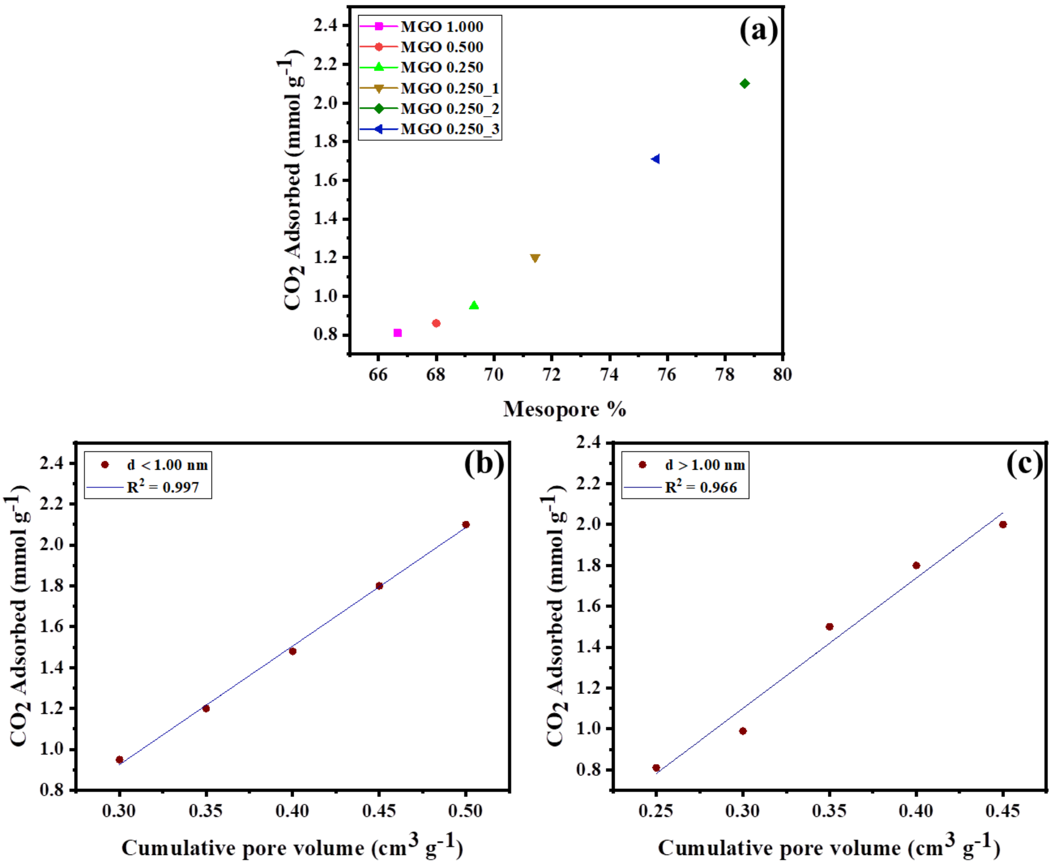

Figure 4.17 (a) Relation between CO_2 adsorption capacity with mesopore %, and linear relation between CO_2 adsorption capacity with cumulative pore volume (b) d < 1.00 nm, and (c) d >1.00 nm.

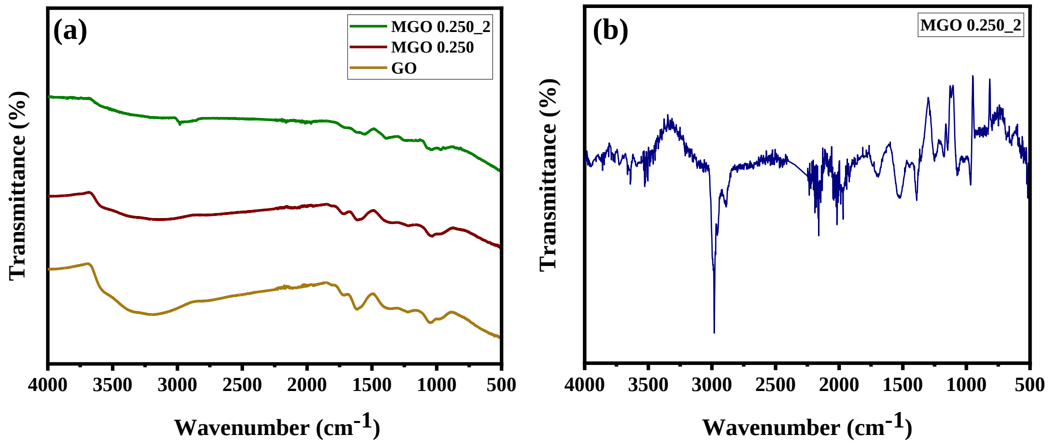

Figure 4.18 FT-IR spectra of (a) before CO_2 adsorption for GO, MGO 0.250, MGO 0.250_2 adsorbents and (b) after CO_2 adsorption for MGO 0.250_2 adsorbent.

The physiochemical, thermodynamic, and kinetic characteristics play a pivotal role in shaping the approach for CO_2 capture. The size and shape of the pores are critical factors, and their abundance is essential for the effective functioning of the CO_2 capture mechanism. Furthermore, a high CO_2 adsorption rate requires an adsorbent with a large volume and surface area of pores. A parallel increase in the percentage of mesopores is observed in Figure 4.17(a) as CO_2 adsorption capability rises. The primary reason for the increase in CO_2 adsorption is the proportional rise in mesopores, which ranges from 66.66 to 78.68 %, as outlined in Table 4.5. According to Figure 4.17(b, c), the $d < 1$ nm range exhibits the best linear connection ($R^2 = 0.996$), with a higher R^2 value than the $d > 1$ nm range.

By utilizing FT-IR spectra, we successfully identified individual adsorption peaks, as depicted in Figure 4.18(b). The corresponding assignments for these peaks are detailed in Table 4.15. Significant variations were observed between the two spectra in the 1600 to 1200 cm^{-1} range. Table 4.15 and Figure 4.18 present the outcomes of our efforts to isolate the spectra for a more comprehensive analysis of the 1600 to 1200 cm^{-1} range. The existence of HCO_3^- recommended the development of bicarbonate, whereas the peak equivalent to COO^- showed the development of carbamate. These results lend support to the notion that π-π interactions can facilitate the self-assembly of 2D porous graphene into 3D hierarchical porous graphene [149,150]. Furthermore, the wetting properties of MGO 0.250_x were evaluated based on the water contact angle calculation [178]. Furthermore, in comparison to MGOs, MGO 0.250_x displayed larger interlayer spaces, evident from the slight shift in the (002) diffraction peaks as illustrated in the XRD patterns presented in Figure 4.1. Consequently, this contributed to the augmentation of the surface area and an increase in adsorption capacity, as outlined in Table 4.5.

Unveiling the thermodynamic parameters and elucidating the intricacies of CO_2 interaction with the adsorbent surface is indispensable for a thorough comprehension of the

CO_2 adsorption mechanism. In our investigation, as the adsorption temperature increased, we observed a decrease in capture performance, indicating an exothermic and physisorption-based adsorption process, as illustrated in Table 4.13 and Table 4.14. The exothermic nature is confirmed by the ΔH° (-11.1564133 KJ mol^{-1}), providing robust support for its physisorption-based mechanism [171]. Furthermore, as depicted in Figure 4.14, the ΔG° was determined to be relatively higher, indicating an accelerated rate of the reaction [115,174]. The CO_2 adsorption exhibited exceptional rates, reaching the peak of 94% CO_2 adsorption. The aforementioned observation suggests that the heightened reactivity of oxygen functionality, as illustrated in Figure 4.8(d), contributed to an accelerated reaction rate, thereby enhancing the probability of rapid adsorption. It's crucial to highlight that the rapid adsorption could potentially be attributed to diffusion constraints within the system. With van der Waals interactions acting as the primary driving force, MGO 0.250_2 thus exhibits a physisorption-based process [167].

Table 4.15 Relevant IR bands after CO_2 adsorption for MGO 0.250_2 in 1600 to 1200 cm^{-1} range.

Wavenumber (cm^{-1})	Assignments	Species
1590	COO^- stretching Vibration	Carbamate
1431	COO^- stretching Vibration	Carbamate
1382	HCO_3^- stretching Vibration	Bicarbonate
1267	C-O deformation vibration of HCO_3^-	Bicarbonate

4.8 Conclusions

In this investigation, the CO_2 adsorption efficiency of the developed MGO-based adsorbents was assessed across various parameters, including temperature, different concentrations of CO_2, and a constant pressure of 1 bar. Specifically, MGO 0.250_2 stands out as the optimal adsorbent, showcasing an enhanced capacity for maximum CO_2 adsorption. We observed that MGO 0.250_2 activated adsorbent gives the best CO_2

adsorption of 2.10 mmol g^{-1} due to having higher surface areas of 753.9 m^2 g^{-1}. Moreover, in the case of MGO 0.250 and MGO 0.250_2, the regeneration study performed at 100 °C demonstrated an enhancement in the recovery % increasing from 86.40% to 90.10%. This indicates a rapid desorption process post-adsorption, with a consistently stable adsorption capacity observed throughout the adsorption-desorption cycles. With its lower error percentage (%) and higher R^2 values, the kinetic experiments confirmed the excellent fit of the pseudo-second-order model. Similarly, the elevated R^2 value of the Freundlich model suggests that it is the most fitting model in the isotherm investigations as well. Furthermore, the thermodynamic parameters confirm that the characteristic nature of the adsorption is physisorption. The dynamic CO_2 capture capacity of MGO 0.250_2, surpassing 1 mmol g^{-1}, positions it as a promising candidate for industrial applications.

Chapter 5 – Chemically Activated Monolithic Graphene Oxide Frameworks for CO_2 Capture

5.1 Synthesis of monolithic graphene oxide-based adsorbents

5.1.1 Synthesis of monolithic graphene oxide

Graphene oxide was produced by modified Hummer's method [129]. The preparation of monolithic graphene oxide commenced with a self-assembly process involving GO [13,193]. Initially, a GO aqueous dispersion was formulated by ultrasonication of a measured amount (5 mg/ml) for 1 hour. This dispersion was subsequently stirred for 3 hours at 90 °C, followed by gradual cooling to room temperature. Subsequently, reducing agent—malic acid (MaA) was introduced in distinct mass ratios to create a homogeneous mixture of GO/MaA (1:1, 1:0.500, 1:0.250). The resulting mixture was subjected to a 2-hour thermal treatment at 90 °C in a hot air oven to induce reduction and yield a monolithic hydrogel. Post-treatment, the wet monolith underwent a thorough cleansing regimen through centrifugation (at 7000 RPM for 10 minutes) to remove excess MaA (unoxidized groups). The advancement of the cleansing regimen was followed through conductivity measurements of the water solution, and the structures were deemed clean when the recorded value fell below 10 μS/cm. The ensuing wet monolith was then subjected to freeze-drying using a HyperCOOL Cooling Trap HC3055 (Korea) set at -55 °C and a pressure of 0.6 mbar for 24-hour duration. Scheme 5 represents the synthesis route of monolithic graphene oxide-based adsorbents. The generated samples were designated as MGOs and correspondingly labeled as per Table 5.1. Detailed information regarding the production yield of the MGO 0.250 sample, amounting to approximately 84%, can be found in Table 5.2.

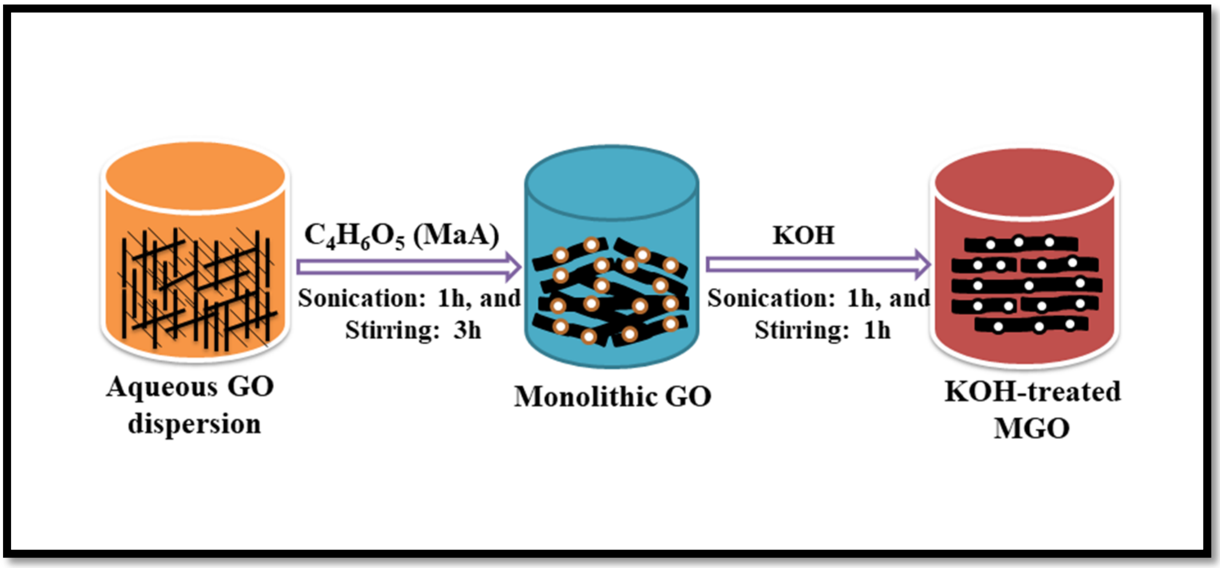

Scheme 5 synthesis scheme for monolithic graphene oxide-based adsorbents.

Table 5.1 Preparation of MGOs with different mass ratios of GO: MaA.

Samples name	GO: MaA	Temperature °C	Density (g^{-1} cm^3)
MGO 0.250	1: 0.250	90	0.191
MGO 0.500	1: 0.500	90	0.229
MGO 1.000	1: 1.000	90	0.254

5.1.2 Synthesis of KOH-treated adsorbent

The preparation of the KOH-treated adsorbent through carboxylation of hydroxyl groups on MGO by chloroacetic acid method [58,194,195] involved a sequential procedure initiated by incorporating a measured amount (5 mg/ml) of aqueous dispersion into a conical flask, followed by ultrasonication for 1 hour. Subsequently, 1 gm of KOH and 1gm of chloroacetic acid [58,194] were introduced into the prepared suspension and allowed to interact for 1 hour. The resulting dispersion underwent stirring for an additional hour at 90 °C, following which it was gradually cooled to room temperature. The resulting wet KOH-treated monolith was subject to a cleansing process via centrifugation (at 7000 RPM for 10 minutes) to effectively eliminate any excess chloroacetic acid content. The advancement of the cleansing regimen was followed through conductivity measurements of the water solution, and the structures were deemed clean when the recorded value fell below 10 µS/cm. The resultant wet monolith was then subjected to freeze-drying at -55 °C and a pressure of 0.6 mbar over a 24-hour duration. Consequently, chemical bonding plays a crucial role in chemical reactions, specifically through covalent linkage, as illustrated in the reaction sequence from Equation 5.1 to Equation 5.3. Pictures of the monoliths taken both before and after the drying process are shown in Figure 5.1(a, b). The resultant sample was labeled as MGO 0.250_KOH. To quantify the production yield of the MGO 0.250_KOH material, the First Pass Yield (FPY) method was employed. It is noteworthy that the MGO 0.250_KOH sample demonstrated a production yield of approximately 82.92%, as comprehensively elaborated in Table 5.2.

$$GO \xrightarrow[\text{Freeze-drying}]{C_4H_6O_5} MGO \tag{5.1}$$

$$MGO + ClCH_2COOH \xrightarrow[90\,^{\circ}\mathrm{C}]{\mathrm{KOH}} MGO.CH_2COOH + KCl + H_2O \tag{5.2}$$

$$MGO.CH_2COOH \xrightarrow[24-hour]{Freeze-drying} MGO.CH_2COOH \tag{5.3}$$

Table 5.2 Production yield of MGO 0.250 and MGO 0.250_KOH adsorbents.

S.N.	**Process @ 1 (MGO 0.250)** **GO + MaA → MGO 0.250 + H_2O** **(1000 mg)+(250 mg) → (1050 mg)**				**Process @ 2 (MGO 0.250_2)** **MGO 0.250 + kOH → MGO 0.250_KOH + H_2O** **(1050 mg) + (1000 mg) → (3150 mg)**				**RTY Yield**
	Production Quantity	Obtained Quantity	Rejection Quantity	FPY Yield	Production Quantity	Obtained Quantity	Rejection Quantity	FPY Yield	
1	1250 mg	1050 mg	250 mg	84.00 %	2050 mg	1700 mg	350 mg	82.92 %	69.65 %

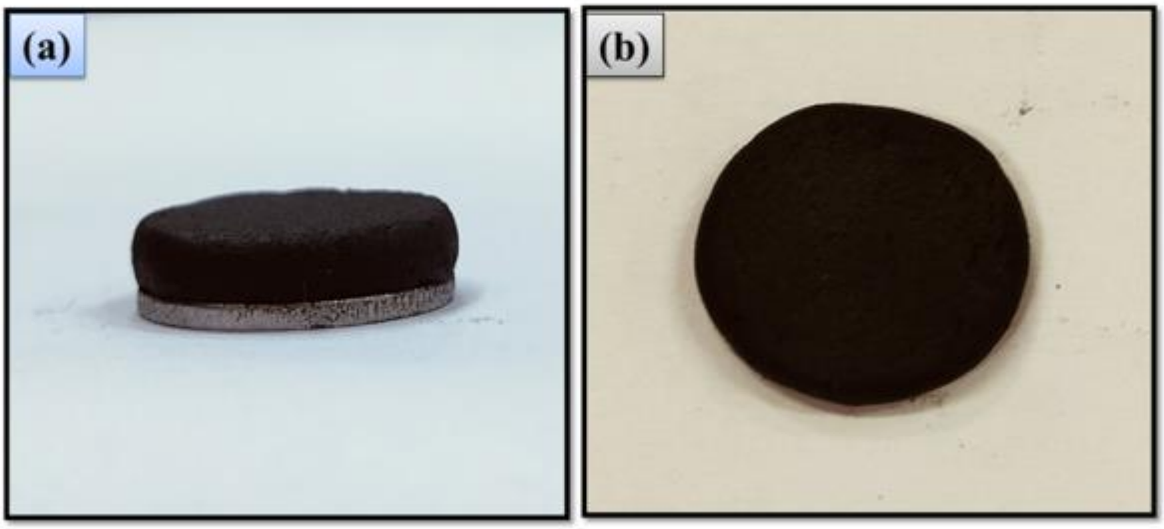

Figure 5.1 Pictures of the monoliths taken (a) before and (b) after the drying process (the monolith is depicted on the face of an Indian one-rupee coin).

5.2 Characterization of adsorbents

5.2.1 Characterization of monolithic materials

The monolithic structures were fashioned by subjecting graphene oxide (GO) to a MaA-driven reduction process within an aqueous dispersion at a temperature of 90 °C. The reduction temperature assumes a pivotal role in shaping the structure of the resultant reduced graphene oxide. In the course of the reduction process, the -OH functional groups are eliminated from the graphene oxide platelets [130]. This reduction-induced transformation underpins the emergence of a porous and hierarchically organized morphology within the monolithic constructs. As depicted in Table 5.1, the monolithic adsorbents manifest remarkably low densities, ranging between 0.191 to 0.254 g/cm³. Intriguingly, the density of the monoliths is exhibited in Table 5.1 as an ascending trajectory with the augmentation of MaA content. This correlation suggests a denser and more tightly knit structure attributable to the expedited reduction process.

5.2.1.1 FT-IR analysis

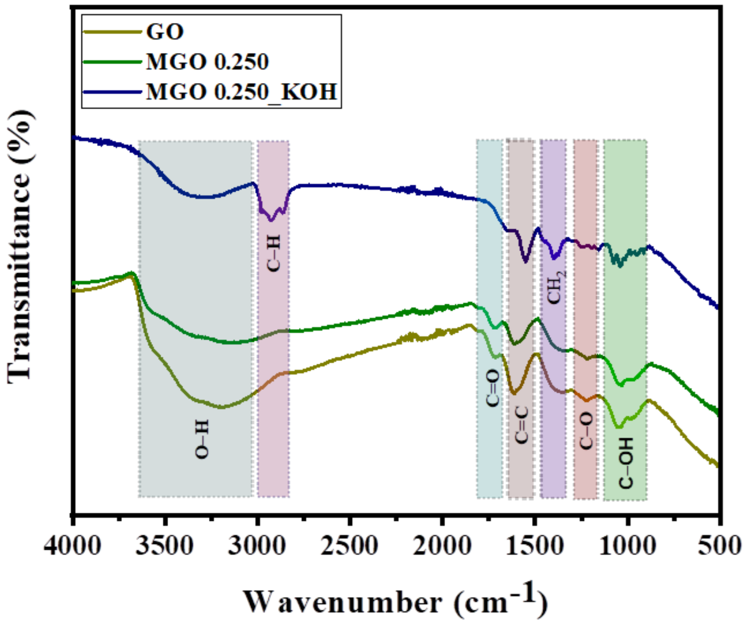

Figure 5.2 FT-IR spectra of GO, MGOs, MGO 0.250_KOH.

The FTIR spectra of the GO, MGO 0.250, and MGO 0.250_KOH samples are depicted in Figure 5.2. These spectra unveil distinct functionalities present on the surface of each material. Notably, the discernible transmission peaks directly correspond to specific vibrations, exhibiting characteristic positions around 3225 (3050 to 2875), 1730, 1450, 1250, 1050, and 1630 cm^{-1}, signifying the O–H, C–H, C=O, CH$_2$, epoxide C–O, alcoholic C–O, and un-oxidized aromatic groups, respectively [11,57,131,196,197]. The comparative analysis of these peaks reveals their consistent occurrence across the GO, MGO 0.250, and MGO 0.250_KOH samples, indicative of shared functional groups. However, the C-H peak demonstrates pronounced intensification in the MGO 0.250_KOH sample. This enhanced prominence of C-H groups underscores the role of the KOH reaction in fostering the generation of C-H groups on the surface of MGOs [132,196]. In particular, MGO 0.250_KOH showed intense peaks between 3050 to 2875 cm^{-1}, which were ascribed to the C-H stretching vibration, and the lesser peaks at 1450 cm^{-1}, which were attributed to CH$_2$ [57].

These peaks were not seen in MGO 0.250 and GO. This provided evidence in favor of adding covalently linked adsorbent to MGO 0.250 [196]. Furthermore, the evolution of the epoxide C–O group peak at 1250 cm^{-1} is noteworthy. The KOH treatment induces a reduction in the intensity of this peak, indicating a transformation in the epoxide functionality. The outcome suggests that the MGO 0.250_KOH sample experiences both C–C and C–O bond cleavage [132–135], culminating in the formation of covalent bonds, including newly developed covalently linked structures.

5.2.1.2 XRD analysis

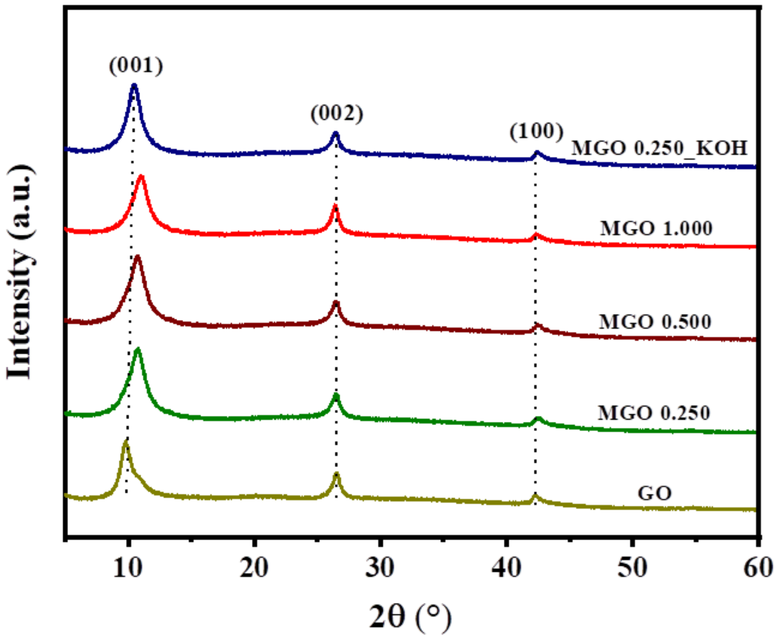

Figure 5.3 XRD patterns of GO, MGOs, MGO 0.250_KOH.

The XRD patterns of GO, MGOs, and activated MGO 0.250_KOH adsorbents are showcased in Figure 5.3. The distinctive crystallographic planes corresponding to diffraction peaks at 10.70°, 26.90°, and 42.75° are attributed to the (001), (002), and (100) crystal planes, respectively [136]. Applying Bragg's equation, the interlayer spacing of MGO is computed at 8.16 Å [137]. A discernible shift in peak intensity is observed following KOH treatment, with a slight augmentation in the peak intensity evident in the MGO 0.250_KOH sample. This phenomenon can be attributed to the heightened presence of oxygen functionalities, as depicted in Figure 5.3. The influence of these oxygen functionalities extends to the interlayer interactions within the MGO structure, consequently impacting the crystalline arrangement of MGO layers. The response to KOH treatment underscores the heightened prominence of surface-bound oxygen functionalities, which, in turn, contributes to the perturbation of the crystalline structure. Notably, the characteristic crystal diffraction peaks corresponding to 10.44°, 10.77°, 10.75°, 10.81°, and 10.45° align with GO, MGO 0.250, MGO 0.500, MGO 1.000, and MGO 0.250_KOH, respectively, further validating the transformation induced by KOH treatment.

5.2.1.3 Raman spectral analysis

Figure 5.4 presents the Raman spectral analysis of GO, MGOs, and MGO 0.250_KOH. The spectral peaks corresponding to the D and G bands appeared at 1300 and 1500 cm^{-1}, respectively. The presence of sp^3 carbon atoms is frequently linked to the D band, which signifies out-of-plane vibrations brought on by structural flaws. In contrast, the G band signifies in-plane vibrations linked to first-order 2g mode scattering, indicative of the presence of sp^2 carbon atoms [131,140,141]. For the MGOs, the near-equal intensities of the D and G bands are indicative of a modest quantity of crystal lattice defects generated through the rigorous oxidation process, characteristic of MGO fabrication [10]. Within the MGO 0.250_KOH sample, a subtle increment in the D band intensity is observed. This elevation can be ascribed to the oxidation influence introduced through the KOH act, amplifying lattice defects and potentially diminishing the crystalline size of sp^2 domains [140,142]. The degree of disorder, encompassing factors like ripples, edges, and flaws, finds representation in the D and G band intensity ratio, commonly denoted as (I_D/I_G) [144]. This intensity ratio, a reflection of the level of disorder, exhibits a slight upward trend across the adsorbents, reaching values of 1.019, 1.045, 1.041, 1.034, and 1.058 for GO, MGO 0.250, MGO 0.500, MGO 1.000, and MGO 0.250_KOH, respectively. This progression highlights the evolving nature of structural disorder within the adsorbents, particularly accentuated by the KOH treatment's oxidative impact on lattice defects and related features.

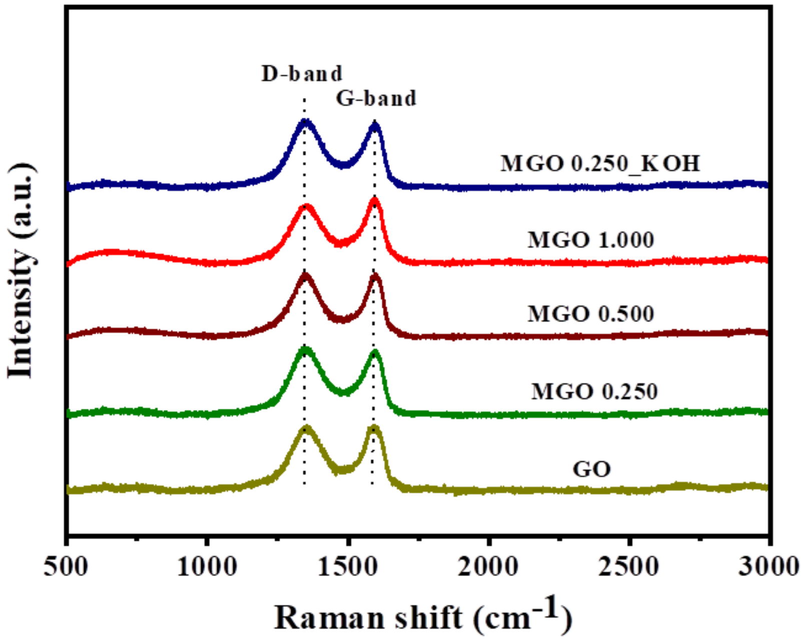

Figure 5.4 Raman spectra GO, MGOs, MGO 0.250_KOH.

5.2.1.4 Surface area and pore volume analysis

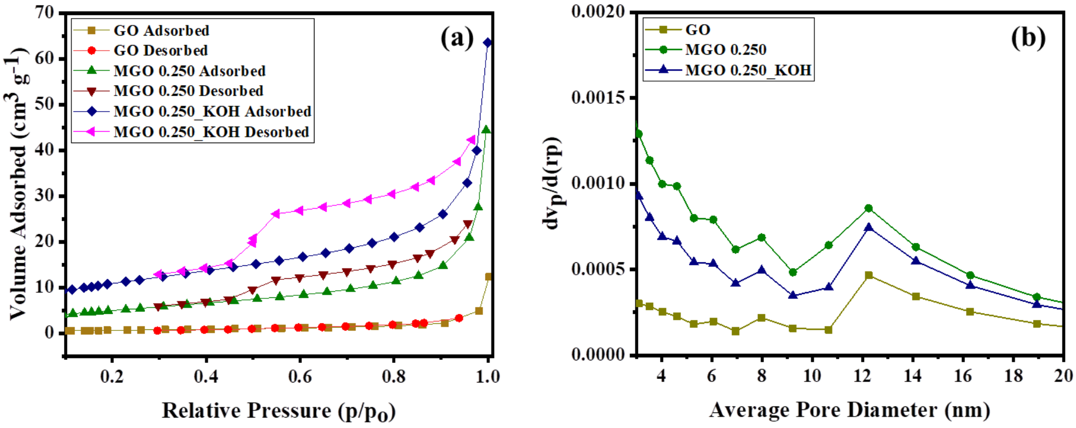

Figure 5.5 (a) N_2 adsorption-desorption isotherm, and (b) pore size distribution curves of GO, MGO 0.250, and MGO 0.250_KOH adsorbents.

BET analysis of N_2 adsorption-desorption isotherm was performed at 77 Kelvin on an automated gas sorption analyzer (Autosorb-IQ, Quntachrome Instruments). For the adsorption measurements, each adsorbent was degassed at 273 Kelvin for six hours. The specific surface area (external and internal surface area) and porosity (%) were calculated by using nitrogen adsorption uptake and relative pressure (p/p_o). The BET surface area achieved from the N_2 adsorption isotherms at 77 Kelvin; the N_2 adsorption-desorption curve is shown in Figure 5.5(a). The type-IV isotherms agree with the existence of the mesoporous nature of the adsorbent, and the average pore diameter lies in the range of 5.0 nm to 20.0 nm. This observation analyzed the specific surface area (SSA) increases with KOH-treated, as shown in Table 5.3. The calculated BET surface areas and total pore volumes of the as-prepared MGO 0.250_KOH were much more significant than those of MGOs. The MGO 0.250_KOH exhibits the most significant BET surface area (419.75 $m^2 g^{-1}$) and total pore volume (1.19 $cm^3 g^{-1}$), which most likely results from the development of more porosity, despite having particular surface areas of our created MGO 0.250_KOH that are significantly less than the 2630 $m^2 g^{-1}$ predicted surface area of a single graphene sheet [145]. However, they still match or exceed those of graphene sponges (418 $m^2 g^{-1}$) [147]. The BJH method's pore size distributions (PSDs) showed that holes with a diameter of less than 20 nm provided the majority of the pore volume, as shown in Figure 5.5(b), with a more apparent PSD in the 4 to 15 nm range, suggesting that all MGOs has small mesopores in the basal plane as shown in Table 5.3. The MGOs precursor volume was raised, and the SSA and total pore volume significantly increased, resulting in a more compacted structure for MGO 0.250_KOH. However, the PSD shift maximum from 3.22 nm for MGO 0.250 to 3.55 nm for MGO 0.250_KOH shows increased oxygen functionality levels, producing MGOs with larger holes. This result is likewise compatible with alterations in the I_D/I_G ratio of the adsorbents, and the MGO 0.250 can conveniently be used to change the concurrent porosity with KOH treatment of the samples.

Table 5.3 BET data of GO, MGOs, and MGO 0.250_KOH adsorbents.

Adsorbent	**SSA (m^2 g^{-1})**	**V_{total} (meso+micro) (cm^3 g^{-1})**	**V_t (meso) (cm^3 g^{-1})**	**Average pore diameter (nm)**	**Meso pore (%)**
GO	278.51	0.64	0.36	5 to 20	56.25
MGO 1.000	287.93	0.68	0.40	5 to 20	58.82
MGO 0.500	296.97	0.76	0.46	5 to 20	60.52
MGO 0.250	309.22	0.87	0.55	5 to 20	63.21
MGO 0.250_KOH	419.75	1.19	0.97	5 to 20	81.51

5.2.1.5 SEM and HR-TEM analysis

The porous morphology of the adsorbents was studied by analyzing the effects of low levels of MaA on pore characteristics. Notably, the introduction of a small amount of MaA resulted in more pronounced pores. Furthermore, the KOH treatment of MGO 0.250, specifically in the case of MGO 0.250_KOH adsorbent, led to an enhancement in surface roughness. This can be observed in the SEM and the HR-TEM images revealed in Figure 5.6. These images reveal the presence of morphological disorders, such as thin sheets, ripples, wrinkles, and related structures within the monoliths. It is worth noting that 2D porous graphene has the ability to self-assemble efficiently into a 3D hierarchical porous graphene structure through hydrophobic and π-π interactions [149,150]. The significant hydrophobicity observed in the MGO 0.250_KOH adsorbent can be attributed to the surface roughness generated by the unique morphology. As depicted in Figure 5.6, the SEM images confirm an increase in surface roughness after KOH-treatment. Additionally, SEM images in Figure 5.6 rather demonstrate the graphene platelets stacking than the creation of porous structures. This sentence suggests the implication of carbon and oxygen in pore enhancement and the resulting changes in the morphological appearance of the graphene layers [179]. Overall, these findings highlight the impact on the porous morphology and surface characteristics of the adsorbents, providing insights into their potential applications in several fields.

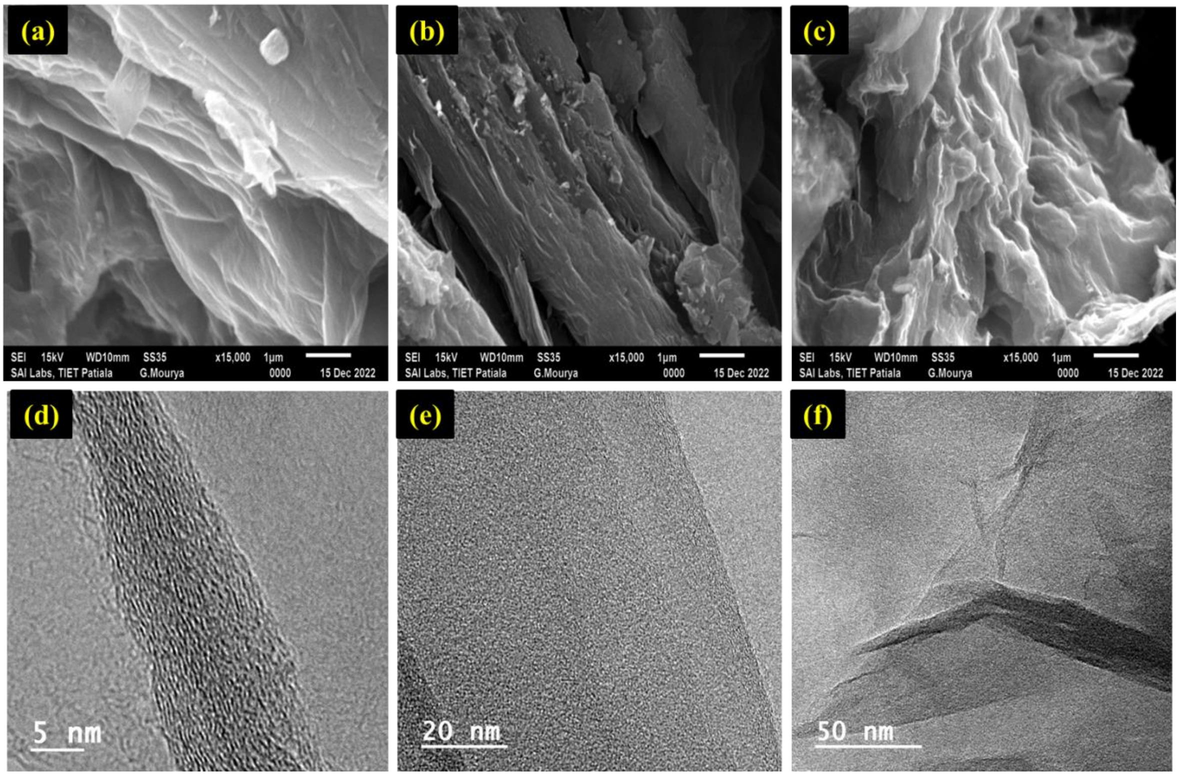

Figure 5.6 SEM images of (a) GO**,** (b) MGO 0.250, (c) MGO 0.250_KOH, and HR-TEM image of MGO 0.250_KOH (d to f). Scale bars in Figure (a to c) 1 μm, scale bars in Figure (d to f) 5 nm, 20 nm, and 50 nm, respectively.

5.2.1.6 XPS analysis

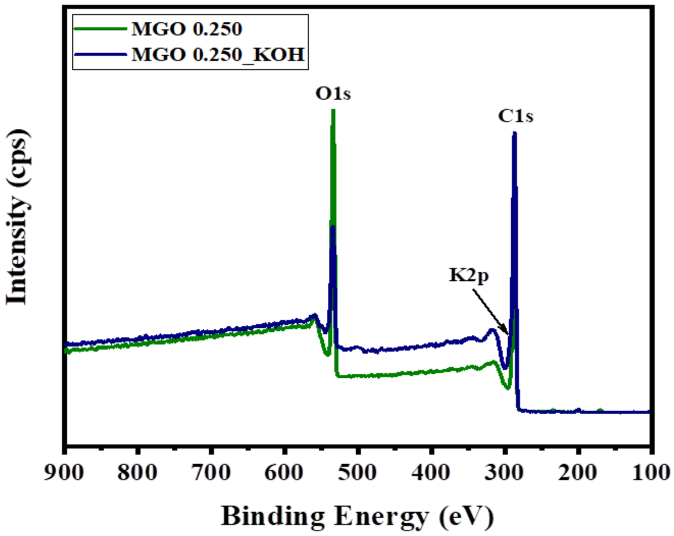

Figure 5.7 XPS survey spectra of MGO 0.250, MGO 0.250_KOH adsorbents.

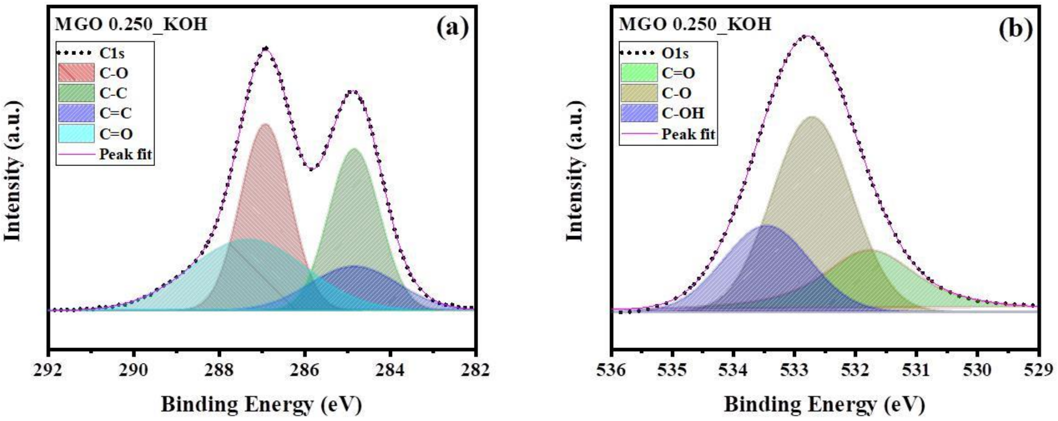

Figure 5.8 XPS spectrum peak of (a) C1s and (b) O1s for MGO 0.250_KOH adsorbent.

The XPS analysis was done to determine the surface functionalities for the synthesized resulting adsorbent. Figure 5.8(a) shows the development of the C1s spectra of KOH-treated adsorbent (MGO 0.250_KOH). The deconvolution of the C1s peak was accomplished using fitting curves with binding energies of about 284.70 eV (C1), 285.13 eV (C2), 286.92 eV (C3), and 287.56 eV (C4) assigned to C=C, C–C, C–OH/C–O, and C=O/COOH are respectively [180–183]. The chemical shifts at the wear track surface shown in Table 5.4, as seen from the matching contributions of the deconvoluted sp^2/sp^3 carbon atoms in the C1s peak, the carbon contribution's graphitization nature changed. Whereas some oxygen groups were lost during KOH treatment, increasing the C/O ratio of approximately 1.99 for the MGO 0.250_KOH, as shown in Figure 5.7. The binding energies in the deconvolution of the O1s peak represent different surface-based oxygen functionalities, as revealed in Figure 5.8(b). The peak represents C=O groups with BE at 531.65 eV (O1). In comparison, the peak represents C–O with BE at 532.70 eV (O2) and C–OH/O=C–OH at 533.45 eV (O3), respectively [181–183]. The chemical shifts at the wear track surface and O1 and O2 in the MGO 0.250_KOH adsorbent have the highest relative area percentage, as shown in Table 5.4; this implies the basic nature of its surface as compared to others [184].

According to studies, each of the functionalities stated above significantly improves samples' basicity and makes them more effective in adsorbing CO_2 [185].

Table 5.4 XPS data for the MGO 0.250_KOH adsorbent.

Sample		C1	C2	C3	C4	O1	O2	O3
MGO 0.250_KOH	BE (eV)	284.70	285.13	286.92	287.56	531.65	532.70	533.45
	FWHM (eV)	1.49	2.53	1.22	2.91	2.33	1.65	2.10
	Area %	30.63	25.01	15.41	28.95	35.11	39.75	25.14

5.2.2 CO_2 capture mechanism

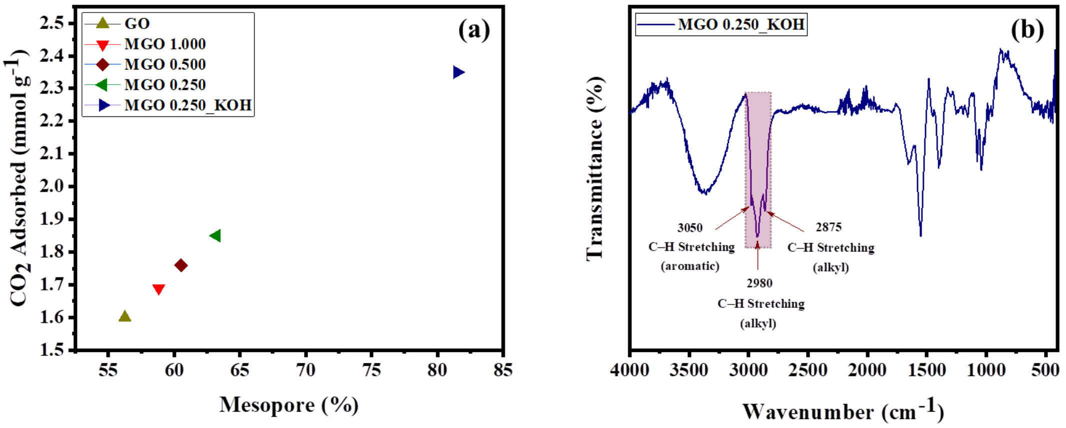

Figure 5.9 (a) Relation between CO_2 adsorption capacity with mesopore % of different adsorbents, and (b) FT-IR spectrum of MGO 0.250_KOH adsorbent.

CO_2 capture relies heavily on the physicochemical attributes of the adsorbent material. Pore size and structure play a vital role, as they dictate the availability of sites for productive interactions during the CO_2 capture process. Moreover, a surplus of pores, coupled with a substantial surface area, is essential for achieving a high degree of CO_2 adsorption efficiency. The interrelation between porosity and CO_2 adsorption efficacy is evident from the influence of porosity on the performance of CO_2 capture. As demonstrated in Figure 5.9(a), there is a noticeable augmentation in the proportion of mesopores, which corresponds to an enhancement in CO_2 capture efficiency. This rise in CO_2 adsorption capacity is predominantly attributed to the escalating mesoporous content within the range of 58.82% to 81.51%. To precisely determine the optimal range of mesopore percentage for efficient CO_2 adsorption and to establish the connection between CO_2 capacity and the different samples—namely, GO, MGOs, and MGO 0.250_KOH—the results are summarized in Table 5.3 and graphically represented in Figure 5.9(a).

To delve deeper into the intricacies of the CO_2 adsorption mechanism, we conducted Fourier-transform infrared (FT-IR) spectroscopy analysis on the MGO 0.250_KOH adsorbent. This analysis enabled the identification of specific covalent-linkage peaks associated with adsorption, as illustrated in Figure 5.9(b). Specifically, MGO 0.250_KOH showed the intense peaks between 3050 to 2875 cm^{-1}, which were ascribed to the C-H stretching vibration, and the lesser peaks at 1450 cm^{-1}, which were attributed to CH_2 [57,58,97,194–196] These peaks were not seen in MGO 0.250 and GO. This provided evidence in favor of adding covalently linked adsorbent to MGO 0.250. Furthermore, for C-H bond, carbon, and hydrogen have electro-negativities of 2.5 and 2.1, respectively; as a result, there are 0.4 electronegativity differences between carbon and hydrogen. The electronegativity difference is smaller than 1.8, indicating that the C-H bond is covalent. We have also calculated the value of $\Delta H°$ (bond energies) during this reaction from thermodynamic parameters. The $\Delta H°$ value of +13.115 kJ mol^{-1} shows the process is endothermic. To unravel the nuances within this spectral range, we present the results visually in Figure 5.9(b). These discoveries lend robust support to the notion that two-dimensional porous graphene exhibits adeptness in self-assembling into a three-dimensional hierarchical porous graphene framework through the synergistic interplay of hydrophobic and π-π interactions [149,150].

Moreover, we assessed the wetting characteristics of MGO 0.250_KOH through water contact angle measurements. A contact angle exceeding 90° is indicative of poor wetting, whereas a slight contact angle below 90° suggests enhanced surface wetting [178]. During the reduction of graphene oxide (GO) to graphene, the resulting graphene nanosheets formed dense structures at interfaces, owing to their shorter inter-sheet distances and stronger π-π interactions [198]. This observation is corroborated by the SEM/HR-TEM images, thoughtfully presented in Figure 5.6. This phenomenon could be ascribed to the presence of KOH molecules that served as chemical pillars during the formation of MGO 0.250_KOH, culminating in an expanded surface area and elevated adsorption capacity, as succinctly summarized in Table 5.3 and Table 5.5.

5.3 CO_2 capture performance

5.3.1 CO_2 adsorption performance of monolithic materials

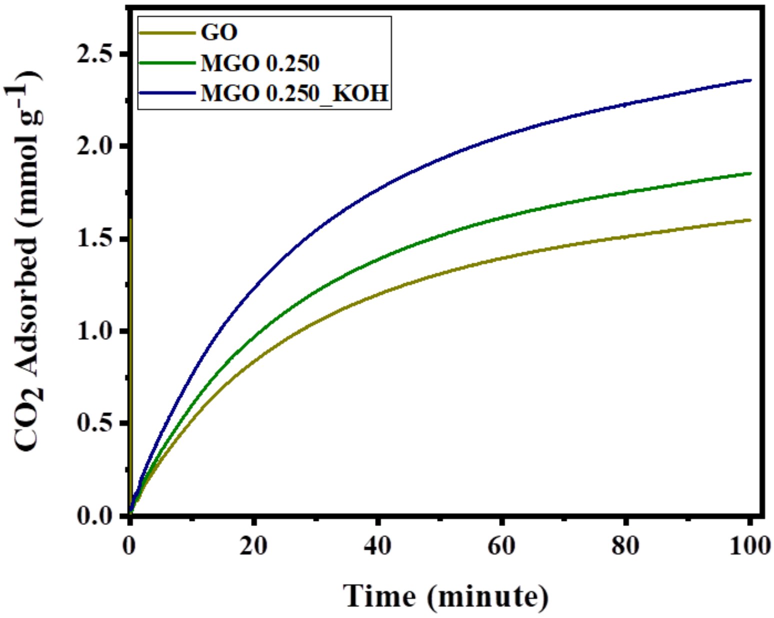

Figure 5.10 CO_2 adsorption performance of GO, MGO 0.250, MGO 0.250_KOH adsorbents at 25 °C.

The CO_2 adsorption capacities of the synthesized and optimized MGOs and MGO 0.250_KOH adsorbents were meticulously evaluated, as illustrated in Figure 5.10. The precise CO_2 adsorption values can be found in Table 5.5. It is evident that, in the initial stages, the CO_2 adsorption capacity reaches its zenith for the MGO 0.250_KOH adsorbent. This specific variant exhibits narrow slit pores, resulting in an approximate CO_2 adsorption capacity of around 2.35 mmol g^{-1}, which is approximately 1.4 times higher than the approximately 1.69 mmol g^{-1} observed for the MGOs. Notably, the fissures generated by the layer-by-layer self-assembly of graphene during thermal annealing likely contribute to a portion of the CO_2 adsorption on MGOs. Furthermore, at a pressure of 1 bar, all the MGOs exhibit a marked upswing in adsorption capacity. The diminutive mesopores facilitate more efficient CO_2 diffusion, while the interconnected platelet structure provides sufficient space to mitigate steric hindrance effects [186]. Consequently, access to all pores within the MGOs becomes viable. Additionally, the isotherm across the pressure range under scrutiny does not display an evident plateau, implying that the samples possess the capacity to adsorb a higher quantity of CO_2 at elevated pressures. At a temperature of 25 °C and a pressure of 1 bar, the equilibrium CO_2 absorption follows this ascending sequence: MGO 1.000 (1.69 mmol g^{-1}) < MGO 0.500 (1.76 mmol g^{-1}) < MGO 0.250 (1.85 mmol g^{-1}) < MGO 0.250_KOH (2.35 mmol g^{-1}). This order can be attributed to MGO 0.250_KOH having the smallest mesopore size among the samples, resulting in the largest BET surface area and total pore volume, thus contributing to its superior CO_2 capture performance. This aligns with existing literature elucidating the influence of smaller pores on low-pressure CO_2 adsorption [102,151].

Furthermore, as outlined in Table 5.6, the CO_2 adsorption capacity of MGO 0.250_KOH proves comparable to that of various other graphene-based materials and carbonaceous counterparts under identical temperature conditions. Notably, this CO_2 adsorption capacity, although comparable, surpasses values reported for other materials. For instance, at 30 °C, the obtained CO_2 adsorption capacity for 3D graphene stands at ca. 1.71 mmol g^{-1} [152], while HGF-Ⅱ records approximately 1.40 mmol g^{-1} at 25 °C [59], and PAN-KOH measures about 1.20 mmol g^{-1} at 25 °C [51]. Among activated carbons at 25 °C, the most recent published value is approximately 0.55 mmol g^{-1} [154]. It is worth noting that various researchers employ diverse activation techniques to enhance the adsorbents' CO_2 adsorption potential, and among these, KOH stands out as an excellent activation agent for enhancing porosity characteristics and adsorption capacities. When compared to findings from other studies, the activated adsorbents developed in our current research exhibit superior adsorption capabilities. This outcome lends support to the notion that MGO 0.250_KOH holds promise for the capture of CO_2 emissions from coal-fired power plants. The significant advantage lies in its capacity for complete and efficient regeneration, allowing for a substantial amount of adsorbed CO_2 to be effectively reclaimed for future sequestration or beneficial utilization.

Table 5.5 The CO_2 adsorption capacity of GO, MGOs, and MGO 0.250_KOH adsorbents at 25 °C.

Adsorbents	**Ads. Time (min)**	**Adsorption Temperature (^oC)**	**CO_2 conc. (%)**	**Adsorption capacity (mmol g^{-1})**
GO	100	25	100	1.60
MGO 1.000	100	25	100	1.69
MGO 0.500	100	25	100	1.76
MGO 0.250	100	25	100	1.85
MGO 0.250_KOH	100	25	100	2.35
MGO 0.250_KOH	100	25	50	1.30

Table 5.6 Comparison table of CO_2 adsorption performance of MGO 0.250_KOH and other adsorbents.

Adsorbent	**Activation method**	**Experimental conditions**		**CO_2 Adsorbed (mmol g^{-1})**	**Ref.**
		CO_2 conc. (%)	**Temp. (°C)**		
MGO 0.250_KOH*	Chemical/KOH (90 °C)	100	25	2.35	Present study
MGO 0.250*	Chemical/KOH (90 °C)	100	25	1.85	Present study
3D graphene	Chemical/NaOH (500 °C)	50	25	1.71	[152]
HPGC-850	Chemical/ (850 °C)	100	0	1.76	[187]
PAN-KOH	Chemical/KOH (800 °C)	12.5	30	1.20	[51]
Carbon monolith	Chemical/KOH (25 °C)	15	30	0.66	[156]
CNTs	Chemical/$SOCl_2$/NH_4OH (350 °C)	60	27	1.58	[153]
EDA	Chemical/COOH (85 °C)	100	25	2.00	[157]
M90_0.5	Chemical/C_6H8O_6 (90 °C)	100	25	2.10	[13]
N-containing resin	Chemical/K_2CO_3 (700 °C)	100	25	1.90	[188]
HGF-II	Chemical/HNO_3 (500 °C)	100	25	1.40	[59]
0.8-DETA/SH-18	Chemical/HCl (108 °C)	100	35	1.65	[199]

5.3.2 Regeneration study

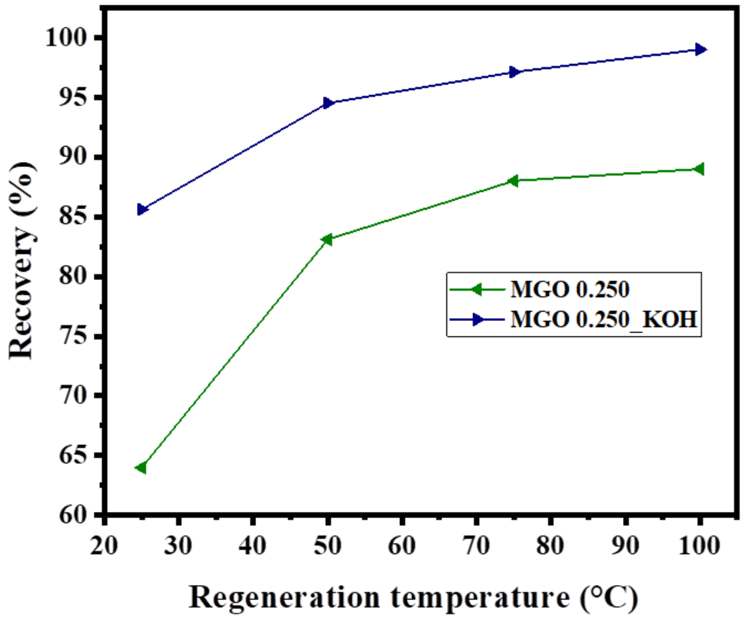

Figure 5.11 Regeneration of MGO 0.250, MGO 0.250_KOH adsorbents.

A comprehensive regeneration investigation was undertaken on the activated adsorbents across a range of temperatures (25 °C, 50 °C, 75 °C, and 100 °C), as depicted in Figure 5.11. Notably, the KOH treatment proved instrumental in augmenting the CO_2 recovery (%) of the activated adsorbents, a trend consistently observed at varying temperatures, as detailed in Table 5.7. At 100 °C, the regeneration process yielded impressive recovery rates of 89.18% for MGO 0.250 and a remarkable 98.80% for MGO 0.250_KOH. With the elevation of the regeneration temperature, there was an instantaneous augmentation in the proportion of CO_2 recovery %. Consequently, the MGO 0.250_KOH adsorbents exhibited near-complete reversibility at 100 °C, manifesting in remarkable recoveries of 98.80%, as comprehensively tabulated in Table 5.7. The regenerative efficacy demonstrated by the MGO 0.250 and MGO 0.250_KOH adsorbents can be attributed to the dynamic alteration of the reaction potential that correlates with the graphitic surface's interaction with CO_2 [19]. Drawing insights from the XRD data elaborated earlier, the heightened multilayer dissociation within the MGO 0.250_KOH adsorbent is anticipated to enhance desorption by effectively releasing CO_2 trapped within the multilayer galleries of MGOs, acting in accordance with the insights gleaned from active sites in this context.

Table 5.7 Adsorption-desorption cycle of MGO 0.250 and MGO 0.250_KOH adsorbents.

Adsorbent	**CO_2 Adsorbed (mmol g^{-1}) at 25 °C**	**CO_2 Desorbed (mmol g^{-1})**				**Recovery percentage (%) of Adsorbed CO_2**			
		25 °C	50 °C	75 °C	100 °C	25 °C	50 °C	75 °C	100 °C
MGO 0.250	1.85	1.18	1.54	1.63	1.65	63.78	83.24	88.10	89.18
MGO 0.250_KOH	2.35	2.01	2.23	2.29	2.32	85.55	94.89	97.44	98.80

5.3.3 Selectivity

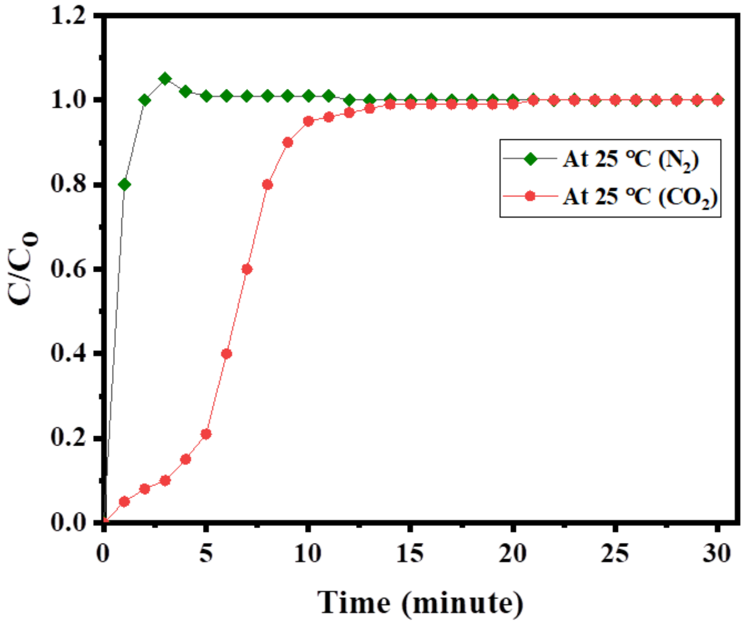

Figure 5.12 CO_2/N_2 selectivity curve.

The selectivity experiments focusing on CO_2/N_2 were executed at 25 °C, 1 bar pressure and CO_2/N_2 binary gas mixture with 50 % CO_2 and 50 % N_2 concentration flow using meticulously prepared adsorbents, with a specific emphasis on investigating the influence of KOH-treated adsorbent's performance. Figure 5.12 visually portrays the outcomes achieved with the adsorbent, revealing a noteworthy reduction in N_2 adsorption capacity. Simultaneously, there's an upsurge in CO_2 uptake, contributing to an augmented CO_2/N_2 selectivity of MGO 0.250_KOH, which is approximately 2.11 times higher than that of MGO 0.250 at 1 bar. These outcomes are expounded upon in Table 5.8, wherein selectivity values of 18.50 and 39.16 were achieved at 1 bar for MGO 0.250 and MGO 0.250_KOH, respectively. The heightened selectivity arises from the notably greater polarizability and quadrupole moment of CO_2 compared to N_2. The results underscore a distinct disparity in adsorption capacity between N_2 and CO_2. This signifies substantial advancement compared to MGO 0.250, which attained a selectivity value of 18.50. In consideration of the diverse industrial emission sources, the applicability of these adsorbents for CO_2 capture under 1 bar pressure conditions bears remarkable technological significance. The findings from this study collectively advocate that the MGO 0.250_KOH adsorbent emerges as a compelling option for proficient CO_2 recovery from flue gases discharged by coal-fired power plants. This conclusion finds resonance in previous research [24,51,59,114] and substantiates the viability of MGO 0.250_KOH in this crucial domain.

Table 5.8 CO_2/N_2 adsorption selectivity on MGO 0.250 and MGO 0.250_KOH adsorbents at 25 °C.

Adsorbent	**CO_2 Adsorbed (mmol g^{-1})**	**N_2 Adsorbed (mmol g^{-1})**	**CO_2/N_2 Selectivity**
	1 bar	**1 bar**	**1 bar**
MGO 0.250	1.85	0.10	18.50
MGO 0.250_KOH	2.35	0.06	39.16

5.3.4 Breakthrough curves

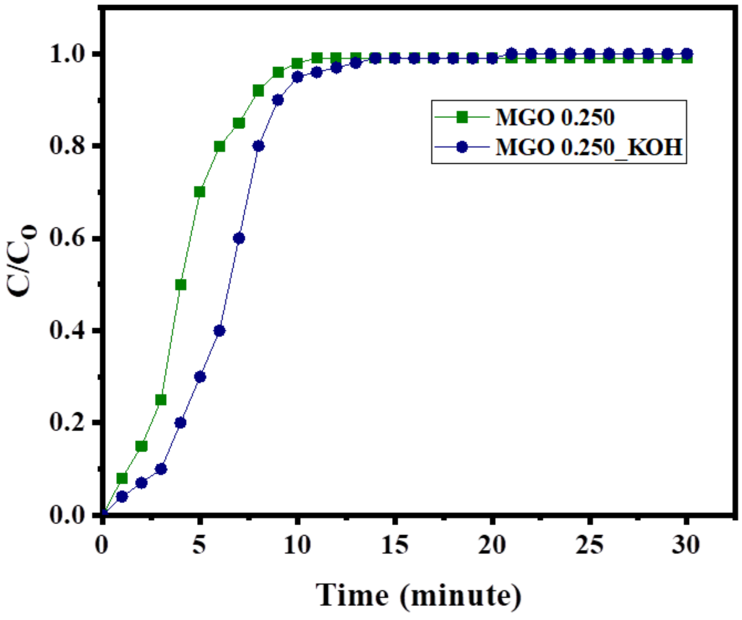

Figure 5.13 Breakthrough curve of MGO 0.250 and MGO 0.250_KOH adsorbents.

The breakthrough curves for the MGO 0.250 and MGO 0.250_KOH samples are revealed in Figure 5.13, which assess the dynamic CO_2 adsorption capacity of ca. 1.0 mmol g^{-1} at 25 °C, 1 bar pressure, and CO_2/N_2 binary gas mixture with 50 % CO_2 and 50 % N_2 concentration flows. It was noted that N_2 was instantly identified, whereas CO_2 began to emerge in the effluent after some time. This shows that N_2 has a lower adsorption capability than CO_2. Initial values of C/C_o for $N_2 > 1$ indicate that N_2 initially occupies the adsorbent's active sites, but with time, N_2 is gradually replaced by CO_2, revealing that the adsorbent has a higher affinity for CO_2 [51,114]. These findings support the incorporation of exceptionally active CO_2-philic chemical groups onto the MGO 0.250_KOH adsorbent through covalent linkage. Hence, MGO 0.250_KOH has more potential to adsorb CO_2 than N_2.

5.4 Conclusions

In this study, we have synthesized monolithic adsorbents based on reduced graphene oxide with varying mass ratios of GO/MaA (1:0.250, 1:0.500, and 1:1 by weight). Additionally, the initially synthesized MGO 0.250 was subjected to KOH-treated adsorbent, leading to the formation of the resultant sample (MGO 0.250_KOH), which was subsequently assessed for its CO_2 capture capabilities. The pivotal findings of our investigation demonstrated that the MGO 0.250_KOH adsorbent exhibited an exceptional CO_2 capture performance, reaching a remarkable 2.35 mmol g^{-1}, attributable to its significantly augmented BET surface area of 419.75 m^2 g^{-1}. This performance enhancement was ascribed to a complex interplay of factors, including morphology, functionality, surface area, and crystal structure. Notably, the best-performing adsorbents, namely MGO 0.250_KOH, showcased superior porosity, inherent basicity, and distinct crystal/structural defects, which collectively contributed to their enhanced CO_2 capture capabilities. Further validation of these findings was attained through regeneration studies conducted at 100 °C. The observed improvement in the recovery percentage of adsorbed CO_2, transitioning from 89.18% for MGO 0.250 to an impressive 98.80% for MGO 0.250_KOH, underscored the efficient desorption dynamics and stable adsorption capacity exhibited by the latter throughout multiple adsorption-desorption cycles. This strategic enhancement holds significant potential for practical implementation within the industrial sector, particularly in scenarios involving low CO_2 partial pressures. These adsorbents offer a combination of attributes, including outstanding CO_2 capture capacities, production yield, mechanism elucidation, selectivity, regenerability, and more, positioning them as a viable and cost-effective pretreatment method for large-scale CO_2 capture prior to employing CCS technology.

Chapter 6 – Conclusions and Recommendations

6.1. Conclusions

In this research project, we have synthesized monolithic graphene oxide-based adsorbents through the self-assembly process of graphene oxide with OxA, and MaA with varying weight ratios and observed CO_2 adsorption performance. To enhance CO_2 capture performance concluded by physical and chemical activation [105]. The CO_2 capture performance depends upon various factors, i.e., morphology, surface area, and crystal structure, that were examined by SEM, FE-SEM, HR-TEM, XPS, BET, XRD, Raman, and FTIR analysis. We have investigated the various kinetic and isotherm models [165,190]. We have also examined various thermodynamic parameters and Q_{st}. Significantly, the monolithic graphene oxide-based adsorbents showed excellent dynamic CO_2 capture capacity (> 1 mmol g^{-1}). The adsorbents possess remarkable CO_2 capture capacities, selectivity, and regenerability, making them highly advantageous as a cost-effective pretreatment method for the CO_2 capture capacity of graphene oxide-based adsorbents was increased using a most straightforward treatment (physical and chemical), which has the potential to be simple to apply in the industrial sector at low CO_2 partial pressure. We ultimately concluded that the chemical activation process through carbonization stands out as the most effective method for implementing CO_2 capture using monolithic graphene oxide-based adsorbents. This preference is attributed to its superior characteristics, including the largest surface area, regenerability, selectivity, and numerous other advantages.

6.2. Recommendations

- To gain a thorough comprehension of the adoption process, It is crucial to assess the impact of various contaminants, such as SO_x and NO_x, affect the CO_2 capture capability.

- The monolithic materials exhibit exceptional reusability and favorable optical properties, rendering them well-suited for the effective treatment of real wastewater.
- Moreover, their application can be extended to encompass CO_2 utilization applications.

References

[1] S.D. Kenarsari, D. Yang, G. Jiang, S. Zhang, J. Wang, A.G. Russell, Q. Wei, M. Fan, Review of recent advances in carbon dioxide separation and capture, RSC Adv. 3 (2013) 22739. https://doi.org/10.1039/c3ra43965h.

[2] H. An, B. Feng, S. Su, Effect of monolithic structure on CO2 adsorption performance of activated carbon fiber–phenolic resin composite: A simulation study, Fuel. 103 (2013) 80–86. https://doi.org/10.1016/j.fuel.2011.06.076.

[3] D.P.V. S, L. Giraldo, J.C. Moreno-Piraján, CO2 adsorption on granular and monolith carbonaceous materials, J. Anal. Appl. Pyrolysis. 96 (2012) 146–152. https://doi.org/10.1016/j.jaap.2012.03.016.

[4] M. Nandi, K. Okada, A. Dutta, A. Bhaumik, J. Maruyama, D. Derks, H. Uyama, Unprecedented CO2 uptake over highly porous N-doped activated carbon monoliths prepared by physical activation, Chem. Commun. 48 (2012) 10283. https://doi.org/10.1039/c2cc35334b.

[5] X. Ma, Y. Li, M. Cao, C. Hu, A novel activating strategy to achieve highly porous carbon monoliths for CO 2 capture, J. Mater. Chem. A. 2 (2014) 4819–4826. https://doi.org/10.1039/C3TA14684G.

[6] S.S. Samsudin, M.S. Abdul Majid, M.R. Mohd Jamir, A.F. Osman, M. Jaafar, H.A. Alshahrani, Physical, Thermal Transport, and Compressive Properties of Epoxy Composite Filled with Graphitic- and Ceramic-Based Thermally Conductive Nanofillers, Polymers (Basel). 14 (2022) 1014.

https://doi.org/10.3390/polym14051014.

[7] K.S. Novoselov, A.K. Geim, S. V. Morozov, D. Jiang, Y. Zhang, S. V. Dubonos, I. V. Grigorieva, A.A. Firsov, Electric field in atomically thin carbon films, Science (80-.). 306 (2004) 666–669. https://doi.org/10.1126/science.1102896.

[8] D.R. Dreyer, H.-P. Jia, C.W. Bielawski, Inside Cover: Graphene Oxide: A Convenient Carbocatalyst for Facilitating Oxidation and Hydration Reactions (Angew. Chem. Int. Ed. 38/2010), Angew. Chemie Int. Ed. 49 (2010) 6686–6686. https://doi.org/10.1002/anie.201003238.

[9] V. Tomašić, F. Jović, State-of-the-art in the monolithic catalysts/reactors, Appl. Catal. A Gen. 311 (2006) 112–121. https://doi.org/10.1016/j.apcata.2006.06.013.

[10] J. Pokhrel, N. Bhoria, S. Anastasiou, T. Tsoufis, D. Gournis, G. Romanos, G.N. Karanikolos, CO2 adsorption behavior of amine-functionalized ZIF-8, graphene oxide, and ZIF-8/graphene oxide composites under dry and wet conditions, Microporous Mesoporous Mater. 267 (2018) 53–67. https://doi.org/10.1016/j.micromeso.2018.03.012.

[11] A. Huang, B. Feng, Facile synthesis of PEI-GO@ZIF-8 hybrid material for CO2 capture, Int. J. Hydrogen Energy. 43 (2018) 2224–2231. https://doi.org/10.1016/j.ijhydene.2017.12.070.

[12] G. Srinivas, J. Burress, T. Yildirim, Graphene oxide derived carbons (GODCs): synthesis and gas adsorption properties, Energy Environ. Sci. 5 (2012) 6453. https://doi.org/10.1039/c2ee21100a.

[13] N. Politakos, I. Barbarin, L.S. Cantador, J.A. Cecilia, E. Mehravar, R. Tomovska, Graphene-Based Monolithic Nanostructures for CO 2 Capture, Ind. Eng. Chem. Res. 59 (2020) 8612–8621. https://doi.org/10.1021/acs.iecr.9b06998.

[14] R. Kumar Jha, H. Bhunia, S. Basu, UV activated monolithic graphene Oxide-Based

adsorbents for dynamic CO2 Capture: Kinetic, isotherm and thermodynamic studies, Chem. Eng. Sci. 285 (2024) 119572. https://doi.org/10.1016/j.ces.2023.119572.

[15] K. Krishnamoorthy, M. Veerapandian, K. Yun, S.-J. Kim, The chemical and structural analysis of graphene oxide with different degrees of oxidation, Carbon N. Y. 53 (2013) 38–49. https://doi.org/10.1016/j.carbon.2012.10.013.

[16] A.M. Varghese, V.M. Rangaraj, S.C. Mun, C.W. Macosko, V. Mittal, Effect of Graphene on Polypropylene/Maleic Anhydride- graft -Ethylene–Vinyl Acetate (PP/EVA- g -MA) Blend: Mechanical, Thermal, Morphological, and Rheological Properties, Ind. Eng. Chem. Res. 57 (2018) 7834–7845. https://doi.org/10.1021/acs.iecr.7b04932.

[17] J. Qin, F. Qiu, X. Rong, H. Zhao, D. Yang, J. Wan, Preparation of graphite oxide/polyurethane foam material and its removal application of malachite green from aqueous solution, J. Appl. Polym. Sci. 131 (2014). https://doi.org/10.1002/app.40988.

[18] A.A. Olajire, Recent advances in the synthesis of covalent organic frameworks for CO2 capture, J. CO2 Util. 17 (2017) 137–161. https://doi.org/10.1016/j.jcou.2016.12.003.

[19] P.M. Sudeep, T.N. Narayanan, A. Ganesan, M.M. Shaijumon, H. Yang, S. Ozden, P.K. Patra, M. Pasquali, R. Vajtai, S. Ganguli, A.K. Roy, M.R. Anantharaman, P.M. Ajayan, Covalently Interconnected Three-Dimensional Graphene Oxide Solids, ACS Nano. 7 (2013) 7034–7040. https://doi.org/10.1021/nn402272u.

[20] Z.-Y. Sui, Y. Cui, J.-H. Zhu, B.-H. Han, Preparation of Three-Dimensional Graphene Oxide–Polyethylenimine Porous Materials as Dye and Gas Adsorbents, ACS Appl. Mater. Interfaces. 5 (2013) 9172–9179. https://doi.org/10.1021/am402661t.

[21] S. Jayanthi, N. KrishnaRao Eswar, S.A. Singh, K. Chatterjee, G. Madras, A.K. Sood, Macroporous three-dimensional graphene oxide foams for dye adsorption and

antibacterial applications, RSC Adv. 6 (2016) 1231–1242. https://doi.org/10.1039/C5RA19925E.

[22] M.Z. Jacobson, Review of solutions to global warming, air pollution, and energy security, Energy Environ. Sci. 2 (2009) 148–173. https://doi.org/10.1039/B809990C.

[23] M.R. Raupach, G. Marland, P. Ciais, C. Le Quéré, J.G. Canadell, G. Klepper, C.B. Field, Global and regional drivers of accelerating CO 2 emissions, Proc. Natl. Acad. Sci. 104 (2007) 10288–10293. https://doi.org/10.1073/pnas.0700609104.

[24] A.M. Varghese, K.S.K. Reddy, S. Singh, G.N. Karanikolos, Performance enhancement of CO2 capture adsorbents by UV treatment: The case of self-supported graphene oxide foam, Chem. Eng. J. 386 (2020) 124022. https://doi.org/10.1016/j.cej.2020.124022.

[25] L.A. Darunte, A.D. Oetomo, K.S. Walton, D.S. Sholl, C.W. Jones, Direct Air Capture of CO 2 Using Amine Functionalized MIL-101(Cr), ACS Sustain. Chem. Eng. 4 (2016) 5761–5768. https://doi.org/10.1021/acssuschemeng.6b01692.

[26] M.K. Mondal, H.K. Balsora, P. Varshney, Progress and trends in CO2 capture/separation technologies: A review, Energy. 46 (2012) 431–441. https://doi.org/10.1016/j.energy.2012.08.006.

[27] S. Suresh, V.C. Srivastava, I.M. Mishra, Isotherm, Thermodynamics, Desorption, and Disposal Study for the Adsorption of Catechol and Resorcinol onto Granular Activated Carbon, J. Chem. Eng. Data. 56 (2011) 811–818. https://doi.org/10.1021/je100303x.

[28] K. Malik, S. Singh, S. Basu, A. Verma, Electrochemical reduction of <scp> CO $_2$ </scp> for synthesis of green fuel, WIREs Energy Environ. 6 (2017). https://doi.org/10.1002/wene.244.

[29] O. Edenhofer, Climate change 2014: mitigation of climate change, Cambridge University Press, 2015.

[30] I.E.A. ETP, IEA Energy Technology Perspectives 2012-Pathways to a Clean Energy System, (2012).

[31] S. Zulfiqar, S. Awan, F. Karadas, M. Atilhan, C.T. Yavuz, M.I. Sarwar, Amidoxime porous polymers for CO2 capture, RSC Adv. 3 (2013) 17203. https://doi.org/10.1039/c3ra42433b.

[32] D.Y.C. Leung, G. Caramanna, M.M. Maroto-Valer, An overview of current status of carbon dioxide capture and storage technologies, Renew. Sustain. Energy Rev. 39 (2014) 426–443. https://doi.org/10.1016/j.rser.2014.07.093.

[33] K.M.K. Yu, I. Curcic, J. Gabriel, S.C.E. Tsang, Recent Advances in CO 2 Capture and Utilization, ChemSusChem. 1 (2008) 893–899. https://doi.org/10.1002/cssc.200800169.

[34] R. Pietrzak, P. Nowicki, J. Kaźmierczak, I. Kuszyńska, J. Goscianska, J. Przepiórski, Comparison of the effects of different chemical activation methods on properties of carbonaceous adsorbents obtained from cherry stones, Chem. Eng. Res. Des. 92 (2014) 1187–1191. https://doi.org/10.1016/j.cherd.2013.10.005.

[35] S.I. Plasynski, J.T. Litynski, H.G. McIlvried, R.D. Srivastava, Progress and New Developments in Carbon Capture and Storage, CRC. Crit. Rev. Plant Sci. 28 (2009) 123–138. https://doi.org/10.1080/07352680902776440.

[36] R. Lal, Sequestering Atmospheric Carbon Dioxide, CRC. Crit. Rev. Plant Sci. 28 (2009) 90–96. https://doi.org/10.1080/07352680902782711.

[37] S.Y. Foong, N.L. Ma, S.S. Lam, W. Peng, F. Low, B.H.K. Lee, A.K.O. Alstrup, C. Sonne, A recent global review of hazardous chlorpyrifos pesticide in fruit and vegetables: Prevalence, remediation and actions needed, J. Hazard. Mater. 400 (2020) 123006. https://doi.org/10.1016/j.jhazmat.2020.123006.

[38] P. Markewitz, W. Kuckshinrichs, W. Leitner, J. Linssen, P. Zapp, R. Bongartz, A.

Schreiber, T.E. Müller, Worldwide innovations in the development of carbon capture technologies and the utilization of CO2, Energy Environ. Sci. 5 (2012) 7281. https://doi.org/10.1039/c2ee03403d.

[39] M. Sharma, R.K. Vyas, K. Singh, A review on reactive adsorption for potential environmental applications, Adsorption. 19 (2013) 161–188.

[40] Q. Chen, F. Rosner, A. Rao, S. Samuelsen, M. Bonnema, A. Jayaraman, G. Alptekin, Simulation of elevated temperature combined water gas shift and solid sorbent CO2 capture for pre-combustion applications using computational fluid dynamics, Appl. Energy. 267 (2020) 114878. https://doi.org/10.1016/j.apenergy.2020.114878.

[41] M. Zhang, Y. Guo, Rate based modeling of absorption and regeneration for CO2 capture by aqueous ammonia solution, Appl. Energy. 111 (2013) 142–152. https://doi.org/10.1016/j.apenergy.2013.04.074.

[42] R. Idem, T. Supap, H. Shi, D. Gelowitz, M. Ball, C. Campbell, P. Tontiwachwuthikul, Practical experience in post-combustion CO2 capture using reactive solvents in large pilot and demonstration plants, Int. J. Greenh. Gas Control. 40 (2015) 6–25. https://doi.org/10.1016/j.ijggc.2015.06.005.

[43] R. Muraleedharan, A. Mondal, B. Mandal, Absorption of carbon dioxide into aqueous blends of 2-amino-2-hydroxymethyl-1,3-propanediol and monoethanolamine, Sep. Purif. Technol. 94 (2012) 92–96. https://doi.org/10.1016/j.seppur.2011.10.035.

[44] A. Veawab, A. Aroonwilas, P. Tontiwachwuthikul, CO2 absorption performance of aqueous alkanolamines in packed columns, Fuel Chem. Div. Prepr. 47 (2002) 49–50.

[45] D. Aaron, C. Tsouris, Separation of CO 2 from Flue Gas: A Review, Sep. Sci. Technol. 40 (2005) 321–348. https://doi.org/10.1081/SS-200042244.

[46] B.E. Gurkan, J.C. De La Fuente, E.M. Mindrup, L.E. Ficke, B.F. Goodrich, E.A. Price, W.F. Schneider, J.F. Brennecke, Equimolar CO2 absorption by anion-functionalized

ionic liquids, J. Am. Chem. Soc. 132 (2010) 2116–2117. https://doi.org/10.1021/ja909305t.

[47] F. Bougie, M.C. Iliuta, CO 2 Absorption in Aqueous Piperazine Solutions: Experimental Study and Modeling, J. Chem. Eng. Data. 56 (2011) 1547–1554. https://doi.org/10.1021/je1012247.

[48] H. Deng, H. Yi, X. Tang, Q. Yu, P. Ning, L. Yang, Adsorption equilibrium for sulfur dioxide, nitric oxide, carbon dioxide, nitrogen on 13X and 5A zeolites, Chem. Eng. J. 188 (2012) 77–85. https://doi.org/10.1016/j.cej.2012.02.026.

[49] J.W. Maina, C. Pozo-Gonzalo, L. Kong, J. Schütz, M. Hill, L.F. Dumée, Metal organic framework based catalysts for CO 2 conversion, Mater. Horizons. 4 (2017) 345–361. https://doi.org/10.1039/C6MH00484A.

[50] R.S. Franchi, P.J.E. Harlick, A. Sayari, Applications of Pore-Expanded Mesoporous Silica. 2. Development of a High-Capacity, Water-Tolerant Adsorbent for CO 2, Ind. Eng. Chem. Res. 44 (2005) 8007–8013. https://doi.org/10.1021/ie0504194.

[51] J. Singh, S. Basu, H. Bhunia, Dynamic CO2 adsorption on activated carbon adsorbents synthesized from polyacrylonitrile (PAN): Kinetic and isotherm studies, Microporous Mesoporous Mater. 280 (2019) 357–366. https://doi.org/10.1016/j.micromeso.2019.02.031.

[52] J. Bai, J. Huang, Q. Yu, M. Demir, M. Kilic, B.N. Altay, X. Hu, L. Wang, N-doped porous carbon derived from macadamia nut shell for CO2 adsorption, Fuel Process. Technol. 249 (2023) 107854. https://doi.org/10.1016/j.fuproc.2023.107854.

[53] J. Bai, J. Huang, Q. Jiang, W. Jiang, M. Demir, M. Kilic, B.N. Altay, L. Wang, X. Hu, Synthesis and characterization of polyphenylene sulfide resin-derived S-doped porous carbons for efficient CO2 capture, Colloids Surfaces A Physicochem. Eng. Asp. 674 (2023) 131916. https://doi.org/10.1016/j.colsurfa.2023.131916.

[54] and J.R.L. Bae, Tae-Hyun, Matthew R. Hudson, Jarad A. Mason, Wendy L. Queen, Justin J. Dutton, Kenji Sumida, Ken J. Micklash, Steven S. Kaye, Craig M. Brown, Energy & Environmental Science 6, Energy Environ. Sci. 6. 1 (2013) 128–138.

[55] S. Dinda, P. Murge, B. Chakravarthy Paruchuri, A study on zeolite-based adsorbents for CO 2 capture, Bull. Mater. Sci. 42 (2019) 240. https://doi.org/10.1007/s12034-019-1936-8.

[56] M.A. de la Casa-Lillo, F. Lamari-Darkrim, D. Cazorla-Amorós, A. Linares-Solano, Hydrogen Storage in Activated Carbons and Activated Carbon Fibers, J. Phys. Chem. B. 106 (2002) 10930–10934. https://doi.org/10.1021/jp014543m.

[57] X. Huang, J. Sun, K. Lv, J. Liu, H. Shen, F. Zhang, Application of core-shell structural acrylic resin/nano-SiO2 composite in water based drilling fluid to plug shale pores, J. Nat. Gas Sci. Eng. 55 (2018) 418–425. https://doi.org/10.1016/j.jngse.2018.05.023.

[58] Z. Fang, Y. Hu, X. Wu, Y. Qin, J. Cheng, Y. Chen, P. Tan, H. Li, A novel magnesium ascorbyl phosphate graphene-based monolith and its superior adsorption capability for bisphenol A, Chem. Eng. J. 334 (2018) 948–956. https://doi.org/10.1016/j.cej.2017.10.067.

[59] S. Chowdhury, R. Balasubramanian, Holey graphene frameworks for highly selective post-combustion carbon capture, Sci. Rep. 6 (2016) 21537. https://doi.org/10.1038/srep21537.

[60] N. Politakos, I. Barbarin, T. Cordero-Lanzac, A. Gonzalez, R. Zangi, R. Tomovska, Reduced graphene oxide/polymer monolithic materials for selective CO2 capture, Polymers (Basel). 12 (2020) 936.

[61] I. Barbarin, N. Politakos, L. Serrano-Cantador, J.A. Cecilia, O. Sanz, R. Tomovska, Towards functionalized graphene/polymer monolithic structures for selective CO2 capture, Microporous Mesoporous Mater. 337 (2022) 111907.

[62] B. Stankovic, I. Barbarin, O. Sanz, R. Tomovska, F. Ruipérez, Experimental and theoretical study of the effect of different functionalities of graphene oxide/polymer composites on selective CO2 capture, Sci. Rep. 12 (2022) 15992.

[63] G.M. Meconi, R. Tomovska, R. Zangi, Adsorption of CO2 gas on graphene–polymer composites, J. CO2 Util. 32 (2019) 92–105.

[64] S.A. Rackley, Carbon capture and storage, Butterworth-Heinemann, 2017.

[65] A. Julbe, M. Drobek, A. Ayral, About the role of adsorption in inorganic and composite membranes, Curr. Opin. Chem. Eng. 24 (2019) 88–97. https://doi.org/10.1016/j.coche.2019.03.007.

[66] J. White, Literature review on adsorption cooling systems, Lat. Am. Caribb. J. Eng. Educ. 378 (2013) 28.

[67] R.T. Yang, Adsorbents: fundamentals and applications, John Wiley & Sons, 2003.

[68] P. Murge, S. Dinda, S. Roy, Zeolite-Based Sorbent for CO 2 Capture: Preparation and Performance Evaluation, Langmuir. 35 (2019) 14751–14760. https://doi.org/10.1021/acs.langmuir.9b02259.

[69] F. Su, C. Lu, S.-C. Kuo, W. Zeng, Adsorption of CO 2 on Amine-Functionalized Y-Type Zeolites, Energy & Fuels. 24 (2010) 1441–1448. https://doi.org/10.1021/ef901077k.

[70] D. Panda, E.A. Kumar, S.K. Singh, Amine Modification of Binder-Containing Zeolite 4A Bodies for Post-Combustion CO 2 Capture, Ind. Eng. Chem. Res. 58 (2019) 5301–5313. https://doi.org/10.1021/acs.iecr.8b03958.

[71] R. Kusumastuti, Sriyono, M. Pancoko, S.L. Butar-Butar, G.E. Putra, H. Tjahjono, Study On The Mechanism of CO 2 Adsorption Process on zeolite 5A as a Molecular Sieve In RDE System: An Infrared Investigation, J. Phys. Conf. Ser. 1198 (2019) 032009. https://doi.org/10.1088/1742-6596/1198/3/032009.

[72] F. Su, C. Lu, CO2 capture from gas stream by zeolite 13X using a dual-column temperature/vacuum swing adsorption, Energy Environ. Sci. 5 (2012) 9021. https://doi.org/10.1039/c2ee22647b.

[73] S. Cavenati, C.A. Grande, A.E. Rodrigues, Adsorption Equilibrium of Methane, Carbon Dioxide, and Nitrogen on Zeolite 13X at High Pressures, J. Chem. Eng. Data. 49 (2004) 1095–1101. https://doi.org/10.1021/je0498917.

[74] S.-Y. Lee, S.-J. Park, A review on solid adsorbents for carbon dioxide capture, J. Ind. Eng. Chem. 23 (2015) 1–11. https://doi.org/10.1016/j.jiec.2014.09.001.

[75] C. Feng, K.C. Khulbe, T. Matsuura, R. Farnood, A.F. Ismail, Recent progress in zeolite/zeotype membranes, J. Membr. Sci. Res. 1 (2015) 49–72.

[76] J. Ci, C. Cao, S. Kuga, J. Shen, M. Wu, Y. Huang, Improved Performance of Microbial Fuel Cell Using Esterified Corncob Cellulose Nanofibers To Fabricate Air-Cathode Gas Diffusion Layer, ACS Sustain. Chem. Eng. 5 (2017) 9614–9618. https://doi.org/10.1021/acssuschemeng.7b01970.

[77] S. Karka, S. Kodukula, S. V. Nandury, U. Pal, Polyethylenimine-Modified Zeolite 13X for CO 2 Capture: Adsorption and Kinetic Studies, ACS Omega. 4 (2019) 16441–16449. https://doi.org/10.1021/acsomega.9b02047.

[78] K. Li, J. Jiang, F. Yan, S. Tian, X. Chen, The influence of polyethyleneimine type and molecular weight on the CO2 capture performance of PEI-nano silica adsorbents, Appl. Energy. 136 (2014) 750–755. https://doi.org/10.1016/j.apenergy.2014.09.057.

[79] X. Xu, C. Song, J.M. Andresen, B.G. Miller, A.W. Scaroni, Novel Polyethylenimine-Modified Mesoporous Molecular Sieve of MCM-41 Type as High-Capacity Adsorbent for CO 2 Capture, Energy & Fuels. 16 (2002) 1463–1469. https://doi.org/10.1021/ef020058u.

[80] X. Xu, C. Song, B.G. Miller, A.W. Scaroni, Adsorption separation of carbon dioxide

from flue gas of natural gas-fired boiler by a novel nanoporous “molecular basket” adsorbent, Fuel Process. Technol. 86 (2005) 1457–1472. https://doi.org/10.1016/j.fuproc.2005.01.002.

[81] X. Xu, C. Song, B.G. Miller, A.W. Scaroni, Influence of Moisture on CO 2 Separation from Gas Mixture by a Nanoporous Adsorbent Based on Polyethylenimine-Modified Molecular Sieve MCM-41, Ind. Eng. Chem. Res. 44 (2005) 8113–8119. https://doi.org/10.1021/ie050382n.

[82] X. Xu, C. Song, J.M. Andresen, B.G. Miller, A.W. Scaroni, Adsorption separation of CO2 from simulated flue gas mixtures by novel CO2 “molecular basket” adsorbents, Int. J. Environ. Technol. Manag. 4 (2004) 32. https://doi.org/10.1504/IJETM.2004.004630.

[83] X. Xu, C. Song, J.M. Andrésen, B.G. Miller, A.W. Scaroni, Preparation and characterization of novel CO2 “molecular basket” adsorbents based on polymer-modified mesoporous molecular sieve MCM-41, Microporous Mesoporous Mater. 62 (2003) 29–45. https://doi.org/10.1016/S1387-1811(03)00388-3.

[84] Y. Belmabkhout, R. Serna-Guerrero, A. Sayari, Adsorption of CO2 from dry gases on MCM-41 silica at ambient temperature and high pressure. 1: Pure CO2 adsorption, Chem. Eng. Sci. 64 (2009) 3721–3728.

[85] Y. Belmabkhout, R. Serna-Guerrero, A. Sayari, Adsorption of CO2-containing gas mixtures over amine-bearing pore-expanded MCM-41 silica: Application for gas purification, Ind. Eng. Chem. Res. 49 (2010) 359–365. https://doi.org/10.1021/ie900837t.

[86] R. Serna-Guerrero, Y. Belmabkhout, A. Sayari, Triamine-grafted pore-expanded mesoporous silica for CO 2 capture: effect of moisture and adsorbent regeneration strategies, Adsorption. 16 (2010) 567–575.

[87] C. Chen, S.-T. Yang, W.-S. Ahn, R. Ryoo, Amine-impregnated silica monolith with a hierarchical pore structure: enhancement of CO2 capture capacity, Chem. Commun. (2009) 3627. https://doi.org/10.1039/b905589d.

[88] W.-J. Son, J.-S. Choi, W.-S. Ahn, Adsorptive removal of carbon dioxide using polyethyleneimine-loaded mesoporous silica materials, Microporous Mesoporous Mater. 113 (2008) 31–40. https://doi.org/10.1016/j.micromeso.2007.10.049.

[89] H. Yan, G. Zhang, J. Liu, G. Li, Y. Wang, Highly efficient CO2 adsorption by imidazole and tetraethylenepentamine functional sorbents: Optimization and analysis using response surface methodology, J. Environ. Chem. Eng. 9 (2021) 105639. https://doi.org/10.1016/j.jece.2021.105639.

[90] M.R. Mello, D. Phanon, G.Q. Silveira, P.L. Llewellyn, C.M. Ronconi, Amine-modified MCM-41 mesoporous silica for carbon dioxide capture, Microporous Mesoporous Mater. 143 (2011) 174–179. https://doi.org/10.1016/j.micromeso.2011.02.022.

[91] J. Liu, Y. Wei, Y. Zhao, Trace Carbon Dioxide Capture by Metal–Organic Frameworks, ACS Sustain. Chem. Eng. 7 (2019) 82–93. https://doi.org/10.1021/acssuschemeng.8b05590.

[92] K. Sladekova, C. Campbell, C. Grant, A.J. Fletcher, J.R.B. Gomes, M. Jorge, The effect of atomic point charges on adsorption isotherms of CO 2 and water in metal organic frameworks, Adsorption. 26 (2020) 663–685.

[93] P. Fageria, S. Gangopadhyay, S. Pande, Synthesis of ZnO/Au and ZnO/Ag nanoparticles and their photocatalytic application using UV and visible light, RSC Adv. 4 (2014) 24962–24972. https://doi.org/10.1039/C4RA03158J.

[94] J. Liu, Y. Wei, P. Li, Y. Zhao, R. Zou, Selective H 2 S/CO 2 Separation by Metal–Organic Frameworks Based on Chemical-Physical Adsorption, J. Phys. Chem. C. 121

(2017) 13249–13255. https://doi.org/10.1021/acs.jpcc.7b04465.

[95] B. Liu, H. Li, X. Ma, R. Chen, S. Wang, L. Li, The synergistic effect of oxygen-containing functional groups on CO 2 adsorption by the glucose–potassium citrate-derived activated carbon, RSC Adv. 8 (2018) 38965–38973. https://doi.org/10.1039/C8RA05523H.

[96] S. Nandi, R. Maity, D. Chakraborty, H. Ballav, R. Vaidhyanathan, Preferential Adsorption of CO 2 in an Ultramicroporous MOF with Cavities Lined by Basic Groups and Open-Metal Sites, Inorg. Chem. 57 (2018) 5267–5272. https://doi.org/10.1021/acs.inorgchem.8b00304.

[97] K. Preet, G. Gupta, M. Kotal, S.K. Kansal, D.B. Salunke, H.K. Sharma, S. Chandra Sahoo, P. Van Der Voort, S. Roy, Mechanochemical Synthesis of a New Triptycene-Based Imine-Linked Covalent Organic Polymer for Degradation of Organic Dye, Cryst. Growth Des. 19 (2019) 2525–2530. https://doi.org/10.1021/acs.cgd.9b00166.

[98] K. Malik, B.M. Rajbongshi, A. Verma, Syngas production from electrochemical reduction of CO2 at high current density using oxide derived Zn/Cu nanocomposite, J. CO2 Util. 33 (2019) 311–319. https://doi.org/10.1016/j.jcou.2019.06.020.

[99] C.P. Cabello, G. Berlier, G. Magnacca, P. Rumori, G.T. Palomino, Enhanced CO 2 adsorption capacity of amine-functionalized MIL-100(Cr) metal–organic frameworks, CrystEngComm. 17 (2015) 430–437. https://doi.org/10.1039/C4CE01265H.

[100] M. Kaur, S.K. Mehta, S.K. Kansal, Amine-functionalized titanium metal-organic framework (NH2-MIL-125(Ti)): A novel fluorescent sensor for the highly selective sensing of copper ions, Mater. Chem. Phys. 254 (2020) 123539. https://doi.org/10.1016/j.matchemphys.2020.123539.

[101] B. Tanhaei, A. Ayati, F.F. Bamoharram, M. Lahtinen, M. Sillanpää, A novel magnetic Preyssler acid grafted chitosan nano adsorbent: synthesis, characterization and

adsorption activity, J. Chem. Technol. Biotechnol. 91 (2016) 1452–1460. https://doi.org/10.1002/jctb.4742.

[102] L. Bastin, P.S. Bárcia, E.J. Hurtado, J.A.C. Silva, A.E. Rodrigues, B. Chen, A Microporous Metal−Organic Framework for Separation of CO 2 /N 2 and CO 2 /CH 4 by Fixed-Bed Adsorption, J. Phys. Chem. C. 112 (2008) 1575–1581. https://doi.org/10.1021/jp077618g.

[103] R. Mohd Firdaus, N. Berrada, A. Desforges, A.R. Mohamed, B. Vigolo, From 2D Graphene Nanosheets to 3D Graphene-based Macrostructures, Chem. – An Asian J. 15 (2020) 2902–2924. https://doi.org/10.1002/asia.202000747.

[104] S. Chowdhury, R. Balasubramanian, From 2D Graphene Nanosheets to 3D Graphene-based Macrostructures, Ind. Eng. Chem. Res. 55 (2016) 7906–7916. https://doi.org/10.1021/acs.iecr.5b04052.

[105] M. Mohammed, R. Rahman, A.M. Mohammed, T. Adam, B.O. Betar, A.F. Osman, O.S. Dahham, Surface treatment to improve water repellence and compatibility of natural fiber with polymer matrix: Recent advancement, Polym. Test. 115 (2022) 107707. https://doi.org/10.1016/j.polymertesting.2022.107707.

[106] Z.-Y. Sui, B.-H. Han, Effect of surface chemistry and textural properties on carbon dioxide uptake in hydrothermally reduced graphene oxide, Carbon N. Y. 82 (2015) 590–598. https://doi.org/10.1016/j.carbon.2014.11.014.

[107] T.J. Bandosz, M. Seredych, E. Rodríguez-Castellón, Y. Cheng, L.L. Daemen, A.J. Ramírez-Cuesta, Evidence for CO2 reactive adsorption on nanoporous S- and N-doped carbon at ambient conditions, Carbon N. Y. 96 (2016) 856–863. https://doi.org/10.1016/j.carbon.2015.10.007.

[108] W. Li, H. Yang, X. Jiang, Q. Liu, Highly selective CO 2 adsorption of ZnO based N-doped reduced graphene oxide porous nanomaterial, Appl. Surf. Sci. 360 (2016) 143–

147. https://doi.org/10.1016/j.apsusc.2015.10.212.

[109] J.M. Ngoy, N. Wagner, L. Riboldi, O. Bolland, A CO2 Capture Technology Using Multi-walled Carbon Nanotubes with Polyaspartamide Surfactant, Energy Procedia. 63 (2014) 2230–2248. https://doi.org/10.1016/j.egypro.2014.11.242.

[110] L. Keller, B. Ohs, J. Lenhart, L. Abduly, P. Blanke, M. Wessling, High capacity polyethylenimine impregnated microtubes made of carbon nanotubes for CO2 capture, Carbon N. Y. 126 (2018) 338–345. https://doi.org/10.1016/j.carbon.2017.10.023.

[111] M. Irani, A.T. Jacobson, K.A.M. Gasem, M. Fan, Modified carbon nanotubes/tetraethylenepentamine for CO2 capture, Fuel. 206 (2017) 10–18. https://doi.org/10.1016/j.fuel.2017.05.087.

[112] H.S. Oliveira, L.M. Araújo, P.C.C. Pinto, G. V Pereira, P.P. de Souza, J.C. Belchior, L.C.A. Oliveira, Improvement on CO 2 capture by CaO pellet modified with carbon nanotubes, Int. Nano Lett. 10 (2020) 141–149.

[113] W.R. Lee, H. Jo, L.M. Yang, H. Lee, D.W. Ryu, K.S. Lim, J.H. Song, D.Y. Min, S.S. Han, J.G. Seo, Y.K. Park, D. Moon, C.S. Hong, Exceptional CO2 working capacity in a heterodiamine-grafted metal-organic framework, Chem. Sci. 6 (2015) 3697–3705. https://doi.org/10.1039/c5sc01191d.

[114] J. Bai, J. Huang, Q. Yu, M. Demir, E. Akgul, B.N. Altay, X. Hu, L. Wang, Fabrication of coconut shell-derived porous carbons for CO2 adsorption application, Front. Chem. Sci. Eng. (2023). https://doi.org/10.1007/s11705-022-2292-6.

[115] A. Karmakar, S. Nagappan, A. Das, A. Kalloorkal, S. Kundu, Exploring the linear relationship between potential dynamics and interfacial capacitance: implications for enhancing the turnover frequency in electrochemical water splitting, J. Mater. Chem. A. 11 (2023) 15635–15642. https://doi.org/10.1039/D3TA02540C.

[116] N. Finčur, D. Šojić Merkulov, P. Putnik, V. Despotović, N. Banić, M. Lazarević, D.

Četojević-Simin, J. Agbaba, B. Abramović, Environmental Photocatalytic Degradation of Antidepressants with Solar Radiation: Kinetics, Mineralization, and Toxicity, Nanomaterials. 11 (2021) 632. https://doi.org/10.3390/nano11030632.

[117] B. Tanhaei, A. Ayati, M. Lahtinen, B. Mahmoodzadeh Vaziri, M. Sillanpää, A magnetic mesoporous chitosan based core-shells biopolymer for anionic dye adsorption: Kinetic and isothermal study and application of <scp>ANN</scp>, J. Appl. Polym. Sci. 133 (2016). https://doi.org/10.1002/app.43466.

[118] C. Goel, H. Bhunia, P.K. Bajpai, Synthesis of nitrogen doped mesoporous carbons for carbon dioxide capture, RSC Adv. 5 (2015) 46568–46582. https://doi.org/10.1039/C5RA05684E.

[119] D. V. Šojić Merkulov, V.N. Despotović, N.D. Banić, S.J. Armaković, N.L. Finčur, M.J. Lazarević, D.D. Četojević-Simin, D.Z. Orčić, M.B. Radoičić, Z. V. Šaponjić, M.I. Čomor, B.F. Abramović, Photocatalytic decomposition of selected biologically active compounds in environmental waters using TiO2/polyaniline nanocomposites: Kinetics, toxicity and intermediates assessment, Environ. Pollut. 239 (2018) 457–465. https://doi.org/10.1016/j.envpol.2018.04.039.

[120] V. Subbaramaiah, V.C. Srivastava, I.D. Mall, Optimization of Reaction Patirameters and Kinetic Modeling of Catalyc Wet Peroxidation of Picoline by Cu/SBA-15, Ind. Eng. Chem. Res. 52 (2013) 9021–9029. https://doi.org/10.1021/ie400124d.

[121] M.A. Hossain, M. Kumita, Y. Michigami, S. Mori, Kinetics of Cr(VI) Adsorption on Used Black Tea Leaves, J. Chem. Eng. JAPAN. 38 (2005) 402–408. https://doi.org/10.1252/jcej.38.402.

[122] Y.. Ho, G. McKay, Pseudo-second order model for sorption processes, Process Biochem. 34 (1999) 451–465. https://doi.org/10.1016/S0032-9592(98)00112-5.

[123] N.A. Rashidi, S. Yusup, B.H. Hameed, Kinetic studies on carbon dioxide capture using

lignocellulosic based activated carbon, Energy. 61 (2013) 440–446. https://doi.org/10.1016/j.energy.2013.08.050.

[124] I. Langmuir, THE CONSTITUTION AND FUNDAMENTAL PROPERTIES OF SOLIDS AND LIQUIDS. PART I. SOLIDS., J. Am. Chem. Soc. 38 (1916) 2221–2295. https://doi.org/10.1021/ja02268a002.

[125] P.B. Vilela, A. Dalalibera, E.C. Duminelli, V.A. Becegato, A.T. Paulino, Adsorption and removal of chromium (VI) contained in aqueous solutions using a chitosan-based hydrogel, Environ. Sci. Pollut. Res. 26 (2019) 28481–28489. https://doi.org/10.1007/s11356-018-3208-3.

[126] A.H. Jawad, A.S. Abdulhameed, Mesoporous Iraqi red kaolin clay as an efficient adsorbent for methylene blue dye: Adsorption kinetic, isotherm and mechanism study, Surfaces and Interfaces. 18 (2020) 100422. https://doi.org/10.1016/j.surfin.2019.100422.

[127] S. Salvestrini, V. Leone, P. Iovino, S. Canzano, S. Capasso, Considerations about the correct evaluation of sorption thermodynamic parameters from equilibrium isotherms, J. Chem. Thermodyn. 68 (2014) 310–316. https://doi.org/10.1016/j.jct.2013.09.013.

[128] B. Guo, L. Chang, K. Xie, Adsorption of Carbon Dioxide on Activated Carbon, J. Nat. Gas Chem. 15 (2006) 223–229. https://doi.org/10.1016/S1003-9953(06)60030-3.

[129] W.S. Hummers, R.E. Offeman, Preparation of Graphitic Oxide, J. Am. Chem. Soc. 80 (1958) 1339–1339. https://doi.org/10.1021/ja01539a017.

[130] J. Zhang, H. Yang, G. Shen, P. Cheng, J. Zhang, S. Guo, Reduction of graphene oxide via <scp>l</scp> -ascorbic acid, Chem. Commun. 46 (2010) 1112–1114. https://doi.org/10.1039/B917705A.

[131] A. Subrati, S. Mondal, M. Ali, A. Alhindi, R. Ghazi, A. Abdala, D. Reinalda, S. Alhassan, Developing Hydrophobic Graphene Foam for Oil Spill Cleanup, Ind. Eng.

Chem. Res. 56 (2017) 6945–6951. https://doi.org/10.1021/acs.iecr.7b00716.

[132] H. Li, Y. Huang, Y. Mao, W.L. Xu, H.J. Ploehn, M. Yu, Tuning the underwater oleophobicity of graphene oxide coatings via UV irradiation, Chem. Commun. 50 (2014) 9849–9851. https://doi.org/10.1039/C4CC03940H.

[133] Y.C. Cheng, T.P. Kaloni, Z.Y. Zhu, U. Schwingenschlögl, Oxidation of graphene in ozone under ultraviolet light, Appl. Phys. Lett. 101 (2012) 073110. https://doi.org/10.1063/1.4746261.

[134] P. Fabbri, L. Valentini, S. Bittolo Bon, D. Foix, L. Pasquali, M. Montecchi, M. Sangermano, In-situ graphene oxide reduction during UV-photopolymerization of graphene oxide/acrylic resins mixtures, Polymer (Guildf). 53 (2012) 6039–6044. https://doi.org/10.1016/j.polymer.2012.10.045.

[135] V.H. Pham, T.V. Cuong, S.H. Hur, E. Oh, E.J. Kim, E.W. Shin, J.S. Chung, Chemical functionalization of graphene sheets by solvothermal reduction of a graphene oxide suspension in N-methyl-2-pyrrolidone, J. Mater. Chem. 21 (2011) 3371–3377. https://doi.org/10.1039/C0JM02790A.

[136] T. Nakajima, A. Mabuchi, R. Hagiwara, A new structure model of graphite oxide, Carbon N. Y. 26 (1988) 357–361. https://doi.org/10.1016/0008-6223(88)90227-8.

[137] E. Yang, M.-H. Ham, H.B. Park, C.-M. Kim, J. Song, I.S. Kim, Tunable semi-permeability of graphene-based membranes by adjusting reduction degree of laminar graphene oxide layer, J. Memb. Sci. 547 (2018) 73–79. https://doi.org/10.1016/j.memsci.2017.10.039.

[138] S.-J. Mu, Y.-C. Su, L.-H. Xiao, S.-D. Liu, T. Hu, H.-B. Tang, X-Ray Difraction Pattern of Graphite Oxide, Chinese Phys. Lett. 30 (2013) 096101. https://doi.org/10.1088/0256-307X/30/9/096101.

[139] T.F. Emiru, D.W. Ayele, Controlled synthesis, characterization and reduction of

graphene oxide: A convenient method for large scale production, Egypt. J. Basic Appl. Sci. 4 (2017) 74–79. https://doi.org/10.1016/j.ejbas.2016.11.002.

[140] J.S. Cho, W. Jang, S.C. Mun, M. Yi, J.H. Park, D.H. Wang, Tuning surface chemistry and morphology of graphene oxide by γ-ray irradiation for improved performance of perovskite photovoltaics, Carbon N. Y. 139 (2018) 564–571. https://doi.org/10.1016/j.carbon.2018.07.010.

[141] S. Verma, R.K. Dutta, A facile method of synthesizing ammonia modified graphene oxide for efficient removal of uranyl ions from aqueous medium, RSC Adv. 5 (2015) 77192–77203. https://doi.org/10.1039/C5RA10555B.

[142] S. Chen, J. Hong, H. Yang, J. Yang, Adsorption of uranium (VI) from aqueous solution using a novel graphene oxide-activated carbon felt composite, J. Environ. Radioact. 126 (2013) 253–258. https://doi.org/10.1016/j.jenvrad.2013.09.002.

[143] S. Panigrahi, S. Praharaj, S. Basu, S.K. Ghosh, S. Jana, S. Pande, T. Vo-Dinh, H. Jiang, T. Pal, Self-Assembly of Silver Nanoparticles: Synthesis, Stabilization, Optical Properties, and Application in Surface-Enhanced Raman Scattering, J. Phys. Chem. B. 110 (2006) 13436–13444. https://doi.org/10.1021/jp062119l.

[144] P. Bhawal, S. Ganguly, T.K. Chaki, N.C. Das, Synthesis and characterization of graphene oxide filled ethylene methyl acrylate hybrid nanocomposites, RSC Adv. 6 (2016) 20781–20790. https://doi.org/10.1039/C5RA24914G.

[145] S. Chowdhury, R. Balasubramanian, Recent advances in the use of graphene-family nanoadsorbents for removal of toxic pollutants from wastewater, Adv. Colloid Interface Sci. 204 (2014) 35–56. https://doi.org/10.1016/j.cis.2013.12.005.

[146] X. Zhang, Z. Sui, B. Xu, S. Yue, Y. Luo, W. Zhan, B. Liu, Mechanically strong and highly conductive graphene aerogel and its use as electrodes for electrochemical power sources, J. Mater. Chem. 21 (2011) 6494. https://doi.org/10.1039/c1jm10239g.

[147] Z. Xu, Z. Li, C.M.B. Holt, X. Tan, H. Wang, B.S. Amirkhiz, T. Stephenson, D. Mitlin, Electrochemical Supercapacitor Electrodes from Sponge-like Graphene Nanoarchitectures with Ultrahigh Power Density, J. Phys. Chem. Lett. 3 (2012) 2928–2933. https://doi.org/10.1021/jz301207g.

[148] L.-Y. Meng, S.-J. Park, Effect of exfoliation temperature on carbon dioxide capture of graphene nanoplates, J. Colloid Interface Sci. 386 (2012) 285–290. https://doi.org/10.1016/j.jcis.2012.07.025.

[149] L. Ren, K.N. Hui, K.S. Hui, Y. Liu, X. Qi, J. Zhong, Y. Du, J. Yang, 3D hierarchical porous graphene aerogel with tunable meso-pores on graphene nanosheets for high-performance energy storage, Sci. Rep. 5 (2015) 14229. https://doi.org/10.1038/srep14229.

[150] Y. Xu, K. Sheng, C. Li, G. Shi, Self-assembled graphene hydrogel via a one-step hydrothermal process, ACS Nano. 4 (2010) 4324–4330. https://doi.org/10.1021/nn101187z.

[151] V. Presser, J. McDonough, S.-H. Yeon, Y. Gogotsi, Effect of pore size on carbon dioxide sorption by carbide derived carbon, Energy Environ. Sci. 4 (2011) 3059. https://doi.org/10.1039/c1ee01176f.

[152] Y. Wang, C. Guan, K. Wang, C.X. Guo, C.M. Li, Nitrogen, Hydrogen, Carbon Dioxide, and Water Vapor Sorption Properties of Three-Dimensional Graphene, J. Chem. Eng. Data. 56 (2011) 642–645. https://doi.org/10.1021/je100840n.

[153] C.-Y. Kuo, Comparison with as-grown and microwave modified carbon nanotubes to removal aqueous bisphenol A, Desalination. 249 (2009) 976–982. https://doi.org/10.1016/j.desal.2009.06.058.

[154] R.-L. Tseng, F.-C. Wu, R.-S. Juang, Adsorption of CO2 at atmospheric pressure on activated carbons prepared from melamine-modified phenol–formaldehyde resins, Sep.

Purif. Technol. 140 (2015) 53–60. https://doi.org/10.1016/j.seppur.2014.11.018.

[155] C. Zhao, Y. Guo, C. Li, S. Lu, Removal of low concentration CO2 at ambient temperature using several potassium-based sorbents, Appl. Energy. 124 (2014) 241–247. https://doi.org/10.1016/j.apenergy.2014.02.054.

[156] S. Hosseini, E. Marahel, I. Bayesti, A. Abbasi, L. Chuah Abdullah, T.S.Y. Choong, CO2 adsorption on modified carbon coated monolith: effect of surface modification by using alkaline solutions, Appl. Surf. Sci. 324 (2015) 569–575. https://doi.org/10.1016/j.apsusc.2014.10.054.

[157] A.I. Pruna, A. Barjola, A.C. Cárcel, B. Alonso, E. Giménez, Effect of Varying Amine Functionalities on CO2 Capture of Carboxylated Graphene Oxide-Based Cryogels, Nanomaterials. 10 (2020) 1446. https://doi.org/10.3390/nano10081446.

[158] K.S. Lakhi, W.S. Cha, S. Joseph, B.J. Wood, S.S. Aldeyab, G. Lawrence, J.-H. Choy, A. Vinu, Cage type mesoporous carbon nitride with large mesopores for CO2 capture, Catal. Today. 243 (2015) 209–217. https://doi.org/10.1016/j.cattod.2014.08.036.

[159] M.H. Chahbani, D. Tondeur, Pressure drop in fixed-bed adsorbers, Chem. Eng. J. 81 (2001) 23–34. https://doi.org/10.1016/S1385-8947(00)00215-1.

[160] A. Moran, O. Talu, Role of Pressure Drop on Rapid Pressure Swing Adsorption Performance, Ind. Eng. Chem. Res. 56 (2017) 5715–5723. https://doi.org/10.1021/acs.iecr.7b00577.

[161] B. Baghapour, M. Rouhani, A. Sharafian, S.B. Kalhori, M. Bahrami, A pressure drop study for packed bed adsorption thermal energy storage, Appl. Therm. Eng. 138 (2018) 731–739. https://doi.org/10.1016/j.applthermaleng.2018.03.098.

[162] N. Sundaram, P.C. Wankat, Pressure drop effects in the pressurization and blowdown steps of pressure swing adsorption, Chem. Eng. Sci. 43 (1988) 123–129. https://doi.org/10.1016/0009-2509(88)87133-1.

[163] C. Ma, J. Bai, M. Demir, X. Hu, S. Liu, L. Wang, Water chestnut shell-derived N/S-doped porous carbons and their applications in CO2 adsorption and supercapacitor, Fuel. 326 (2022) 125119. https://doi.org/10.1016/j.fuel.2022.125119.

[164] J. Bai, J. Huang, Q. Yu, M. Demir, F.H. Gecit, B.N. Altay, L. Wang, X. Hu, One-pot synthesis of self S-doped porous carbon for efficient CO2 adsorption, Fuel Process. Technol. 244 (2023) 107700. https://doi.org/10.1016/j.fuproc.2023.107700.

[165] A.K. Sahu, V.C. Srivastava, I.D. Mall, D.H. Lataye, Adsorption of Furfural from Aqueous Solution onto Activated Carbon: Kinetic, Equilibrium and Thermodynamic Study, Sep. Sci. Technol. 43 (2008) 1239–1259. https://doi.org/10.1080/01496390701885711.

[166] K. Bera, A. Karmakar, K. Karthick, S.S. Sankar, S. Kumaravel, R. Madhu, S. Kundu, Enhancement of the OER Kinetics of the Less-Explored α-MnO 2 via Nickel Doping Approaches in Alkaline Medium, Inorg. Chem. 60 (2021) 19429–19439. https://doi.org/10.1021/acs.inorgchem.1c03236.

[167] P.M. Sudeep, T.N. Narayanan, A. Ganesan, M.M. Shaijumon, H. Yang, S. Ozden, P.K. Patra, M. Pasquali, R. Vajtai, S. Ganguli, A.K. Roy, M.R. Anantharaman, P.M. Ajayan, Covalently interconnected three-dimensional graphene oxide solids, ACS Nano. 7 (2013) 7034–7040. https://doi.org/10.1021/nn402272u.

[168] L. Aljerf, High-efficiency extraction of bromocresol purple dye and heavy metals as chromium from industrial effluent by adsorption onto a modified surface of zeolite: Kinetics and equilibrium study, J. Environ. Manage. 225 (2018) 120–132. https://doi.org/10.1016/j.jenvman.2018.07.048.

[169] A. Khelifa, L. Benchehida, Z. Derriche, Adsorption of carbon dioxide by X zeolites exchanged with Ni2+ and Cr3+: isotherms and isosteric heat, J. Colloid Interface Sci. 278 (2004) 9–17. https://doi.org/10.1016/j.jcis.2004.05.033.

[170] V. Chabot, D. Higgins, A. Yu, X. Xiao, Z. Chen, J. Zhang, A review of graphene and graphene oxide sponge: material synthesis and applications to energy and the environment, Energy Environ. Sci. 7 (2014) 1564. https://doi.org/10.1039/c3ee43385d.

[171] C. Goel, H. Kaur, H. Bhunia, P.K. Bajpai, Carbon dioxide adsorption on nitrogen enriched carbon adsorbents: Experimental, kinetics, isothermal and thermodynamic studies, J. CO2 Util. 16 (2016) 50–63. https://doi.org/10.1016/j.jcou.2016.06.002.

[172] Y. Chen, D. Lv, J. Wu, J. Xiao, H. Xi, Q. Xia, Z. Li, A new MOF-505@GO composite with high selectivity for CO 2 /CH 4 and CO 2 /N 2 separation, Chem. Eng. J. 308 (2017) 1065–1072. https://doi.org/10.1016/j.cej.2016.09.138.

[173] O. Hamdaoui, E. Naffrechoux, Modeling of adsorption isotherms of phenol and chlorophenols onto granular activated carbon. Part I. Two-parameter models and equations allowing determination of thermodynamic parameters, J. Hazard. Mater. 147 (2007) 381–394. https://doi.org/10.1016/j.jhazmat.2007.01.021.

[174] Y. Liu, J. Wilcox, Effects of surface heterogeneity on the adsorption of CO 2 in microporous carbons, Environ. Sci. Technol. 46 (2012) 1940–1947. https://doi.org/10.1021/es204071g.

[175] S.-C. Hsu, C. Lu, F. Su, W. Zeng, W. Chen, Thermodynamics and regeneration studies of CO2 adsorption on multiwalled carbon nanotubes, Chem. Eng. Sci. 65 (2010) 1354–1361. https://doi.org/10.1016/j.ces.2009.10.005.

[176] Q. Yu, J. Bai, J. Huang, M. Demir, A.A. Farghaly, P. Aghamohammadi, X. Hu, L. Wang, One-Pot Synthesis of Melamine Formaldehyde Resin-Derived N-Doped Porous Carbon for CO2 Capture Application, Molecules. 28 (2023) 1772. https://doi.org/10.3390/molecules28041772.

[177] R.K. Jha, H. Bhunia, S. Basu, Enhancing CO2 capture through innovating monolithic graphene oxide frameworks, Environ. Res. 249 (2024) 118426.

https://doi.org/10.1016/j.envres.2024.118426.

[178] Y. Yuan, T.R. Lee, Contact angle and wetting properties, in: Springer Ser. Surf. Sci., 2013: pp. 3–34. https://doi.org/10.1007/978-3-642-34243-1_1.

[179] W. Ouyang, D. Zeng, X. Yu, F. Xie, W. Zhang, J. Chen, J. Yan, F. Xie, L. Wang, H. Meng, D. Yuan, Exploring the active sites of nitrogen-doped graphene as catalysts for the oxygen reduction reaction, Int. J. Hydrogen Energy. 39 (2014) 15996–16005. https://doi.org/10.1016/j.ijhydene.2014.01.045.

[180] S. Pei, H.M. Cheng, The reduction of graphene oxide, Carbon N. Y. 50 (2012) 3210–3228. https://doi.org/10.1016/j.carbon.2011.11.010.

[181] L. Stobinski, B. Lesiak, A. Malolepszy, M. Mazurkiewicz, B. Mierzwa, J. Zemek, P. Jiricek, I. Bieloshapka, Graphene oxide and reduced graphene oxide studied by the XRD, TEM and electron spectroscopy methods, J. Electron Spectros. Relat. Phenomena. 195 (2014) 145–154. https://doi.org/10.1016/j.elspec.2014.07.003.

[182] E.S. Ganya, N. Soin, S.J. Moloi, J.A. McLaughlin, W.F. Pong, S.C. Ray, Polyacrylate grafted graphene oxide nanocomposites for biomedical applications, J. Appl. Phys. 127 (2020) 054302. https://doi.org/10.1063/1.5135572.

[183] B. Gupta, N. Kumar, K. Panda, V. Kanan, S. Joshi, I. Visoly-Fisher, Role of oxygen functional groups in reduced graphene oxide for lubrication, Sci. Rep. 7 (2017) 45030. https://doi.org/10.1038/srep45030.

[184] D. Tiwari, C. Goel, H. Bhunia, P.K. Bajpai, Melamine-formaldehyde derived porous carbons for adsorption of CO2 capture, J. Environ. Manage. 197 (2017) 415–427. https://doi.org/10.1016/j.jenvman.2017.04.013.

[185] J. Shi, N. Yan, H. Cui, Y. Liu, Y. Weng, D. Li, X. Ji, Nitrogen doped hierarchically porous carbon derived from glucosamine hydrochloride for CO2 adsorption, J. CO2 Util. 21 (2017) 444–449. https://doi.org/10.1016/j.jcou.2017.08.010.

[186] L. Zhou, J. Fan, G. Cui, X. Shang, Q. Tang, J. Wang, M. Fan, Highly efficient and reversible CO 2 adsorption by amine-grafted platelet SBA-15 with expanded pore diameters and short mesochannels, Green Chem. 16 (2014) 4009–4016. https://doi.org/10.1039/C4GC00832D.

[187] K. Xia, X. Tian, S. Fei, K. You, Hierarchical porous graphene-based carbons prepared by carbon dioxide activation and their gas adsorption properties, Int. J. Hydrogen Energy. 39 (2014) 11047–11054. https://doi.org/10.1016/j.ijhydene.2014.05.059.

[188] T.C. Drage, A. Arenillas, K.M. Smith, C. Pevida, S. Piippo, C.E. Snape, Preparation of carbon dioxide adsorbents from the chemical activation of urea–formaldehyde and melamine–formaldehyde resins, Fuel. 86 (2007) 22–31. https://doi.org/10.1016/j.fuel.2006.07.003.

[189] A. Busch, Y. Gensterblum, B.M. Krooss, Methane and CO2 sorption and desorption measurements on dry Argonne premium coals: pure components and mixtures, Int. J. Coal Geol. 55 (2003) 205–224. https://doi.org/10.1016/S0166-5162(03)00113-7.

[190] A.B. Wassie, V.C. Srivastava, Teff straw characterization and utiization for chromium removal from lwastewater: Kinetics, isotherm and thermodynamic modelling, J. Environ. Chem. Eng. 4 (2016) 1117–1125. https://doi.org/10.1016/j.jece.2016.01.019.

[191] V. Krungleviciute, A.D. Migone, M. Yudasaka, S. Iijima, CO 2 adsorption on dahlia-like carbon nanohorns: Isosteric heat and surface area measurements, J. Phys. Chem. C. 116 (2012) 306–310. https://doi.org/10.1021/jp208766u.

[192] S. Chowdhury, R. Balasubramanian, Highly efficient, rapid and selective CO2 capture by thermally treated graphene nanosheets, J. CO2 Util. 13 (2016) 50–60. https://doi.org/10.1016/j.jcou.2015.12.001.

[193] R.K. Jha, H. Bhunia, S. Basu, UV activated monolithic graphene Oxide-Based adsorbents for dynamic CO2 Capture: Kinetic, isotherm and thermodynamic studies,

Chem. Eng. Sci. (2023) 119572.

[194] S. Guo, J. Raya, D. Ji, Y. Nishina, C. Ménard-Moyon, A. Bianco, Is carboxylation an efficient method for graphene oxide functionalization?, Nanoscale Adv. 2 (2020) 4085–4092. https://doi.org/10.1039/D0NA00561D.

[195] X. Hu, L. Mu, J. Wen, Q. Zhou, Covalently synthesized graphene oxide-aptamer nanosheets for efficient visible-light photocatalysis of nucleic acids and proteins of viruses, Carbon N. Y. 50 (2012) 2772–2781. https://doi.org/10.1016/j.carbon.2012.02.038.

[196] K. Lv, P. Huang, Z. Zhou, X. Wei, Q. Luo, Z. Huang, H. Yan, H. Jia, Study of Janus Amphiphilic Graphene Oxide as a High-Performance Shale Inhibitor and Its Inhibition Mechanism, Front. Chem. 8 (2020). https://doi.org/10.3389/fchem.2020.00201.

[197] M. Jiang, Y. Xiong, B. Xue, Q. Zhang, Q. Wan, H. Zhao, Multi-layer graphene oxide synergistically modified by two coupling agents and its application in reinforced natural rubber composites, RSC Adv. 8 (2018) 29847–29854. https://doi.org/10.1039/c8ra05016c.

[198] S. Joshi, S. Kalyanasundaram, V. Balasubramanian, Quantitative Analysis of Sodium Carbonate and Sodium Bicarbonate in Solid Mixtures Using Fourier Transform Infrared Spectroscopy (FT-IR), Appl. Spectrosc. 67 (2013) 841–845. https://doi.org/10.1366/12-06915.

[199] L. Liu, H. Chen, E. Shiko, X. Fan, Y. Zhou, G. Zhang, X. Luo, X. (Eric) Hu, Low-cost DETA impregnation of acid-activated sepiolite for CO2 capture, Chem. Eng. J. 353 (2018) 940–948. https://doi.org/10.1016/j.cej.2018.07.086.

LIST OF PUBLICATIONS

Related to Ph.D. work

[1]. Ranjeet Kumar Jha, Haripada Bhunia, Soumen Basu, UV activated monolithic graphene Oxide-Based adsorbents for dynamic CO2 Capture: Kinetic, isotherm and thermodynamic studies, Chem. Eng. Sci. 285 (2024) 119572. https://doi.org/10.1016/j.ces.2023.119572. (IF: 4.7)

[2]. Ranjeet Kumar Jha, Haripada Bhunia, Soumen Basu, Enhancing CO2 capture through innovating monolithic graphene oxide frameworks, Environ. Res. 249 (2024) 118426. https://doi.org/10.1016/j.envres.2024.118426. (IF: 8.3)

[3]. Ranjeet Kumar Jha, Haripada Bhunia, Soumen Basu, Experimental kinetics and thermodynamics investigation: Chemically activated carbon-enriched monolithic reduced graphene oxide for efficient CO2 capture, Heliyon. 10 (2024) e27439. https://doi.org/10.1016/j.heliyon.2024.e27439. (IF: 4.0)

[4]. Ranjeet Kumar Jha, Haripada Bhunia, Soumen Basu, Synergistic Enhancement of CO2 Capture Performance through Self-Assembled Reduction of Monolithic Graphene Oxide-Based Nano Adsobents, (Under review)

LIST OF CONFERENCES AND WORKSHOP

Related to Ph. D. work

[1] Poster presentation on the topic “Enhancing the CO_2 Capture Efficiency by Physically Activated Monolithic Graphene Oxide-based Adsorbents: Effect of Various UV-treatment Time” 13th in SERIES AND 1st INTERNATIONAL CONFERENCE on Recent Advances in chemistry (CRAC – 2023) organized by Department of Chemistry, Punjabi University, Patiala (23rd -24th February, 2023).

[2] Best poster presentation award on the topic “Chemically Activated Carbon Enriched Monolithic Reduced Graphene Oxide-Based Adsorbents for CO_2 Capture: Experimental Kinetic and Thermodynamic Studies” 2nd International Conference on “Intellection, Innovation and Implication in Chemistry” (IIIC-2023) organized by Department of Chemistry, DAV University, Jalandhar (18th -19th April, 2023).

[3] Attend workshop on “Advanced Instrumentation Techniques in Chemical Analysis” organized by School of Chemistry and Biochemistry, T.I.E.T., Patiala (04th – 05th October, 2023).

EDITIONS OF PUBLISHED ARTICLES

Chemical Engineering Science 285 (2024) 119572

Contents lists available at ScienceDirect

Chemical Engineering Science

journal homepage: www.elsevier.com/locate/ces

UV activated monolithic graphene Oxide-Based adsorbents for dynamic CO_2 Capture: Kinetic, isotherm and thermodynamic studies

Ranjeet Kumar Jha[a], Haripada Bhunia[b,*], Soumen Basu[a,*]

[a] School of Chemistry and Biochemistry, Thapar Institute of Engineering and Technology, Patiala-147004, Punjab, India
[b] Department of Chemical Engineering, Thapar Institute of Engineering and Technology, Patiala-147004, Punjab, India

ARTICLE INFO

Keywords:
Monolithic graphene oxide
UV-treatment
CO_2 capture
Kinetic study
Isotherm study
Thermodynamic study

ABSTRACT

In this research article, the synthesis of monolithic graphene oxide-based adsorbent was prepared by the self-assembly process of graphene oxide followed by oxalic acid reduction with various mass ratios and activated by UV treatments. The optimized adsorbent reveals an excellent dynamic CO_2 capture capacity of 1.65 mmol g^{-1} at 25 °C, owing to its elevated BET surface area of 577.3 m^2/g. Considering the desorption step with a constant volume flow rate, it becomes evident that the pressure drop results in excessive consumption of desorbing gas (N_2) approximately 50 % for the regeneration process. Several studied were investigated; the regenerability of 98.8 %, an excellent CO_2/N_2 selectivity, fast kinetics, the pseudo-second-order kinetic model and Freundlich isotherm model were best fitted. Thermodynamic studies reveal the heterogeneity of adsorption site, the adsorption process endothermic nature, as indicated by $\Delta H°$ value of + 13.1154139 KJ mol^{-1}, underscoring the distinctive characteristic property of chemisorption.

1. Introduction

Carbonaceous products cause global warming due to the emission of combustion and burning of fossil fuels, as well as increased motor vehicle practice. The chemical industry plays a vital role in the CO_2 levels increase in the atmosphere and the environment due to anthropogenic happenings (Darunte et al., 2016; Jacobson, 2009; Raupach et al., 2007; Varghese et al., 2020). Thus, released anthropogenic CO_2 is utilized by various factors (Zulfiqar et al., 2013). So, CO_2 capture technology plays an essential role in decreasing the concentration of CO_2 in the atmosphere. Amine adsorption is more grown and widely utilizes CCS technology. However, the regeneration study of adsorbents is costly, which is the main drawback of this adsorbent (Leung et al., 2014). CCS technology has been used for CO_2 capture of solid adsorbents as practicable alternatives. Recently, many solid adsorbents have been observed for CO_2 adsorption (Maina et al., 2017), likely graphene (Chowdhury and Balasubramanian, 2016; Fang et al., 2018; Politakos et al., 2020; Varghese et al., 2020), activated carbon (Franchi et al., 2005), Zeolite (Bae et al. 2013), silica (de la Casa-Lillo et al., 2002), and many more. Graphene, an extraordinary carbonaceous material, holds immense promise across a range of domains, including electronics, catalysis, energy applications, and adsorption (Dreyer et al., 2010; Novoselov et al., 2004). To harness its potential in these arenas, the assembly of individual graphene sheets into a macroscopic graphene monolith is crucial (Tang et al., 2010; Yang et al., 2011). Based on the literature review, we have developed monolithic materials and activated by UV treatment. The resultant materials have various characteristics properties found as the light weight, low density, ability to deform and absorb energy, open porosity, good morphology, high surface area, excellent CO_2 adsorption capacity, and many more.

The major advantage of CO_2 capture is that it produces the appearance of the solid sorbents of the monoliths in a simple way. Because of its distinctive porous structure, graphitic nature, stability, cost-effectiveness, and versatility in functionalization with a wide range of partners, such as graphene oxide (GO), a type of porous carbonaceous material is observed as particularly attractive for CO_2 capture (Pokhrel et al., 2018), to optimize adsorption performance and improve efficiency (Huang and Feng, 2018; Srinivas et al., 2012). Monolithic graphene oxide is generated from graphene oxide through controlled oxidation and elimination processes, with the resulting material's ultimate properties being determined by the chosen methodology and extent of oxidation (Dimiev and Tour, 2014; Marcano et al., 2010). The basis of it is a hexagonally arranged, two-dimensional graphitic structure with sp^2 and sp^3 hybridization in the carbon atoms

---

* Corresponding authors.
E-mail addresses: hbhunia@thapar.edu (H. Bhunia), soumen.basu@thapar.edu (S. Basu).

https://doi.org/10.1016/j.ces.2023.119572
Received 11 September 2023; Received in revised form 8 November 2023; Accepted 27 November 2023

Heliyon 10 (2024) e27439

Contents lists available at ScienceDirect

Heliyon

journal homepage: www.cell.com/heliyon

Research article

Experimental kinetics and thermodynamics investigation: Chemically activated carbon-enriched monolithic reduced graphene oxide for efficient CO_2 capture

Ranjeet Kumar Jha [a], Haripada Bhunia [b,**], Soumen Basu [a,*]

[a] Department of Chemistry and Biochemistry, Thapar Institute of Engineering and Technology, Patiala 147004, Punjab, India
[b] Department of Chemical Engineering, Thapar Institute of Engineering and Technology, Patiala 147004, Punjab, India

ARTICLE INFO

Keywords:
Monolith
Graphene oxide
Chemically activated
CO_2 capture
Kinetic study
Thermodynamic study

ABSTRACT

In this research, we have developed solid MGOs by self-assembled reduction process of GO at 90 °C with different weight ratios of oxalic acid (1:1, 1:0.500, and 1:0.250). The as-synthesized monoliths were carbonized (at 600 °C) and chemically activated with varying proportions of NaOH (1:1, 1:2, and 1:3). This materials offer the CO_2 adsorption effect under dynamic conditions, fast mass transfer, easy handling, and outstanding stability throughout the adsorption-desorption cycle. FE-SEM, and HR-TEM analyses confirmed the porous nature and shape of the adsorbents, while XPS examination revealed the presence of distinct functional groups on the surface of the monolith. By increasing the mass ratios (MGO:NaOH) from 1:1 to 1:2, the surface areas increased by approximately 2.6 times, ranging from 520.8 to 753.9 $m^2 g^{-1}$ (surface area of the untreated MGO was 289.2 $m^2 g^{-1}$). Consequently, this resulted in a notable enhancement of 2.10 mmol g^{-1} in dynamic CO_2 capture capacity. The assessment encompassed the evaluation of production yield, selectivity, regenerability, kinetics, equilibrium isotherm, and isosteric temperatures of adsorption (Q_{st}). The decrease in CO_2 capture effectiveness with rising adsorption temperature indicated an exothermic and physisorption process. The regenerability of 99.1 % at 100 °C and excellent cyclic stability with efficient CO_2 adsorption make this monolithic adsorbent appropriate for post-combustion CO_2 capture. The significant Q_{st} lend support to the heterogeneity of the adsorbent's surface, and the pseudo-second-order kinetic model along with the Freundlich isotherm model emerged as the most fitting. Therefore, the current investigation shows that the carbon-enriched adsorbents enhance the CO_2 adsorption capacity. It may be used as a low-cost pretreatment method on an industrial scale before carbon capture.

1. Introduction

The effects of CO_2 emissions cause global warming [1]. The combustion of fossil fuels and emissions, coupled with the extensive use of motor vehicles, has contributed to the escalation of climate change [2–4]. Hence, anthropogenic CO_2 emissions find application in various processes [5]. Thus, mitigating atmospheric CO_2 levels necessitates the deployment of CO_2 capture technologies. Amine adsorption stands out as a well-established method, making widespread use of CCS technology. Regrettably, the primary drawback of

---

* Corresponding author.
** Corresponding author.
E-mail addresses: hbhunia@thapar.edu (H. Bhunia), soumen.basu@thapar.edu (S. Basu).

https://doi.org/10.1016/j.heliyon.2024.e27439
Received 3 April 2023; Received in revised form 19 February 2024; Accepted 28 February 2024

Environmental Research 249 (2024) 118426

Contents lists available at ScienceDirect

Environmental Research

journal homepage: www.elsevier.com/locate/envres

Enhancing CO_2 capture through innovating monolithic graphene oxide frameworks

Ranjeet Kumar Jha [a], Haripada Bhunia [b,**], Soumen Basu [a,*]

[a] School of Chemistry and Biochemistry, Thapar Institute of Engineering and Technology, Patiala, 147004, Punjab, India
[b] Department of Chemical Engineering, Thapar Institute of Engineering and Technology, Patiala, 147004, Punjab, India

ARTICLE INFO

Keywords:
Monolith
Graphene oxide
KOH-Treatment
Selectivity
CO_2 capture

ABSTRACT

The advancement and engineering of novel crystalline materials is facilitated through the utilization of innovative porous crystalline structures, established via KOH-treated monolithic graphene oxide frameworks. These materials exhibit remarkable and versatile characteristics for both functional exploration and applications within the realm of CO_2 capture. In this comprehensive study, we have synthesized monolithic reduced graphene oxide-based adsorbents through a meticulous self-assembly process involving different mass ratios of GO/malic acid (MaA) (1:0.250, 1:0.500, and 1:1 by weight). Building upon this foundation, we further modified MGO 0.250 through KOH-treatment by chloroacetic acid method, leading to the creation of MGO 0.250_KOH, which was subjected to CO_2 capture assessments. The comprehensive investigation encompassed an array of parameters including morphology, specific surface area, crystal defects, functional group identification, and CO_2 capture efficiency. Employing a combination of FT-IR, XRD, Raman, BET, SEM, HR-TEM, and XPS techniques, the study revealed profound insights. Particularly notable was the observation that the MGO 0.250_KOH adsorbent exhibited an exceptional CO_2 capture performance, leading to a significant enhancement of the CO_2 capture capacity from 1.69 mmol g^{-1} to 2.35 mmol g^{-1} at standard conditions of 25 °C and 1 bar pressure. This performance enhancement was concomitant with an augmentation in surface area, elevating from 287.93 to 419.75 $m^2 g^{-1}$ (a nearly 1.5-fold increase compared to MGO 1.000 with a surface area of 287.93 $m^2 g^{-1}$). The monolithic adsorbent demonstrated a commendable production yield of 82.92%, along with an impressive regenerability of 98.80% at 100 °C. Additionally, adsorbent's proficiency in CO_2 adsorption, rendering it a promising candidate for post-combustion CO_2 capture applications. These findings collectively underscore the capacity adsorbents to significantly amplify CO_2 capture capabilities. The viability of employing this strategy as an uncomplicated pretreatment technique in various industrial sectors is a plausible prospect, given the study's outcomes.

1. Introduction

Graphene, an extraordinary carbonaceous material, holds immense promise across a range of domains, including electronics, catalysis, energy applications, and adsorption. Monolithic nanomaterials stand out for their substantial CO_2 capture capacities, distinguishing them from metal-organic frameworks or zeolites (An et al., 2013; Kenarsari et al., 2013; Ma et al., 2014; Nandi et al., 2012; S et al., 2012). Sustainable technologies typically serve as the foundation for a wide range of goods and services that enhance quality of life, save expenses, and minimize or completely eliminate their negative effects on the environment. The chemical process industry's sustainable development depends on the utilization of graphene-based monoliths. They facilitate the environmentally friendly synthesis of products by consuming less energy and, in some situations, preventing the creation of waste and byproducts. The so-called integrated approach to environmental protection, which includes, among other things, the integration of multiple process the processes including chemical reaction, separation, heat exchange, and momentum transfer, benefits greatly from the use of monoliths, especially when implemented in an organized manner (Dreyer et al., 2010; Novoselov et al., 2004; Tomašić and Jović, 2006). Among the various porous carbonaceous materials, graphene oxide (GO) stands out, recognized for its potential in CO_2 capture (Pokhrel et al., 2018). This unique property makes it a compelling candidate for optimizing

---

* Corresponding author.
** Corresponding author.
E-mail addresses: hbhunia@thapar.edu (H. Bhunia), soumen.basu@thapar.edu (S. Basu).

https://doi.org/10.1016/j.envres.2024.118426
Received 5 October 2023; Received in revised form 31 January 2024; Accepted 4 February 2024